ANALYSIS AND ENGINEERING OF LIGHT IN COMPLEX MEDIA VIA GEOMETRICAL OPTICS

ALIREZA AKBARZADEH

A THESIS SUBMITTED
FOR THE DEGREE OF DOCTOR OF PHILOSOPHY

DEPARTMENT OF ELECTRICAL AND COMPUTER ENGINEERING

NATIONAL UNIVERSITY OF SINGAPORE

2014

DECLARATION

I hereby declare that this thesis is my original work and it has been written by me in its entirety. I have duly acknowledged all the sources of information which have been used in the thesis.

This thesis has also not been submitted for any degree in any university previously.

Alireza Akbarzadeh
28 May 2014

Science is wonderfully equipped to answer the question "How?",
but it gets terribly confused when you ask the question "Why"?

Erwin Chargaff

ACKNOWLEDGEMENTS

This thesis is truly dedicated to those who have kindly supported me during the past years, without whose helps I would have never been at this position that currently I am. Unfortunately this page is too small for me to express my sincerest gratitude to all those people to whom I owe all my achievements.

Without any doubt the main role in my education and success (if any) belongs to my parents who took my hands from the day of my birth, took steps as small as a toddler's, were patient enough to respond my curiosity and ignorance, provided me a lovely place to grow and to bloom, and were present at all the hard times that I needed someone to lean on. I also need to appreciate my brother and my sister who have helped me in a great deal so far and have made my life so pleasant. I always see them beside myself and feel their encouragements. These are the reasons that I am always thankful to God for giving me such a blessed family.

I take this opportunity to thank all my teachers, from the primary school to university, for every good lesson that they taught me and made me a better person. It is a pity that here I cannot name all of them and admire them one by one. But among them, I need to offer my special thanks to Aaron Danner and Cheng-Wei Qiu who were my advisors, teachers and friends during my PhD studies in the last four years in NUS. I was lucky to have them with me in NUS. Unquestionably without their advices and supports I would not be able to reach this point. I warmly shake their hands and thank them for everything they gave me during these four years.

I owe a big thanks to my close friends for their companionship, for the time that they spent with me and for all the good feelings they generously gave me. In addition, I appreciate all the people in the Centre for Optoelectronics (COE) in NUS with whom I had good times and spent most of my working life during the last four years.

And finally I am grateful to NUS and Agency for Science, Technology and Research (A*STAR) for offering me the scholarship to pursue my PhD studies in Singapore.

Dedicated to my mother, Fatmeh Moshfea
&
my father, Rahman Akbarzadeh.

Table of Contents

Summary

In this thesis we study different features of Graded-Index Media from the Geometrical Optics point of view and we explore effective techniques of analysis and design of interesting optical Meta-Devices.

First, with the help of tensor analysis we generalize ray tracing machinery in a coordinate-free style and we show in detail how ray tracing in anisotropic media in arbitrary coordinate systems and curved spaces can be carried out. Writing Maxwell's equations in the most general form, we derive a coordinate-free form for the eikonal equation and hence the Hamiltonian of a general purpose medium. The expression works for both orthogonal and non-orthogonal coordinate systems, and we show how it can be simplified for biaxial and uniaxial media in orthogonal coordinate systems. In order to show the utility of the equation in a real case, we study both the isotropic and the uniaxially transmuted birefringent Eaton lens and derive the ray trajectories in spherical coordinates for each case.

Next, a reverse design schematic for designing a metamaterial magnifier with graded negative refractive index for both two-dimensional and three-dimensional cases is proposed. Photorealistic rendering is integrated with traced ray trajectories in example designs to visualize the scattering magnification as well as imaging of the proposed graded-index magnifier with negative index metamaterials. The material of the magnifying shell can be uniquely and independently determined without knowing beforehand the corresponding domain deformation. This reverse recipe and photorealistic rendering directly tackles the significance of all possible parametric profiles and demonstrates the performance of the device in a realistic scene, which provides a scheme to design, select and evaluate a metamaterial magnifier.

Third, based on the optical behavior of gradient biaxial dielectrics a design method is described in detail which allows one to combine the behavior of up to four totally independent isotropic optical instruments in an overlapping region of space. This is non-trivial because of the mixing of the index tensor elements in the Hamiltonian; previously known methods only handled uniaxial dielectrics (where only two independent isotropic optical functions could overlap). The biaxial method introduced also allows three-

dimensional multi-faced Janus devices to be designed; these are worked out in an example of what is possible to design with the method.

Finally, the mechanical interaction between light and graded-index media (both isotropic and anisotropic) is presented from the geometrical optics perspective. Utilizing Hamiltonian equations to determine ray trajectories combined with a description of the Lorentz force exerted on bound currents and charges, we provide a general method that we denote “force tracing” for determining the direction and magnitude of the bulk and surface force density in arbitrarily anisotropic and inhomogeneous media. This technique provides the optical community with machinery which can give a good estimation of the force field distribution in different complex media, and with significantly faster computation speeds than full wave methods allow. Comparison of force tracing against analytical solutions shows some unusual limitations of geometrical optics which we also illustrate.

List of Tables

List of Figures

List of Symbols

k	wave vector
ω	angular frequency
λ	wavelength
c	velocity of light
ε	permittivity
μ	permeability
n	refractive index
χ_e	electric susceptibility
χ_m	magnetic susceptibility

List of Publications

Journal Papers

A. Akbarzadeh, M. Danesh, C. –W. Qiu, and A. J. Danner, 2014, "Tracing optical force fields within graded-index media", New J. Phys. **16**, 053035 (2014).

A. Akbarzadeh, C. –W. Qiu, and A. J. Danner, 2013, "Exploiting design freedom in biaxial dielectrics to enable spatially overlapping optical instruments", Sci. Rep. **3**, 2055 (5 pages).

C. –W. Qiu, **A. Akbarzadeh**, T. C. Han, and A. J. Danner, 2012, "Photorealistic rendering of a graded negative-index metamaterial magnifier", New J. Phys. **14**, 033024 (10 pages).

A. Akbarzadeh and A. J. Danner, 2010, "Generalization of ray tracing in a linear inhomogeneous anisotropic medium: a coordinate-free approach", J. Opt. Soc. Am. A **27**, 2558-2562.

Conference Papers

A. Akbarzadeh, C. –W. Qiu, and A. J. Danner, 2014, "Force tracing versus ray tracing", To be presented in International Conference on Metamaterials, Photonic Crystals and Plasmonics (META), Singapore.

A. Akbarzadeh, C. –W. Qiu, T. Tyc, and A. J. Danner, 2013, "Visualization of Pulse Propagation and Optical Force in Graded-index Optical Devices", Oral presentation in Progress In Electromagnetic Research Symposium (PIERS), Stockholm, Sweden. [*Invited*]

E. Wong, L. Benaissa, **A. Akbarzadeh**, C. –W. Qiu, and A. J. Danner, 2012, "Maxwell's Fish-eye in Practice", Oral presentation in International Conference of Young Researchers on Advanced Materials (ICYRAM), Singapore.

A. J. Danner and **A. Akbarzadeh**, 2012, "Biaxial Anisotropy: A Survey of Interesting Optical Phenomena in Graded Media", Oral presentation in International Conference on Metamaterials, Photonic Crystals and Plasmonics (META), Paris, France.

A. Akbarzadeh, C. –W. Qiu, and A. J. Danner, 2012, "Biaxial Anisotropy in Gradient Permittivity Dielectric Optical Instruments", Oral presentation in Progress In Electromagnetic Research Symposium (PIERS), Kuala Lumpur, Malaysia.

A. Akbarzadeh, T. Han, A. J. Danner, and C. –W. Qiu, 2012, "Generalization of Superscatterer Design and Photorealistic Raytracing Thereof", Oral presentation in Progress In Electromagnetic Research Symposium (PIERS), Kuala Lumpur, Malaysia.

CHAPTER 1 Introduction

1.1 Motivation and Background

From the day that man first walked upon the earth, he started exploring his surrounding environment and learning how to manage his life. He was weak, alone and totally ignorant. But he had to face challenges, fight with natural disasters like volcanic eruptions, earthquakes, floods, and lightning. Wild beasts were his neighbors, and it was not easy to deal with these creatures. He did not have any knowledge about his body, the nature of viruses and diseases or their cures. He did not know how to sail, how to farm, how to hunt, how to love, or even how to talk. The wind looked like ghosts to him, the Sun and the Moon were two unknown gods, stars were believed to participate in his destiny, solar and lunar eclipses were considered to be the rage of gods and goddesses, and many other natural phenomena were sources of fear and divinity in his life. But he wanted to live with nature, and therefore he had to adapt himself to his surroundings. He was offered new experiences every day, and those exciting experiences could, at times, lead to the loss of his life. His only tools when facing those experiences were his five basic senses and his mind. He could see, hear, touch, smell and taste, and also think logically to answer his bewildering curiosities. However, among all his tools, his ability to see was the most important tool. His sophisticated vision was helping him perceive his world precisely, think, and then take an action. He was always scared by darkness, and night was frightful to him. Trivially, he had much appreciation for light and shining objects. Obviously he was also excited by light and he tried to know this strange and lovely friend around him. It can be one of the main reasons that humans have studied light, its interactions with objects, and its applications since ancient times.

Besides the countless undocumented studies of light that certainly took place over previous millennia, it was none other than Sir Isaac Newton who is largely thought of as the man who first studied light in a physical, scientific way. It was he whose study in 17th century was based on the assumption that light is *corpuscular*, which means that light can be thought of as a stream of tiny particles which spread out when light travels through space. This idea was considered in great detail, and inspired many other researchers to explore the physics of light from this point of view. However, in the early 19th century, in a very famous experiment by Thomas Young, it was shown that light can act like a wave, and produce diffraction patterns while travelling through narrow slits, though this fact was also previously seen in 17th century by Francesco Maria Grimaldi. Based on these observations and theoretical works by Christian Huygens and Augustin-Jean Fresnel, the theory of *wave optics* became more popular and later with the help of Maxwell's equations, it was believed that it was, in fact, the only correct theory of the nature of light.

Max Planck and Albert Einstein's respective explanations of *Black body radiation* and *Photoelectric effect* led to the most recent conclusion that light has both wave and particle characteristics.

The theory of optics can thus be considered an old, mature field of study, having been recognized by brilliant minds for many years. But in addition to its most basic and ancient function of allowing our eyes to function properly, light has, within just the last century, found use in myriad applications, especially in scientific applications. Different types of microscopy and imaging techniques, lasers, optical transceivers, optical fibers, optical lithography, optical cooling processes, optical lenses and their tomography techniques, all and all, are signs of the enormous number of applications of optics in our scientific life.

Due to the never-ending hunger of consumers to novel technologies, gadgets and luxuries in daily life, researchers are resorting to the interaction of light with novel and unusual materials and structures to bring about even more unusual and fascinating dimensions to human life. Illusions, cloaking and perfect imaging are examples of such attempts. To understand the excitement behind the astonishing physics of *metamaterials* and generally *complex media*, it is important to first review the global behavior of such media and comprehend their interaction with light.

1.2 Complex Media

Thanks to their rich physics and potential in future applications in optics, complex media have more recently become important research topics. The interaction of light and, in general, electromagnetic waves, with complex structures has led experimentalists to explore these materials in great depth after first observing many interesting phenomena. The negative refraction of light rays [1, 2], isotropic reflections [3], invisibility of cloaked objects and folding of visual space [4, 5], limitless imaging [6, 7], reversal of Cherenkov radiation [8], reversal of the Doppler effect [9], anti-parallelism of group velocity and phase velocity [10], strange shapes of the *k*-surface in a monochromatic propagation [11], and Fano resonances [12], etc., are examples of such interesting and unusual behaviors, which have already been observed or are expected to be observed in complex media. While such anomalous behavior in complex structures is permissible because of symmetry and space-time invariance of Maxwell's equations and is otherwise "natural" behavior, it is often surprising and unexpected, inspiring theoretical researchers to reconsider many fundamental properties of light, both in classical and quantum electrodynamics. As a consequence, a large number of papers on different aspects of complex media have been recently published. As can be seen through a simple literature review, extensive effort has been devoted by many different researchers and institutes to the exploration of the properties of complex media, their potentials in fabricating novel devices, and their potentials to overcome many preconceived limitations in different fields of electromagnetic wave theory, electronics, optics and acoustics. These researchers are primarily divided into two categories. The scientists in the first category are mainly theoreticians who are deeply involved in the foundations of complex media and are proposing new ideas and theories, while the second category of researchers are primarily involved in observing the properties of complex media and also fabricating devices consisting of complex structures.

The main question then, is, what is the definition of complexity in materials? In what sense can a medium be called complex? How complex can a medium be? How is it possible to quantify the complexity in materials? How can we analyze complex structures to see whether we are able to engineer electromagnetic fields? What are the possibilities in fabricating complex optical structures and realizing them?

Through common-sense notions, complexity in materials should have something to do with their structures or their chemistry. This can be the first step in defining a complex medium. From a structural point of view, the complexity of a medium can be either due to the complex shape of its constituent components or the order/organization of the components within the medium. Complexity in the shape of components can often make it very difficult to model the structure geometrically and/or mathematically or to handle the corresponding physical equations analytically or numerically.

The distribution of the constituent components can also cause a complex medium to have many different and sometimes anomalous properties. Existence of periodicity, for example, in the structure of a medium confers symmetrical properties which simplifies analysis and complexity of electromagnetic calculations and simulations. The composition of inclusions within a medium can also impart nonreciprocity to the complex medium, chirality being a prime example. Additionally, the use of active components may impose nonlinearity on the medium and affect its frequency response. The use of resonant type inclusions can also result in unusual physics which may not be normally observed in nature. So we see that the constituent components, i.e. their shapes or their organizations, in a medium can play an important role in the resultant properties of that medium. Besides the structural properties of a medium, its chemistry can cause interesting effects in its interaction with electromagnetic fields. Magnetoelectric materials [13], magnetodielectric materials [14], different types of ceramics [15], stealth materials [16], carbon nonotubes [17] and graphene [18] are examples of new kinds of materials which show interesting properties due to their chemistry. But unlike structural properties which emerge from composite materials, chemistry cannot really be engineered, so this is only a second concern in this work.

As alluded to above, we are preparing to define “complex media”. A complex medium is a composite consisting of either structural variation, or component variation, which additionally possesses four distinct characteristics. The first characteristic is anomalous physics. A complex medium often shows new physical properties which at first glance might seem to be in contradiction with conventional physical laws. But in fact, it can often lead to a relook at fundamental definitions and concepts of physics, bring lots of skepticism and controversy, and finally open its own space among other well-known topics. The second one is scarcity or non-existence in nature. A complex medium does not usually exist in nature. The unusual physics that is ultimately what we are trying to harness requires specific sets of conditions in a medium that would be improbable to occur naturally. The third feature of a complex medium is in its fabrication. The fabrication of a complex medium is typically tedious and needs a lot of care to meet a high standard of accuracy in its structure. Finally the fourth characteristic of a complex medium is its tight design requirements, both in calculation of its structure and in mathematical models describing it. Analysis of a complex medium usually needs a huge amount of computer memory, advanced Computer Process Units (CPUs) and many complicated mathematical formulations and theorems.

So, in general, complex media are called “complex” because of their remarkable physics, their unavailability in nature, their intricate structures and their unwieldy mathematical models. The abovementioned features for complex media may look a bit odd; for instance, one could claim that fabrication processes or mathematical models of many conventional materials and structures are also extremely complicated, but we do not call them "complex media". Likewise, many everyday objects, such as fruit juices, papers, and rubbers, etc., are extremely scarce in our universe as a whole, yet we do not call them "complex media". In this sense, we have to confess that no definition in science, including our definition, is totally conclusive; all proposed definitions generally come along with arguments, exceptions and inconsistencies. But we believe that if a man-made medium possesses *all* four characteristics above, that medium is definitely a complex medium. There might exist some exceptional complex media which do not have all of the above-stated characteristics. A very detailed analysis on definition of complex media can be found in [19].

We need to add one more point and that is our preference in terminology. We prefer the word "*medium*" for the purpose of our research to other words like "*material*" or "*structure*". The reason is that, as explained above, complex media owe their properties to their organizations and structures, or to their chemical ingredients, atoms and molecules. The first group could be called "structures" while the second group could be called "materials", so eventually the word "*medium*" is more general.

1.3 Geometrical Optics at a Glance

Geometrical Optics is the situation in optics where we practically solve a problem under the asymptotic situation that the wavelength goes to zero $\lambda \to 0$ and the energy transport can be described by the language of geometry [20]. This approximate theory is reliable only where the electromagnetic fields have rapid changes in their phases and gradual variations in their amplitudes.

For the sake of accuracy in the limit of geometrical optics, the media parameters (permittivity, permeability, conductivity, etc.) should fluctuate slowly in the scale of at least one wavelength or more precisely,

$$\frac{\left|\vec{\nabla}\cdot\left(\vec{\vec{\xi}}\cdot\vec{F}\right)\right|}{k_0} \ll 1, \quad \frac{\left|\sigma\vec{F}\right|}{k_0} \ll 1, \tag{1.1}$$

where $\vec{\vec{\xi}}$ is standing for the electromagnetic constitutive tensors, σ for the electromagnetic loss or gain, $\vec{F}$ for fields, $k_0 = \omega/c = 2\pi/\lambda$, ω is the angular frequency and c is the velocity of light in free space. As a matter of fact, the propagating fields can be expressed in terms of locally plane waves (quasi-plane waves). Based on Fermat's principle and Lagrangian calculus, they can be traced beautifully by pencils of rays [20, 21].

In the domain of geometrical optics we are allowed to write the electromagnetic fields as

$$\begin{cases} \vec{E}\left(\vec{r},t\right) = \vec{E}_0 \exp\left(ik_0\vec{k}\cdot\vec{r} - i\omega t\right) \\ \vec{H}\left(\vec{r},t\right) = \vec{H}_0 \exp\left(ik_0\vec{k}\cdot\vec{r} - i\omega t\right) \end{cases}, \tag{1.2}$$

where $\vec{k}$ is the wave vector and the magnitudes of both $\vec{E}_0$ and $\vec{H}_0$ are assumed to be approximately constant. Inserting the above expressions for $\vec{E}$ and $\vec{H}$ in Maxwell's equations and with the help of constitutive relations, we can find a dispersion relation in any medium [22]. The dispersion relation of a medium is basically called *Hamiltonian* of that medium. In the domain of geometrical optics with the use of the corresponding Hamiltonian $\mathcal{H}\left(\vec{r},\vec{k}\right)$ in a specific problem, we arrive at the Hamilton's set of differential equations,

$$\begin{cases} \dfrac{d\vec{r}}{d\tau} = \dfrac{\partial \mathcal{H}}{\partial \vec{k}} \\ \dfrac{d\vec{k}}{d\tau} = -\dfrac{\partial \mathcal{H}}{\partial \vec{r}} \end{cases}, \tag{1.3}$$

where τ is the ray tracing parameter. By solving the Hamilton's equations, we can find $\vec{r}(\tau)$ and $\vec{k}(\tau)$ which all together make a path in the space. Traditionally a ray of light is defined as a geometrical path which is optically the shortest possible path (*Fermat's principle*) and through which the energy is transported.

1.4 A Review of Transformation Optics

The concepts of conformal mapping [4] and coordinate transformation [5] were initially used to control light's path effectively and make an object invisible. Soon after these invisibility papers were published which essentially introduced the topic of *Transformation Optics*, they motivated a huge number of researchers to explore different methods and tools related to this topic to engineer the behavior of light in graded complex media. As will be reviewed briefly in this section (a detailed analysis on the media-geometry equivalence can be found in [21]), based on the invariance of the Maxwell equations through coordinate transformation, it is shown that media can resemble geometries and vice versa. Relying on this equivalence, we can assume predefined functionalities in a *virtual medium* and then through the use of a proper coordinate transformation we are able to find the constitutive parameters of the corresponding physical medium. This is actually the main concept of transformation optics. In recent years, transformation optics has been invoked extensively and therefore a wide range of applications, such as carpet cloaks [23], external cloaks [24], scattering enhancement [25], beam splitters [26], homogeneous nonmagnetic bends [27], field collimators [28], deep sub-wavelength waveguides [29], and super resolution devices [30] have been considered. In addition to all the efforts to realize the mentioned applications and many more, it has been shown that there exist several practical limitations on the performance of transformation optics devices [31].

Taking advantage of the mathematics of differential geometry [21], we can write the free space version of Maxwell's equations (in the MKS system) in curved space as,

$$\frac{1}{\sqrt{g}}\left(\sqrt{g}\,\mathbf{E}^i\right)_{,i} = \frac{\rho}{\varepsilon_0}, \tag{1.4}$$

$$\frac{1}{\sqrt{g}}\left(\sqrt{g}\,\mathbf{B}^i\right)_{,i} = 0, \tag{1.5}$$

$$e^{ijk}\mathbf{E}_{k,j} = -\frac{\partial \mathbf{B}^i}{\partial t}, \tag{1.6}$$

$$e^{ijk}\mathbf{B}_{k,j} = \frac{1}{c^2}\frac{\partial \mathbf{E}^i}{\partial t} + \mu_0 \mathbf{j}^i, \tag{1.7}$$

where $i, j, k = 1,2,3$, comma stands for vector differentiation, and $e^{ijk} = \pm\left(1/\sqrt{g}\right)\left[ijk\right]$ is the Levi-Civita tensor in which the plus sign is for the right handed and the minus sign is for the left handed coordinate system, and we use the Einstein summation convention on repeated indices. The symbol g is determinant of metric tensor g_{ij} of the corresponding coordinate system, $\left[ijk\right] = 1$ for an even permutation of 123, $\left[ijk\right] = -1$ for an odd permutation of 123, and $\left[ijk\right] = 0$ for any other case, ρ is the free charge density, and $\mathbf{j}$ is the free current density. Writing the Maxwell equations in terms of solely covariant forms of $\mathbf{E}$ and $\mathbf{B}$ and expressing the Levi-Civita tensor in terms of permutation symbols, we have,

$$\left(\sqrt{g}\, g^{ij}\mathbf{E}_j\right)_{,i} = \frac{\sqrt{g}\,\rho}{\varepsilon_0}, \tag{1.8}$$

$$\left(\sqrt{g}\, g^{ij}\mathbf{B}_j\right)_{,i} = 0, \tag{1.9}$$

$$[ijk]\mathbf{E}_{k,j} = -\frac{\partial\left(\pm\sqrt{g}\, g^{ij}\mathbf{B}_j\right)}{\partial t}, \tag{1.10}$$

$$[ijk]\mathbf{B}_{k,j} = \frac{1}{c^2}\frac{\partial\left(\pm\sqrt{g}\, g^{ij}\mathbf{E}_j\right)}{\partial t} + \mu_0\sqrt{g}\,\mathbf{j}^i, \tag{1.11}$$

Table 1.1. Comparison between Maxwell's equations in free space and in the equivalent macroscopic medium.

Free Space (Top: Flat Space, Bottom: Curved Space)	Macroscopic Medium (Cartesian Coordinates)
$\nabla\cdot\mathbf{E} = \rho/\varepsilon_0$ $\nabla\cdot\mathbf{B} = 0$ $\nabla\times\mathbf{E} = -\frac{\partial\mathbf{B}}{\partial t}$ $\nabla\times\mathbf{B} = \frac{1}{c^2}\frac{\partial\mathbf{E}}{\partial t} + \mu_0\mathbf{j}$	$\nabla\cdot\mathbf{D} = \text{ρ}$ $\nabla\cdot\mathbf{B} = 0$ $\nabla\times\mathbf{E} = -\frac{\partial\mathbf{B}}{\partial t}$ $\nabla\times\mathbf{H} = \frac{\partial\mathbf{D}}{\partial t} + \mathbf{J}$
$\left(\sqrt{g}\, g^{ij}\mathbf{E}_j\right)_{,i} = \sqrt{g}\,\rho/\varepsilon_0$ $\left(\sqrt{g}\, g^{ij}\mathbf{B}_j\right)_{,i} = 0$ $[ijk]\mathbf{E}_{k,j} = -\frac{\partial\left(\pm\sqrt{g}\, g^{ij}\mathbf{B}_j\right)}{\partial t}$ $[ijk]\mathbf{B}_{k,j} = \frac{1}{c^2}\frac{\partial\left(\pm\sqrt{g}\, g^{ij}\mathbf{E}_j\right)}{\partial t} + \mu_0\sqrt{g}\,\mathbf{j}^i$	$\mathbf{D}^i_{\ ,i} = \text{ρ}$ $\mathbf{B}^i_{\ ,i} = 0$ $[ijk]\mathbf{E}_{k,j} = -\frac{\partial\mathbf{B}^i}{\partial t}$ $[ijk]\mathbf{H}_{k,j} = \frac{\partial\mathbf{D}^i}{\partial t} + \mathbf{J}^i$

Now if we rescale the free charge and current densities as,

$$\text{ρ} = \sqrt{g}\,\rho, \tag{1.12}$$

$$\mathbf{J} = \sqrt{g}\,\mathbf{j}, \tag{1.13}$$

and also express the constitutive equations like

$$\mathbf{D}^i = \varepsilon_0 \varepsilon^{ij} \mathbf{E}_j , \tag{1.14}$$

$$\mathbf{B}^i = \mu_0 \mu^{ij} \mathbf{H}_j , \tag{1.15}$$

where the components of permittivity and permeability tensors are

$$\varepsilon^{ij} = \mu^{ij} = \pm\sqrt{g}\, g^{ij} , \tag{1.16}$$

then we see that Maxwell's equations in free space and in an arbitrary coordinate system or geometry are the same as Maxwell's equations in a macroscopic medium in the right handed Cartesian coordinate system. In other words, geometries are equivalent to media and vice versa. According to equation (1.16), these media are impedance matched to free space as the impedance of a medium is defined as $\sqrt{\mu / \varepsilon}$, i.e. the impedance of free space and the equivalent medium both are equal to one. The equivalence explained in this paragraph has been summarized in Table 1.1.

The expressed equivalence between the free space in Cartesian coordinates and the impedance matched macroscopic medium in arbitrary coordinates is the core idea behind the transformation optics. According to this equivalence, we can infer the transformation optics concept as follows. Let us assume a medium in an initial geometrical space. The medium can be free space and the initial medium can be assumed to be a right handed Cartesian coordinate system. Then if we transform the Cartesian system into a new arbitrary curved coordinate system, the electromagnetic fields will change and look like the electromagnetic fields in an equivalent macroscopic medium in a right handed Cartesian system. The former space is called *virtual space* and the later one is called *physical space*. More details on this interpretation can be found in [21]. On the basis of this equivalence, a recipe to design devices with extraordinary electromagnetic features can be proposed. A desired extraordinary formation of electromagnetic fields or light rays, which are not violating Maxwell's equations, can be thought of first. Then comparing the curved power flow lines or light rays with the straight lines in the globally flat right handed Cartesian space, a proper spatial transformation between these two spaces can be inferred. Then from the tabulated equivalence, the constitutive parameters of a physical space, which possesses the desired extraordinary electromagnetic features, can be obtained. An example of such a transformation is shown in Fig. 1.1.

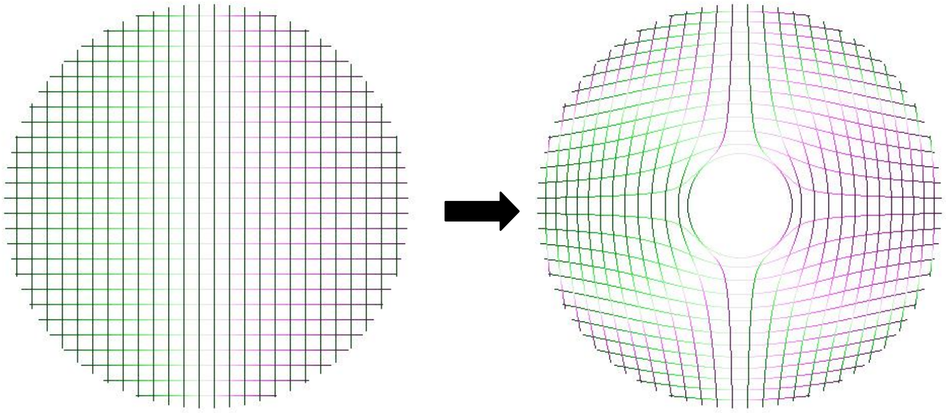

Fig. 1.1. An example of transformation of spaces.

In the previous formulation, the Maxwell equations in the right handed Cartesian coordinate system were compared with those in an arbitrary curved coordinate system. However, if we assume another curved space instead of a Cartesian one, then the relationship between the constitutive parameters of the macroscopic medium and the metric tensor of the equivalent geometry needs to be modified as,

$$\varepsilon^{ij} = \pm \frac{\sqrt{g}}{\sqrt{\gamma}} g^{ij} \varepsilon', \tag{1.17}$$

$$\mu^{ij} = \pm \frac{\sqrt{g}}{\sqrt{\gamma}} g^{ij} \mu', \tag{1.18}$$

where ε' and μ' are constitutive parameters of the virtual space and γ is determinant of the virtual space metric tensor. Finally if we transform a virtual space with coordinates $x^{i'}$ and constitutive parameters μ' and ε' to a physical space with coordinates x^i according to a transformation matrix $\mathbf{\Lambda} = \Lambda^i_{\ i'} = \left(\partial x^i / \partial x^{i'}\right)$, then the constitutive parameters in the physical space would be [21],

$$\varepsilon = \frac{\sqrt{g'}}{\sqrt{\gamma}} \frac{\mathbf{\Lambda}\left(\mathbf{g}'\right)^{-1}\mathbf{\Lambda}^T}{\det \mathbf{\Lambda}} \varepsilon', \tag{1.19}$$

$$\mu = \frac{\sqrt{g'}}{\sqrt{\gamma}} \frac{\mathbf{\Lambda}\left(\mathbf{g}'\right)^{-1}\mathbf{\Lambda}^T}{\det \mathbf{\Lambda}} \mu', \tag{1.20}$$

where $\mathbf{g}'$ is the metric tensor in the virtual space with determinant g', γ is the determinant of the metric tensor of the physical space, $\det \mathbf{\Lambda}$ is the determinant of $\mathbf{\Lambda}$ and T stands for the matrix transpose operator. Note that sometimes the transformation matrix is called the Jacobian matrix.

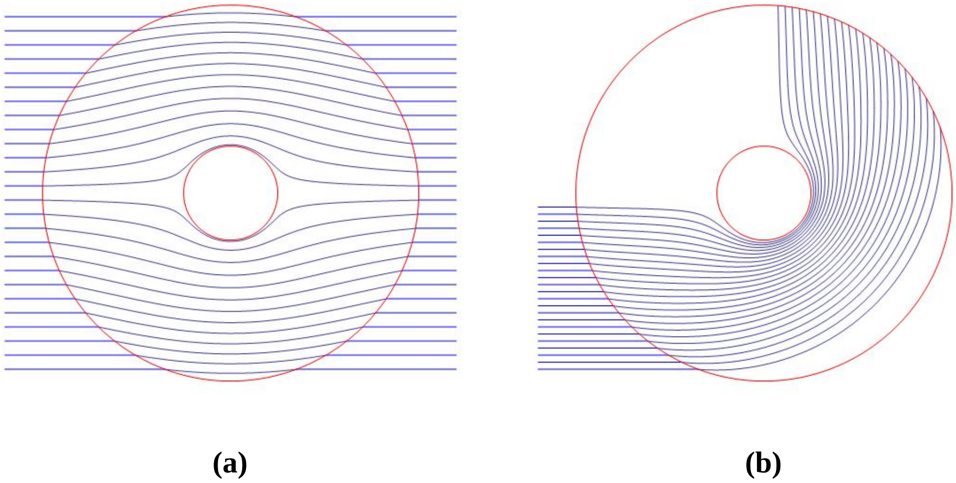

Fig. 1.2. Two examples of transformation optics based devices: (a) simple cloaking; (b) cloaking in addition to 90 degree bending.

Two examples of the use of transformation optics are given in Fig. 1.2. In both cases the transformations are done for cloaking an object inside the inner sphere. However, for the first case the virtual space is taken as vacuum while for the second one it is assumed to be 90-degree bending lens medium. Many other examples can be found in the literature as well.

1.5 Complementary Media and Space Folding

We would like to briefly review the concept of complementary media and the process of space folding. If the juxtaposition of two different media leads to a vanishing of the optical effects of both media, then these two media are called *complementary*. As shown with details in [32], if the constitutive profiles of two media are inverted mirror image of each other, the two media act like complementary media and cancel the presence of each other. In other words, if in the Cartesian coordinate systems, we have two slabs with constitutive parameters like,

$$\begin{aligned} &\varepsilon_1 = +\varepsilon(x,y), \qquad \mu_1 = +\mu(x,y), \qquad -d < z < 0, \\ &\varepsilon_2 = -\varepsilon(x,y), \qquad \mu_2 = -\mu(x,y), \qquad 0 < z < d, \end{aligned} \tag{1.21}$$

then these two slabs cancel out each other and the interface at $z = -d$ can be translated to $z = d$. However, for the non-Cartesian geometries (like spherical shells) we have to possibly transform them into the Cartesian slabs and figure out their mutual complementary slabs and finally transform the whole newly found stack of slabs back into the original geometry [32].

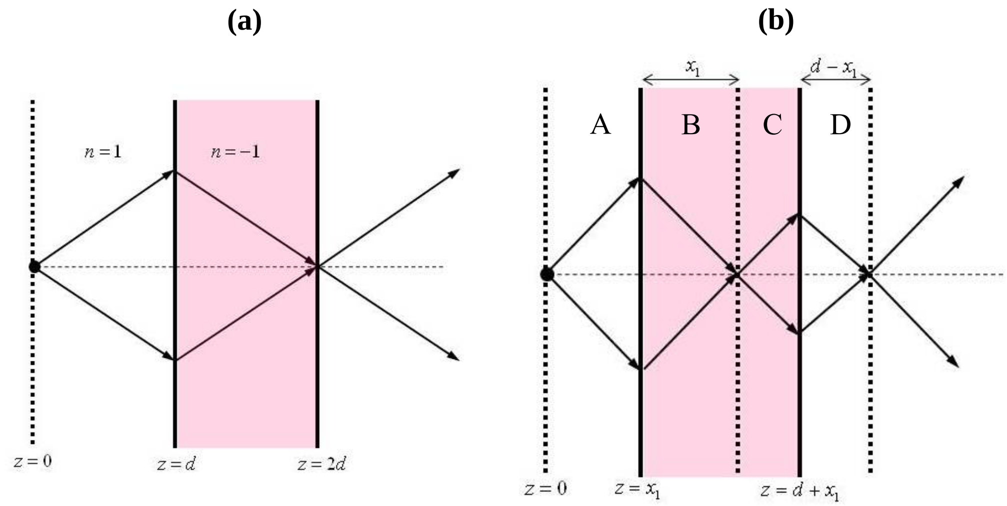

Fig. 1.3. (a) Cancelation of two complementary slabs, (b) Cascading two pairs of complementary slabs.

Now let us consider the simplest case of complementary media. Assume we have a homogeneous slab with thickness d and refractive index $n=-1$ (Fig. 1.3(a)). According to the theory of complementary media, this slab can make another slab of the same thickness but with $n=+1$ vanish. As a result, in Fig. 1.3(a) planes $z=0$ and $z=2d$ have identical optical characteristics and the space between them acts like a null space. This translation of the optical characteristics of planes can be employed effectively in imaging. According to Pendry *et al.*, since the space cancelation is complete, the loss of sub-wavelength information carried by exponentially decaying evanescent modes in the left slab can be compensated by the right slab and hence the finest optical features of the object located at $z=0$ can be imaged at $z=2d$; therefore, the image formed at the interface $z=2d$ is perfect [6, 21, 32]. But it might be more desirable in practical applications to construct the image somewhere outside the negative index slab. To do so, we should move the source closer to the negative index slab. If we move the source as much as x_1

closer to the negative slab, its perfect image is formed at a distance $d - x_1$ from the negative slab (Fig. 1.3(b)). In fact, as shown in Fig. 1.3(b), we are cascading the complementary slabs to move the perfect image further; slab "A" is cancelled out by slab "B" and slab "C" is cancelled out by slab "D".

If we use the complementary media in spherical geometries, not only do we obtain perfect imaging, but also the optical magnification of the image. As an example, suppose in Fig. 1.4 the medium in the shell $r_1 < r < r_2$ is complementary to the medium filling the shell $r_2 < r < r_3$. As shown in Fig. 1.4, if we put two point sources with a distance like x in between them on the surface of the sphere $0 < r < r_1$, then their perfect images form on the outer boundary of the region $r_2 < r < r_3$ and the distance between the point images is enlarged ($y > x$).

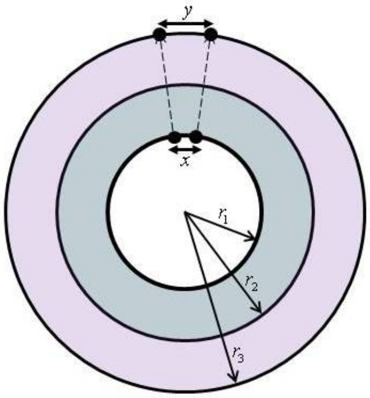

Fig. 1.4. Magnification of perfect images of two point sources in spherical geometry.

The idea of complementary media can be applied in designing magnifiers. Assume one side of a negative index slab ($n = -1$) of thickness d_1 is replaced by a mirror and a point source is located in vacuum at a distance like d_2 ($d_2 > d_1$) from the other side of the slab (see Fig. 1.5(a)). Since the negative slab cancels a slab of vacuum with thickness d_1, the optical properties of the mirror interface is the same as the plane "AB" shown in Fig. 1.5(a) and the mirror looks as if it were located closer to the source (at the distance $d_2 - d_1$). Now if we translate this scheme into a spherical geometry, as illustrated in Fig. 1.5(b), we extend the virtual image of an illuminated sphere to bigger spheres and hence increase its scattering cross section. The detailed analysis of the spherical magnifier, which is usually called a *superscatterer*, is provided in [25] and we avoid repeating that here.

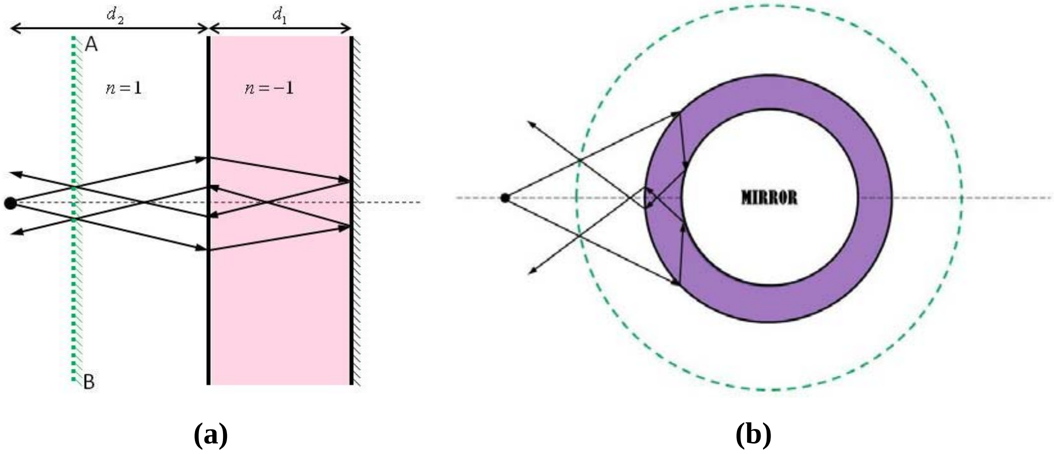

Fig. 1.5. Image magnification with the use of complementary media; (a) flat mirror, (b) spherical mirror.

At the end of this section, we would like to briefly consider the concept of space-folding and its role in the perfect imaging and superscattering. Interested readers are first referred to [21] in which the theory of space-folding and transformation media is explained comprehensively. First of all, let us consider the empty space in which the virtual space (x') and physical space (x) are overlapping totally and they follow a linear relation with a slope of one (Fig. 1.6(a)). Now assume we are allowed to accept a fold in the diagram of the virtual space versus the physical space as shown in Fig. 1.6(b). As shown in Fig. 1.6(b), within the fold each point of the virtual space is triple valued and the electromagnetic properties of the three corresponding points in the physical space are identical. It means that if we put a source on one of these points, what is seen in either of the other two points is perfectly like that which exists in the source point as if the source were tripled. According to the theory of transformation media, with the use of transformation

$$\begin{aligned} x' &= x'(x), \\ y' &= y, \\ z' &= z, \end{aligned} \tag{1.22}$$

the fold in the $x' - x$ diagram is equivalent to a medium with the profile parameters

$$\varepsilon = \mu = diag\left\{\frac{dx}{dx'}, \frac{dx'}{dx}, \frac{dx'}{dx}\right\}, \tag{1.23}$$

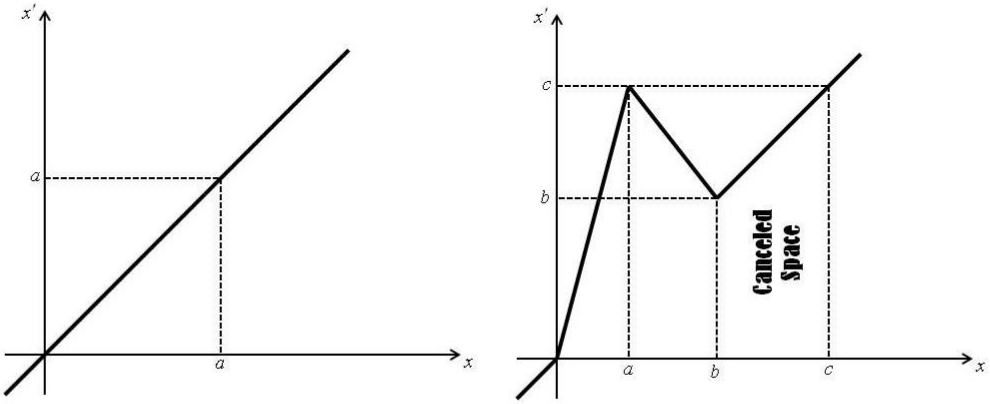

(a) **(b)**

Fig. 1.6. Virtual space versus physical space in (a) empty space, (b) folded space for perfect imaging

Note that both the virtual and physical spaces are Cartesian spaces and have similar metric tensors and the transformation matrix is $\Lambda = diag\{dx/dx', 1, 1\}$. The simplest transformation which provides us the desired space folding is $x'(x) = -x$. Using this transformation, according to equation (1.23), we get an isotropic profile with $n = -1$.

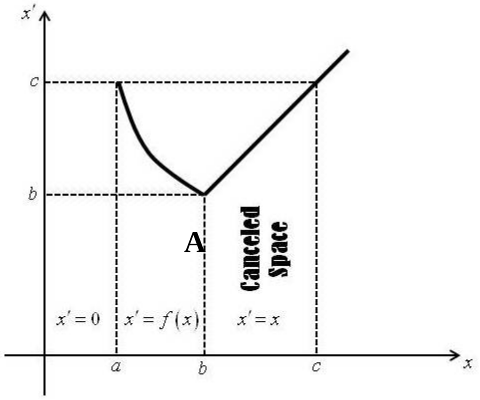

Fig. 1.7. Virtual space versus physical space in a folded space for superscattering.

The idea of superscattering can also be explained via the theory of space folding. As shown in Fig. 1.7, if we transform the space “A” backed by a mirror (at $x = a$) via a monotonically descending function like $x' = f\left(x\right)$ (where $df/dx < 0$ in region “A”), we will have a fold in the whole space and some part of the free space will be cancelled by region “A”. As a matter of fact, it seems as if the mirror were moved to $x = c$ and a sufficiently far object on the left side of region “A” sees its image closer than what really is in the mirror. As said earlier, the detailed study of this idea and how to use it in designing a spherical superscatterer directly was presented in [25]. However, in the Chapter 3 we propose a recipe in designing two and three dimensional superscatterers in a reverse manner and we will explore their properties by using ray tracing techniques as well as full-wave simulations.

1.6 Objectives

Our major objective in this PhD research is to understand deeply the interaction of light with complex media. Nowadays, there exists a rising interest among researchers to employ complex media and metamaterials to new optical applications and to explore the novel properties. Keeping the limitations of the usual materials and their capabilities in mind, researchers are seeking new types of media, which promise to overcome these limitations. Additionally, new sorts of applications are thought of and efforts are made to bring unusual phenomena into human life. However, there exist severe drawbacks in terms of loss, dispersion, and anisotropy in fabrication and application of known complex media. It is a worthwhile endeavour to consider the propagation of light inside complex media, to explain newly observed phenomena, and to explore novel behaviors.

As a matter of fact, we are motivated to develop analytical tools to study the physics of complex media and to investigate techniques that help us bring the behavior of light in complex media under our control. We are specifically interested in the strong tool of ray tracing for studying the interaction of electromagnetic waves and light rays with complex media in the domain of geometrical optics. Since in recent years, more attention has been paid to complex media and/or geometries, the ray tracing method has to be able to handle more sophisticated situations. In fact, we aim to generalize the well established method of ray tracing so that it can be applied to non-Euclidean or non-orthogonal coordinate systems; which will be carried out in this thesis. Meanwhile, we are also interested in photorealistic ray tracing of optical devices, which visualizes the physics behind designed devices in lifelike scenarios, which can enhance understanding and learning.

1.7 Contributions

Several contributions from this report can be mentioned. Invoking the mathematical machinery of differential geometry, a coordinate-free form for the eikonal equation and hence the Hamiltonian of a general purpose medium is derived to trace the trajectories of light within graded complex media. The generalized method works for both orthogonal and non-orthogonal coordinate systems. It is shown how the derived expressions can be simplified for biaxial and uniaxial media in orthogonal coordinate systems. With the help of algebraic manipulation, we factorize the Hamiltonian in biaxial media into two terms and break the corresponding Hamiltonian surface into two separate shells. Furthermore, in order to show the utility of the generalized formulation in a real case, both the isotropic and the uniaxially transmuted Eaton lens are studied. All these details were published in [33].

Using the transformation optics concept in the reverse direction, a formulation is given which can hold any arbitrary well-defined mathematical function to produce the constitutive parameters of a two or three dimensional superscatterer. According to the flexibility offered by the reverse method, different generating functions can be compared in terms of different features like isotropy, and inhomogeneity, etc. Consequently an isotropic two dimensional superscatterer is designed. Besides, utilizing the generalized ray tracing method, different photorealistic visualizations of the considered superscattering phenomena are depicted and the imaging aspects of the designed devices are reviewed. The obtained results in this section were published in [34] and presented in [35].

By using the simplified version of the factored biaxial Hamiltonian, we propose a recipe to control the formation of ray trajectories along two orthogonal planes with respect to their polarizations. This proposed method can be used in any orthogonal coordinate system. As an example, we consider the spherical geometry and we design a spherical graded-index dielectric device with four different functionalities at the same time. Based on this four-function device recipe, we design another spherical dielectric “Janus” device with two different functions along the two orthogonal planes for the unpolarized light. All these results were published in [36] and presented in [37, 38].

Traditionally a ray trajectory is the minimal path of energy transport which can be traced by the use of Lagrangian mathematics, provided the necessary conditions required by geometrical optics are met. But we show that in addition to the flow of energy, the flow of momentum can be traced along a ray trajectory and we propose a technique, that we call “force tracing”, to calculate the direction and magnitude of the optical force density within isotropic and anisotropic media under the geometrical optics approximation. By invoking the Lorentz force density acting on bound sources in a medium and employing the geometrical optics approximations, we derive regressive equations for the force field within isotropic and anisotropic media. In particular we show that the obtained optical force density in isotropic media is directly proportional to the curvature of the corresponding ray trajectory. For the case of anisotropic media the situation is more complicated and it is not easy to derive similar thing to what we have for isotropic media. To validate our analysis, we analyze the optical force density within two isotropic lenses, Eaton lens and Luneburg lens, and one anisotropic device, the Pendry cloak, and we show a reasonable agreement between our force fields under geometrical optics restrictions with those obtained by full-wave calculations.

Additionally, we talk about cases that the geometrical optics fails to calculate the optical force correctly. This is something which may lead to imposing new limitations on the borders of geometrical optics domain. All these facts and results were presented in [39] and have been accepted to be published as an article.

1.8 Organization

The outline of this thesis in the next chapters is as follows. In Chapter 2, we will generalize the ray tracing method in general coordinate-free style. We will review the optical Hamiltonian in isotropic, uniaxial and biaxial media. With the use of the generalized ray tracing technique, we will consider the Eaton lens as an example and we will transmute the optical singularity in this lens into a geometrical singularity.

In Chapter 3, based on the theory of complementary media and transformation optics, we will propose a reverse method to design 2D and 3D superscatterers. With the proposed reverse method, we will acquire a freedom to design superscatterers with different considerations which might be important from practical point of view. Cylindrical and spherical superscatterers will be designed and their behavior will be examined from full-wave and geometrical optics perspectives. Photorealistic rendering of the designed lenses will be demonstrated to show how they look like in a realistic situation.

In Chapter 4, we will take graded-index biaxial dielectrics into account. With the use of the biaxial Hamiltonian factorization (which will be shown in Chapter 2), we will introduce a method to control the functionalities of the possible polarizations along the principle planes in a biaxial dielectric device. As an example, we will consider the spherical geometry and we will design a radially symmetric device with four different optical functions at the same time. Furthermore, we will design a radially symmetric device with two different functions along its principle planes for the unpolarized light.

In Chapter 5, we will first review the Minkowski-Abraham dilemma on the momentum of light in media. Then based on the general time-averaged Lorentz force density and with the use of geometrical optics elements, we will introduce a new method, which we call force tracing, to trace the bulk and surface force fields along the trajectories of light rays in isotropic and anisotropic media. Under the realm of geometrical optics, we will also show the analytical relation between the Lorentz force density and the curvature of a ray in an isotropic medium. We will examine the validity of the force tracing technique in isotropic and anisotropic examples, as well

In Chapter 6, we will conclude the thesis and we will give several suggestions for future work.

CHAPTER 2 Generalization of Ray Tracing via a Coordinate-Free Approach

2.1 Introduction

Recently the advent of devices, such as perfect lenses [6, 7], invisibility cloaks [5, 40], and optical concentrators [41], has encouraged investigations into the foundations of optics, as well as attempts to engineer trajectories of light rays for any desired functionality. While it is relatively straightforward to calculate ray paths once one is given a certain index of refraction distribution in space $n(x,y,z)$, it is exceedingly difficult to go in the opposite direction—to command light to do certain things by engineering the refractive index profile. While the field of transformation optics continues to make headway toward this goal, the realm of geometrical optics represents a worthwhile field of investigation because of its potential to solve many problems to an acceptable degree of accuracy (invisibility cloaks with phase slips [42], for example, or universal retroreflection with Eaton lenses [21, 43, 44]), but with significantly eased materials requirements compared to devices designed with transformation optics that must preserve wave behavior.

In order to design devices in curved geometries, a comprehensive understanding of ray trajectory calculations via Hamilton's equations inside a medium is necessary. Hamilton's equations, which are useful in geometrical optics, classical and quantum mechanics, make a differential having roots in Fermat's principle, which states that a light ray always traces the extremal (optically minimum) path between two spatial points. The complexity of a medium, denoted by its constitutive relations and profiles, determines the degree of difficulty we face in dealing with such differential equations. For example, the solution of Hamilton's equations in a homogenous isotropic medium is so simple that the ray trajectory in such a medium is trivially a straight line (light in any uniform dielectric travels in a straight line). But in an anisotropic/inhomogeneous gradient medium the equations can be unwieldy to handle, and ray trajectories can curve and/or split.

It is worthwhile to note that anisotropic media in the limit of geometrical optics have been considered in the literatures for decades [45-49], and their physics in controlling the geometry of light is well understood. In [49], the problem of the Hamiltonian equation and ray tracing inside and at the surface of an inhomogeneous anisotropic medium have been studied comprehensively. However, the authors of [49] have considered only uniaxial media in Cartesian coordinates.

Nevertheless, the previous works on ray tracing were mostly in Euclidean space and were done under specific constraints. Being free of all these constraints, in this chapter the ray tracing technique is generalized and optical limit is analyzed with arbitrary anisotropy in arbitrary geometries. While the results to be demonstrated here could of course have been carried out in Cartesian coordinates instead, it is worthwhile to demonstrate Hamiltonian in arbitrary coordinates because of the great utility of working in other coordinate systems when designing optical components. This utility is also present in non-Euclidean spaces and has already resulted in interesting device design [40]. This is the primary motivation of this work.

Accordingly, we first briefly go through well-established geometrical optics theory and derive the Hamiltonian of a general purpose medium in a coordinate free manner. The derived expression works for both orthogonal and non-orthogonal coordinate systems, and we show how it can be simplified for biaxial and uniaxial media in orthogonal coordinate systems. Then we use the ray tracing process to determine the ray trajectories in different media. Taking advantage of ray tracing in birefringent media, we also show how transmutation of the index profile singularity can be converted into geometrical singularity [44].

2.2 Hamiltonian in a General Purpose Medium

If we consider the source-free Maxwell equations in a general form, we have

$$e^{ijk}\mathbf{E}_{k,j} = -\frac{\partial \mathbf{B}^i}{\partial t}, \tag{2.1}$$

$$e^{ijk}\mathbf{H}_{k,j} = \frac{\partial \mathbf{D}^i}{\partial t}, \tag{2.2}$$

$$\mathbf{D}^i{}_{,i} = 0, \tag{2.3}$$

$$\mathbf{B}^i{}_{,i} = 0, \tag{2.4}$$

where $i, j, k = 1, 2, 3$. It should be noticed that $\mathbf{E}$, $\mathbf{H}$ are one-forms and $\mathbf{D}$, $\mathbf{B}$ are vectors, respectively. If we consider ε and μ as relative permittivity and permeability tensors, respectively, then in a linear medium, we have

$$\mathbf{D}^i = \varepsilon_0 \varepsilon^{ij}\mathbf{E}_j, \tag{2.5}$$

$$\mathbf{B}^i = \mu_0 \mu^{ij}\mathbf{H}_j, \tag{2.6}$$

where ε_0 and μ_0 are the vacuum permittivity and permeability, respectively. In the geometrical optics limit, we can assume the electromagnetic fields as quasi-plane waves,

$$\mathbf{E}_j = \mathscr{E}_j \exp\left(ik_0 \mathbf{k}_m \mathbf{r}^m - i\omega t\right), \tag{2.7}$$

$$\mathbf{H}_j = \frac{1}{\eta_0} \mathscr{H}_j \exp\left(ik_0 \mathbf{k}_m \mathbf{r}^m - i\omega t\right), \tag{2.8}$$

where $m = 1,2,3$, $k_0 = \omega / c$, ω is the frequency, c is the light velocity in empty space, $\mathbf{k}$ is the wave vector, $\mathbf{r}$ is the position vector, and $\eta_0 = \sqrt{\mu_0 / \varepsilon_0}$. It should be noted that the quasi-plane-wave form (equations (2.7) and (2.8)) for the electromagnetic fields are true only in a small neighborhood of a given point. Farther from the point, the vector fields may depart the quasi-plane-wave form, for both the ray and the coordinate lines may be curved. With the use of equations (2.5) and (2.6), and after discarding several terms which are negligible under the geometrical optics approximation, equations (2.1) and (2.2) would be simplified as,

$$e^{ijk} \mathbf{k}_j \mathscr{E}_k - \mu^{ij} \mathscr{H}_j = 0, \tag{2.9}$$

$$e^{ijk} \mathbf{k}_j \mathscr{H}_k + \varepsilon^{ij} \mathscr{E}_j = 0. \tag{2.10}$$

Eliminating $\mathscr{H}$ from equations (2.9) and (2.10), we have,

$$M^{pk} \mathscr{E}_k = 0, \tag{2.11}$$

where $M^{pk} = \mathbf{k}_n \mathbf{k}_j \xi^{mi} e^{pn}{}_m e_i{}^{jk} + \varepsilon^{pk}$, $\xi = \mu^{-1}$, and all the subscripts or superscripts are from 1 to 3. Equation (2.11) is actually the well known eikonal equation in the wave vector domain, where the spatial derivatives of the eikonal have been replaced by the corresponding components of the wave vector. Avoiding a trivial solution to this equation, the determinant of M should be zero. As a matter of fact, the Hamiltonian is defined as

$$\mathcal{H} = \det\left(M\right) = \left[ijk\right] M^{(p)i} M^{(q)j} M^{(r)k} , \tag{2.12}$$

where $\left(pqr\right)$ is an even permutation of 123. It should be noted that the expressions obtained for the matrix M and the Hamiltonian are independent of any coordinate system and can be used in both orthogonal and non-orthogonal curvilinear coordinate systems. However, for non-orthogonal coordinate systems the basis vectors are not perpendicular to each other. Thus, the off-diagonal elements of the Levi-Civita tensor are not all zero, and the cross product of two basis vectors is not in the direction of the other basis vector. As a result, the expressions for the matrix M and the Hamiltonian would have more terms and would be much more complicated than those of the orthogonal one. Since the Levi-Civita tensor is different for various non-orthogonal coordinate systems, we cannot make our general Hamiltonian expression simpler for the non-orthogonal case. But as will be seen in the next sections, we can obtain simpler expressions for both biaxial and uniaxial cases in a general orthogonal coordinate system. It is also worth noting that for both dielectric ($\varepsilon = n^2$ and μ=the unit matrix) and impedance matched media, i.e. $\varepsilon = \mu = n$, where ε and μ are tensors in an orthogonal coordinate system, as shown in [50], the Hamiltonian would be

$$\mathcal{H} = \det\left(M\right) = \frac{1}{\det\left(n\right)}\left(\mathbf{k}^{\mathrm{T}} n \mathbf{k} - \det\left(n\right)\right)^2 , \tag{2.13}$$

which can also be derived from the given general expression (2.12) for the Hamiltonian (T stands for matrix transpose operation).

After finding the general expression for the Hamiltonian of a linear inhomogeneous anisotropic medium, to actually calculate the ray trajectories one can use the differential ray equations (Hamilton's equations) which are

$$\frac{d\mathbf{r}}{d\tau} = \nabla_{\mathbf{k}}\mathcal{H}\,, \tag{2.14}$$

$$\frac{d\mathbf{k}}{d\tau} = -\nabla_{\mathbf{r}}\mathcal{H}\,, \tag{2.15}$$

where τ parameterizes the ray paths. Hence we can find parametric ray trajectories by solving the above set of differential equations.

In addition to solving the above differential equations, one more step must be taken to be able to carry out ray tracing in a general medium. Since generally the interfaces between two media are not impedance matched, there would be a sort of reflection and/or refraction in the $\mathbf{k}$ vector trace at the boundaries. In cases where impedance matching at interfaces between different media exists, the incident rays would not be reflected, although there can still be refraction of the incoming rays at the boundary of the two optical media. In order to solve for the ray trajectories inside the medium of the transmitted rays, we need to be able to calculate the abrupt change in direction of the incident ray at the boundary. Therefore for the sake of completeness, one must solve this system of equations which results from boundary conditions at the interface:

$$\begin{aligned} &e^{ijk}\,\mathbf{k}_j^{inc}\,\hat{\mathbf{n}}_k = e^{ijk}\,\mathbf{k}_j^{ref}\,\hat{\mathbf{n}}_k = e^{ijk}\,\mathbf{k}_j^{tran}\,\hat{\mathbf{n}}_k\,, \\ &\mathcal{H}(\mathbf{k}^{tran}) = 0, \\ &\mathcal{H}_s(\mathbf{k}^{ref}) = 0, \end{aligned} \tag{2.16}$$

where $\mathcal{H}$ and $\mathcal{H}_s$ are the Hamiltonians of the device and the surrounding medium, respectively, and also $\mathbf{k}^{inc}$ is the wave vector of the incident ray, $\mathbf{k}^{ref}$ is the wave vector of the reflected ray, $\mathbf{k}^{tran}$ is the wave vector of the refracted ray inside the medium, and $\hat{\mathbf{n}}$ is the unit vector normal to the boundary. Solving this system of equations, we are able to find the components of the refracted ray or rays inside the material at an interface. It is also obvious that for anisotropic cases, the equation $\mathcal{H}(\mathbf{k}^{tran}) = 0$ has more than one result for $\mathbf{k}^{tran}$, and this means that multiple refraction and splitting of an incident ray into more than one ray inside the optical medium can occur. However, non-impedance matched media require more attention. During departure from a non-impedance matched medium, some parts of the rays would be reflected back into the incident medium. In order to obtain the reflected and transmitted wave vectors of the exiting rays, a system of equations similar to (2.16) should be solved as follows:

$$\begin{aligned} &e^{ijk}\,\mathbf{k}_j^{inc}\,\hat{\mathbf{n}}_k = e^{ijk}\,\mathbf{k}_j^{ref}\,\hat{\mathbf{n}}_k = e^{ijk}\,\mathbf{k}_j^{tran}\,\hat{\mathbf{n}}_k\,, \\ &\mathcal{H}(\mathbf{k}^{ref}) = 0, \\ &\mathcal{H}_s(\mathbf{k}^{tran}) = 0\cdot \end{aligned} \tag{2.17}$$

Finally we need to add that our general Hamiltonian study does not work for *Bi* media (bi-anisotropic, bi-isotropic and chiral) [22, 51] in which the constitutive equations are coupled to each other and modifications would have to be done in order to include such media in a future analysis, complicated as that may be. But because of their anomalies and additional degrees of freedom [51], chiral materials might be invoked to design more alluring devices in future.

2.3 Hamiltonian in Dielectric Biaxial Media in Orthogonal Coordinate Systems

It is known that in general the permittivity tensor ε of a reciprocal medium is symmetric and therefore we can always find a specific orthonormal coordinate system (i.e. principle coordinate system) in which the permittivity tensor can be written in the form of a diagonal matrix. So in the principle coordinate system $\{x_1, x_2, x_3\}$, for a dielectric (i.e. permeability is equal to one $\mu = 1$) biaxial medium we have

$$\varepsilon = \begin{pmatrix} n_1^2 & 0 & 0 \\ 0 & n_2^2 & 0 \\ 0 & 0 & n_3^2 \end{pmatrix} \cdot \tag{2.18}$$

Then the aforementioned matrix M would be simplified as

$$M = \varepsilon + K, \tag{2.19}$$

where $K = \begin{pmatrix} -(k_2^2 + k_3^2) & k_1 k_2 & k_1 k_3 \\ k_1 k_2 & -(k_1^2 + k_3^2) & k_2 k_3 \\ k_1 k_3 & k_2 k_3 & -(k_1^2 + k_2^2) \end{pmatrix}$ and k_i ($i = 1, 2, 3$) are the components of the wave vector. Hence the Hamiltonian would be

$$\begin{aligned} \mathcal{H} = \det\left(M\right) = k_1^4\, n_1^2 + \left(k_2^2 + k_3^2 - n_1^2\right)\left(k_2^2 n_2^2 + \left(k_3^2 - n_2^2\right) n_3^2\right) \\ + k_1^2 \left(k_2^2 \left(n_2^2 + n_1^2\right) - n_1^2 \left(n_2^2 + n_3^2\right) + k_3^2 \left(n_1^2 + n_3^2\right)\right), \end{aligned} \tag{2.20}$$

which is a quartic equation. The Hamiltonian in a biaxial medium is of degree four for each k_i and hence, in the wave vector domain it constructs a special surface which intersects each axis at four conjugate points. This surface, which is sometimes called wave surface or optical indicatrix [20], is the combination of a sphere and an oval. The three dimensional structure of the Hamiltonian surface and its intersections with each of the $k_i = 0$ planes are shown in Fig. 2.1. As seen in Fig. 2.1, the sphere and oval are concentric and for the case of $n_1 < n_2 < n_3$. In general these two meet each other at four points located in the $k_2 = 0$ plane. Similar to [52], we prefer to call these points diabolical points. The dashed lines connecting the origin to the diabolical points, as shown in Fig. 2.1(a), are along the optical axes. The direction of the optical axes can be found via the equations given in [53]. Except at the diabolical points, at all the other points the Hamiltonian concentric shells are distinguishable. Due to this fact, the phase matching process [22] makes any incident ray at the interface of the biaxial medium refract into at most two rays (double refraction), though in some occasions they may overlap or become evanescent. As discovered by Hamilton [54], the diabolical points are causes of one of the most interesting phenomena in optics, conical refraction. Since at the diabolical points there is a degeneracy in the direction of the normal to the Hamiltonian surface, the ray vectors at these points are infinite and build up a cone [20, 52]. Therefore if the wave vector of the incident light at the interface is along one of the optical axes, we will have a conical distribution of rays within the biaxial medium.

Putting the conical refraction aside, we should be able to factorize the Hamiltonian into two terms which can have nontrivial roots. Now we try to find these two terms following the method of Born and Wolf [20]. We define $\mathcal{H}_1$ as

$$\mathcal{H}_1 = k^2 \mathcal{H}, \tag{2.21}$$

where $k^2 = k_1^2 + k_2^2 + k_3^2$ and $\mathcal{H}$ was given in equation (2.20). With some simple algebraic manipulations, we can write

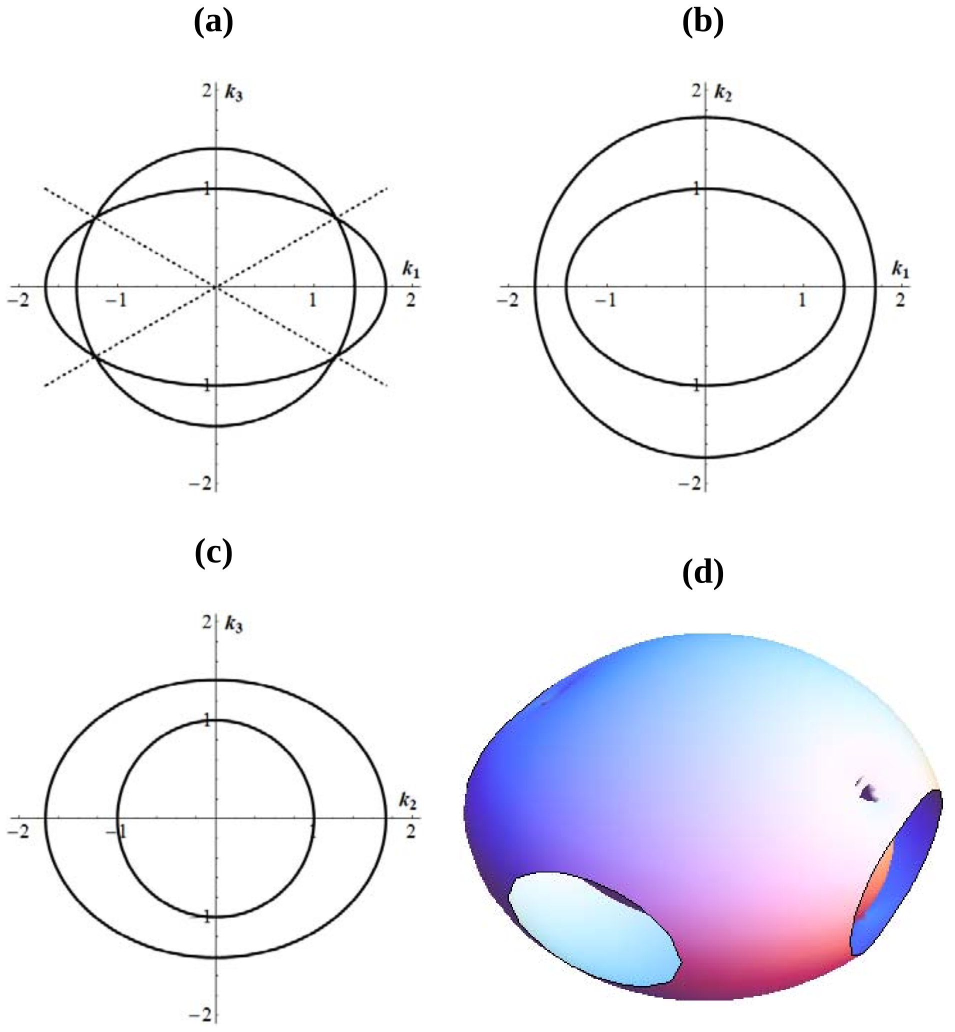

Fig. 2.1. Schematic of the Hamiltonian surface for a biaxial medium with $n_1 = 1$, $n_2 = \sqrt{2}$ and $n_3 = \sqrt{3}$; (a,b,c) intersection with $k_2 = 0$, $k_3 = 0$ and $k_1 = 0$ planes, respectively, (d) three-dimensional representation which is cut from the sides to show more details.

$$\begin{aligned}\mathcal{H}_1 = k_1^2 n_1^2 \left(n_2^2 - k^2\right)\left(n_3^2 - k^2\right) + k_2^2 n_2^2 \left(n_3^2 - k^2\right)\left(n_1^2 - k^2\right) \\ + k_3^2 n_3^2 \left(n_1^2 - k^2\right)\left(n_2^2 - k^2\right).\end{aligned} \tag{2.22}$$

Then by defining $g = n_2^2 - k^2$, $g_1 = n_1^2 - n_2^2$ and $g_3 = n_2^2 - n_3^2$, we have

$$\mathcal{H}_1 = g\left(g - g_3\right) k_1^2 n_1^2 + \left(g + g_1\right)\left(g - g_3\right) k_2^2 n_2^2 + g\left(g + g_1\right) k_3^2 n_3^2 . \tag{2.23}$$

Now we see that $\mathcal{H}_1$ is a second degree polynomial function of g, i.e. $\mathcal{H}_1 = \mathcal{H}_1(g)$. So we can express $\mathcal{H}_1$ as

$$\mathcal{H}_1 = G\left(g - g_a\right)\left(g - g_b\right), \tag{2.24}$$

where g_a and g_b are zeros of $\mathcal{H}_1$ and G is a nonzero constant. From equation (2.21), we have

$$\mathcal{H} = \frac{\mathcal{H}_1}{k^2} = \frac{G}{k^2}\left(g - g_a\right)\left(g - g_b\right). \tag{2.25}$$

Or we can express the Hamiltonian as

$$\mathcal{H} = \mathcal{H}_a \mathcal{H}_b \mathcal{H}_c , \tag{2.26}$$

where for $\mathcal{H}_a$, $\mathcal{H}_b$ and $\mathcal{H}_c$ we have

$$\mathcal{H}_a = \frac{k_1^2 n_1^2 + k_2^2 n_2^2 + k_3^2 n_3^2}{k^2}, \tag{2.27}$$

$$\begin{aligned} \mathcal{H}_{b,c} = -k^2 + n_2^2 + \frac{1}{2\left(k_1^2 n_1^2 + k_2^2 n_2^2 + k_3^2 n_3^2\right)} \Big\{ & \left(k_1^2 n_1^2 + k_2^2 n_2^2\right)\left(n_2^2 - n_3^2\right) \\ & -\left(k_2^2 n_2^2 + k_2^2 n_2^2\right)\left(n_1^2 - n_2^2\right) \pm \Big[k_1^4 n_1^4 \left(n_2^2 - n_3^2\right)^2 + \\ & \left(k_3^2 n_3^2 \left(n_1^2 - n_2^2\right) + k_2^2 n_2^2 \left(n_1^2 - n_3^2\right)\right)^2 + 2k_1^2 n_1^2 \left(n_2^2 - n_3^2\right) \\ & \left(k_3^2 n_3^2 \left(n_2^2 - n_1^2\right) + k_2^2 n_2^2 \left(n_1^2 - n_3^2\right)\right)\Big]^{0.5} \Big\}, \end{aligned} \tag{2.28}$$

and in equation (2.28) the plus sign is for $\mathcal{H}_b$ and the minus sign is for $\mathcal{H}_c$. Equations (2.26)-(2.28) show the factorized form of the Hamiltonian in a biaxial medium, where $\mathcal{H}_b$ describes one ray and $\mathcal{H}_c$ describes the behavior of the other ray. At diabolical points, we have $\mathcal{H}_b = \mathcal{H}_c = 0$ and the ray trajectories cannot be defined. By factorizing the Hamiltonian, we have actually divided the Hamiltonian surface into outer and inner shells with true optical axes and obviously their combination gives us the whole Hamiltonian surface. It might be interesting to see the shape of the Hamiltonian surface and the corresponding shells according to these factorized terms. Of course the whole shape of the Hamiltonian surface would be the same as that shown in

Fig. 2.1(d). But $\mathcal{H}_a \times \mathcal{H}_b$ and $\mathcal{H}_c$ individually have different shapes rather than the oval and the spherical forms mentioned in Fig. 2.1. The three dimensional schematics of these two shells and their intersections with the $k_i = 0$ planes are depicted in Fig. 2.2. It is seen that by combining the schematics in Figs. 2.2(a) and (b), we obtain the corresponding schematic shown in Fig. 2.2(c). As will be explained later in Chapter 4, the advantage we can take of such a factorization is the ability to control the biaxiality in order to design devices offering different responses to different polarizations. Functionalities which are not available in natural isotropic or anisotropic media can be readily achieved.

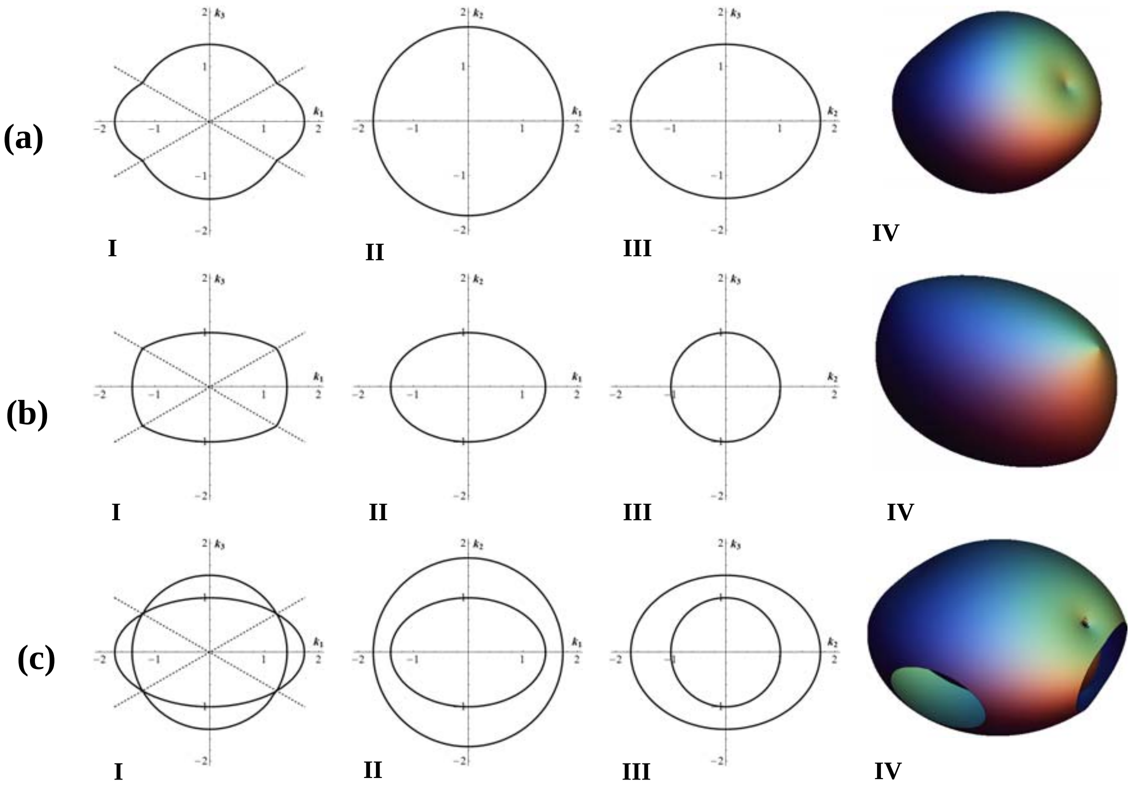

Fig. 2.2. Schematic surfaces of the factorized terms and the shape of the full Hamiltonian; the intersections and three dimensional shapes of (a,I-IV) $\mathcal{H}_a \times \mathcal{H}_b$, (b,I-IV) $\mathcal{H}_c$, (c,I-IV) $\mathcal{H} = \mathcal{H}_a \times \mathcal{H}_b \times \mathcal{H}_c$. Note that the schematic in c(IV) is cut from the sides to show more details.

2.4 Hamiltonian in Dielectric Uniaxial Media in Orthogonal Coordinate Systems

The case of the dielectric uniaxial material leads to significant simplification in the Hamiltonian equation. By letting $n_2 = n_3 = n_o$ and $n_1 = n_e$ in (2.20), we have for a dielectric uniaxial medium,

$$\mathcal{H} = \det\left(M\right) = \mathcal{H}_o\mathcal{H}_e = \left(k_1^2 + k_2^2 + k_3^2 - n_o^2\right)\left(k_1^2\, n_e^2 + \left(k_2^2 + k_3^2 - n_e^2\right)n_o^2\right), \quad (2.29)$$

which means that the incident wave to such a medium is decomposed into ordinary ($\mathcal{H}_o = 0$) and extraordinary ($\mathcal{H}_e = 0$) waves. As seen, the uniaxial Hamiltonian equation consists of spherical and ellipsoidal equations in *k*-space, respectively, and they meet each other at $(0, 0, \pm n_o)$. It is interesting to note that regardless of the orthogonal coordinate system, in which the birefringence of a medium occurs, we always have two Hamiltonians and "ray splitting" always occurs, although sometimes the rays may become degenerate.

2.5 Example: Transmutation of the Singularity in the Eaton Lens

On the basis of the general formulation of the ray tracing in the previous sections, we analyze several devices in the rest of this report. However, in this section we apply our general Hamiltonian and related mathematics in a real case as an example and try to demonstrate all the important features. To do so, we take the Eaton lens into account. The Eaton lens is a perfect retro-reflector that reflects back all incident light rays omnidirectionally. The index profile of the Eaton lens is spherically symmetric and is a function of *r* if we take the center of the lens as the origin,

$$n(r)=\sqrt{\frac{2a}{r}-1}, \tag{2.30}$$

where a is the radial extent of the Eaton lens, $r=|\mathbf{r}|$, and we let it equal 1 for our study. Since the device is spherically symmetric, the angular momentum of the rays is a fixed vector and all the incident rays that lie on a plane do not leave that plane when travelling inside the device [21, 55]. Hence, for simplicity, we take the $\theta=\pi/2$ plane in spherical coordinate (r,θ,ϕ) as one plane of the rays to examine. As the profile index is isotropic, the Hamiltonian is

$$\mathcal{H}=k_r^2+k_\phi^2-n(r)^2. \tag{2.31}$$

Solving the differential Hamilton's equations (2.14) and (2.15) with proper initial conditions, we obtain the ray trajectories as shown in Fig. 2.3. It can be shown that the rays inside the lens are actually, as it is observed, ellipses with a common focal point [21, 55].

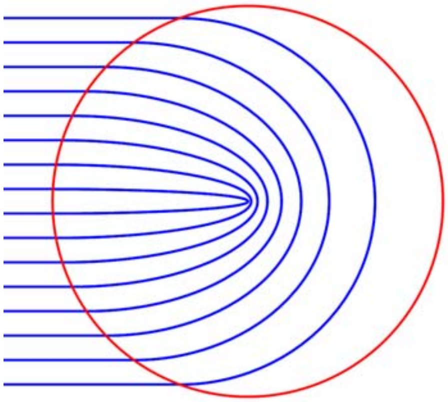

Fig. 2.3. Ray trajectories inside an isotropic Eaton lens.

It is obvious that due to uniform deflection of light rays, the Eaton lens profile has a singularity at the origin, and as r tends to zero, the refractive index goes to infinity and the speed of light vanishes. In order to avoid such a singularity, we need to transmute the material singularity into geometrical singularity, which is more feasible from practical point of view, as explained in [43, 44]. It should be noted that the idea behind this transmutation is based on the theory of transformation optics, which was explained with more details in the previous chapter. However, for transmutation of the singularity, a coordinate transformation from *r-space* to *R-space* is needed. After the still-undecided coordinate transformation and rescaling [44], diagonal tensor elements (in spherical coordinates) are as follows:

$$\varepsilon_{(ii)}\left(R\right)=\left\{\frac{n^2r^2}{R^2},n^2\left(\frac{dr}{dR}\right)^2,n^2\left(\frac{dr}{dR}\right)^2\right\}, \tag{2.32}$$

$$\mu_{(ii)}\left(R\right)=\left\{\frac{r^2}{R^2}\left(\frac{dR}{dr}\right)^2,1,1\right\}, \tag{2.33}$$

where n is the original profile index and $R\left(r\right)$ is the transformation function, and off-diagonal elements of the transformed permittivity and permeability are zero. It is seen that transmutation of the singularity inevitably inserts birefringence into the optical medium. It should be noted that despite the fact that the transmutation takes care of the singularity, it is clear that a dielectric cannot be used to implement this device unless $\mu_{rr}=1$ (clearly not the case). So if we force $\mu_{rr}=1$, we actually sacrifice one polarization, and the performance of the lens is preserved only for one of the two possible polarizations, i.e. in-plane and out-of-plane polarization.

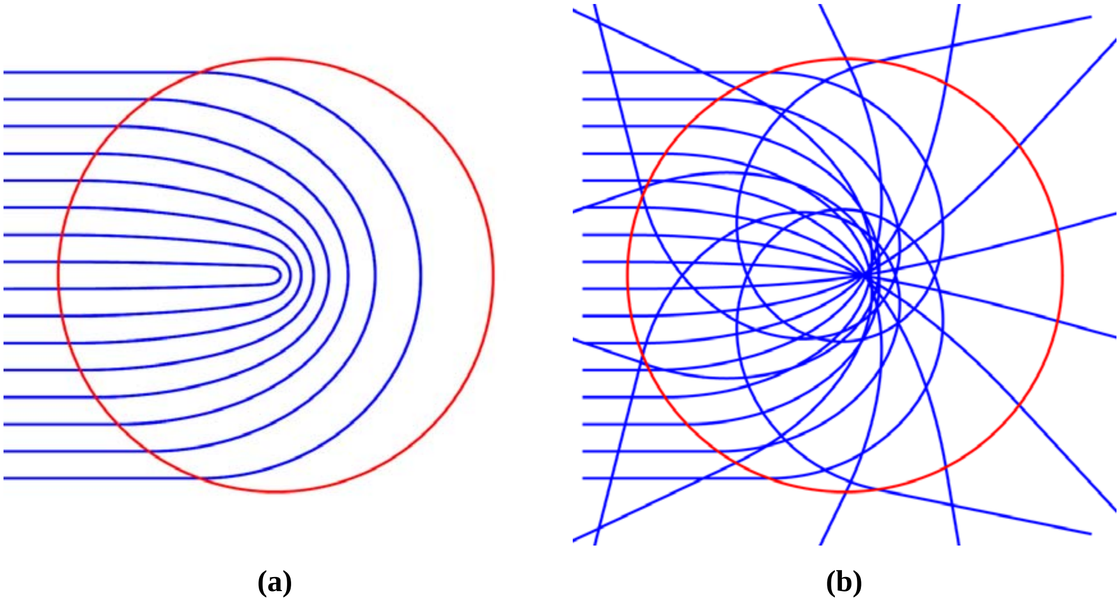

Fig. 2.4. Ray trajectories inside the Eaton lens transmuted via $R(r)$ for the (a) in-plane polarization and (b) out-of-plane polarization.

Transmuting the refractive index profile and accepting the expense of one polarization by allowing $\mu_{rr}=1$, we can find the ray trajectories by solving the four coupled differential equations coming out of the Hamiltonian of the transformed medium,

$$\mathcal{H}=\left(\varepsilon_{rr}k_r^2+\varepsilon_{\phi\phi}k_\phi^2-\varepsilon_{rr}\varepsilon_{\phi\phi}\mu_{\theta\theta}\right)\left(\mu_{rr}k_r^2+\mu_{\phi\phi}k_\phi^2-\mu_{rr}\mu_{\phi\phi}\varepsilon_{\theta\theta}\right), \tag{2.34}$$

where after normalization $\varepsilon_{rr}=n_r^2$, $\varepsilon_{\theta\theta}=\varepsilon_{\phi\phi}=n_\phi^2$, $n_r=n(R)r(R)/R$, $n_\phi=n(R)(dr/dR)$, $\mu_{\theta\theta}=\mu_{\phi\phi}=1$, $\mu_{rr}=(r/R)^2(dR/dr)^2$. However, as said earlier we are interested only in dielectrics, we assign $\mu_{rr}=1$; therefore the performance of the out-of-plane polarization (the second term on the right hand side of equation (2.34)) would be disturbed. Since the Eaton lens is a spherically symmetric device, we choose $R(r)=\sqrt{r}(r+1)/2$ as the transformation function to give a reflectionless boundary at the lens edge and therefore we obtain the ray equations by solving equations (2.14)-(2.16) as shown in Fig. 2.4. It is seen that the Eaton lens acts like a perfect retro-reflector for the in-plane polarization, while the out-of-plane polarization is sacrificed. The transmuted $n_r(R)$ and $n_\phi(R)$ versus R are plotted in Fig. 2.5, where they do not demonstrate any singularity and achieve the value of one at the boundary $R=1$, which is required for impedance matching.

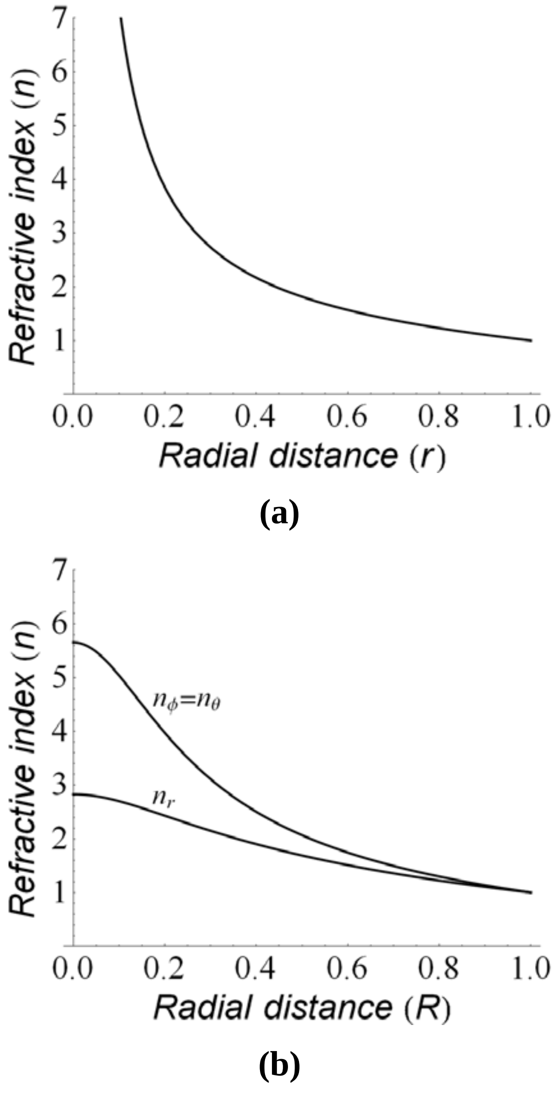

Fig. 2.5. Plots of refractive indices (a) before transmutation $n(r)$ and (b) after transmutation $n_r(R)$ and $n_\phi(R) = n_\theta(R)$.

2.6 Conclusions

The Hamiltonian equation is extremely important in determining the behavior of light rays in an optical device. The demand for anisotropic materials, extensive application of transformation optics, and increasing use of structures with unusual non-flat topologies, all in all, have made us resort to non-Euclidean and/or non-orthogonal coordinate systems. Accordingly, a comprehensive understanding of Hamiltonian optics and ray equations in a general curvilinear geometry independent of any coordinate system is required. In this chapter, we demonstrated the Hamiltonian equation of a propagating wave through a general purpose medium and in a coordinate-free style. Biaxial and uniaxial media were considered as two special cases, and the validity of our analysis was shown for the transmuted Eaton lens.

The presented formulation in this chapter is the core of all calculations in this thesis and will be employed in analysis and design of different complex devices in the subsequent chapters. In addition to the simple ray tracing, photorealistic ray tracing is possible using the described method here and the next chapter will expand upon the applicability of these two in illustrating the performance of graded-index superscatterers.

CHAPTER 3 Design and Photorealistic Rendering of Graded-Index Superscatterers

3.1 Introduction

As mentioned earlier in Chapter 1, scattering enhancement and image magnification generally, are one of the proposed applications of transformation optics. Enhancement of scattering and absorption of light by optically small particles, i.e. particles which can be circumscribed in the sphere of radius $\lambda_0 / 2\pi$, is of fundamental interest from both the theoretical and practical points of view [56-59]. It is known that most of the energy of the light incident into a small particle is mainly stored in the near field and the radiation efficiency of such a particle is extremely low [58]. In order to overcome this undesirable near field energy storage, different techniques have been proposed [25, 56-59]. Recently the method of transformation optics on the basis of the concept of complementary media was invoked by Yang et al. [25] and followed by Wee and Pendry [59] to enrich the scattered or absorbed energy by a small particle, though their approach relies on the initial knowledge of the spatial transformation function.

In this chapter, a reverse method based on a spatial transformation will be proposed to design a general superscatterer. This will make an excellent example in which the machinery developed and described in detail in Chapter 2 can be applied. In fact it will be shown that any well defined function can act as a generating function to produce the required parameters for a superscatterer constitutive profile. Accordingly, the complementary media can be uniquely determined without the prior knowledge of the corresponding spatial transformation. However, the resultant superscatterer profile is not unique and this reverse recipe is inclusive of all possible parametric profiles, and as a matter of fact, it can lead us to obtain the superscatterer's constitutive profile for a desired field pattern in the complementary media. Thus, different generating functions can be examined and the generated superscatterer index profiles can be compared in terms of various factors like homogeneity, isotropy, non-singularity, ease of fabrication, cost, and loss. For instance, this concept provides a straightforward way to investigate the constitutive parameters of the superscatterer, which will be employed to obtain an isotropic retro-reflecting superscatterer with inhomogeneous negative refractive index.

So in this chapter, the mathematical formulation of the reverse method will be presented in a regressive manner for both 2D and 3D structures. Along with these calculations, several full wave simulations of the designed superscatterers will be provided, in which different generating functions will be examined. The required parameters for the design of an isotropic superscatterer will be derived and its imaging characteristics will be studied. In addition to full wave simulations, ray tracing analysis will be conducted to provide a better estimation on how the designed superscatterers actually work. On the basis of the calculated ray trajectories, animations will be illustrated to give an idea on how the superscatterer may look like in real life.

3.2 Two Dimensional Superscatterer Design

First, let us assume that a circular region ($r \leq a$) covered by complementary media ($a \leq r \leq b$) in physical space $\Omega(r)$ is transformed from a circular region ($r' \le c$) in virtual space $\Omega'(r')$ via an unknown transformation function. The constitutive parameters of the complementary media are assumed to be equal for impedance matching, i.e. $\vec{\varepsilon}(r) = \vec{\mu}(r) = \alpha_r \hat{r}\hat{r} + \alpha_\phi \hat{\phi}\hat{\phi} + \alpha_z \hat{z}\hat{z}$. Since the transformation is in the radial direction, the Jacobian matrix of the transformation is diagonal, though we still have no information about the transformation. The relative parameters of the complementary media can be obtained as $\vec{\varepsilon} = \vec{\mu} = \vec{A} \cdot \vec{A}^{\mathrm{T}} \big/ \det\left(\vec{A}\right)$, where $\vec{A} = \partial(r, \phi, z) / \partial(r', \phi', z')$ is the Jacobian matrix [21, 60] $\left(r', \phi', z'\right)$ and $\left(r, \phi, z\right)$ represent the virtual and physical spaces, respectively. Then three principle values of $\vec{\varepsilon}\left(r\right)$ and $\vec{\mu}\left(r\right)$ can be obtained as, $\alpha_r = \dfrac{r' \mathrm{d}r}{r \mathrm{d}r'}$, $\alpha_\phi = \dfrac{1}{\alpha_r}$ and $\alpha_z = \dfrac{r' \mathrm{d}r'}{r \mathrm{d}r}$. By making use of the identities $\alpha_r \alpha_z = (r'/r)^2$ and $r\sqrt{\alpha_r \alpha_z}\,\partial[r\sqrt{\alpha_r \alpha_z}\,] / \partial r = r\alpha_z$, one can obtain

$$r'^2 = C_0 + 2\int_a^r r_1 \alpha_z\left(r_1\right) dr_1 , \tag{3.1}$$

where C_0 is a constant to be determined. Due to the folding configuration ($r' = c$ when $r = a$), from equation (3.1) we have $C_0 = c^2$. The other constraint ($r' = b$ when $r = b$) imposed by the radial folding leads to the normalization condition

$$\int_a^b r_1 \alpha_z\left(r_1\right) dr_1 = \frac{b^2 - c^2}{2} \cdot \tag{3.2}$$

Here, we introduce the generating function $g\left(r\right)$, which is proportional to $\alpha_z(r)$, i.e. $\alpha_z(r) = d_0 g(r)$, where d_0 is an arbitrary constant. Substituting

$\alpha_z(r) = d_0 g(r)$ into equation (3.2), we can obtain

$$d_0 = \frac{b^2 - c^2}{2\int_a^b r_1 g(r_1)\, dr_1} \cdot \tag{3.3}$$

Thus $\alpha_z(r)$ can expressed as

$$\alpha_z(r) = \frac{(b^2 - c^2) g(r)}{2\int_a^b r_1 g(r_1)\, dr_1}. \tag{3.4}$$

From the aforementioned identity $\alpha_r \alpha_z = (r'/r)^2$ and equation (3.4), $\alpha_r(r)$ can be determined

$$\alpha_r(r) = \frac{c^2 + 2\int_a^r r_1 \alpha_z(r_1)\, dr_1}{r^2 \alpha_z(r)}. \tag{3.5}$$

The unknown coordinate transformation for the corresponding complementary media can, therefore, be written as

$$r' = \sqrt{c^2 + 2\int_a^r r_1 \alpha_z(r_1)\, dr_1} \cdot \tag{3.6}$$

To validate this method, we select a specific generating function $g(r) = r^n$ ($n = 0, \pm 1, \pm 2, \ldots$) as the representative demonstration. Then $\alpha_z(r)$ can be derived as

$$\begin{aligned} \alpha_z(r) &= \frac{(n+2)(b^2 - c^2) r^n}{2(b^{n+2} - a^{n+2})} \quad \text{when } n \neq -2, \\ \alpha_z(r) &= \frac{b^2 - c^2}{2r^2 \ln(b/a)} \quad \text{when } n = -2 \cdot \end{aligned} \tag{3.7}$$

The corresponding coordinate transformation can be expressed as

$$
\begin{aligned}
r' &= \sqrt{c^2 + \frac{\left(b^2 - c^2\right)\left(r^{n+2} - a^{n+2}\right)}{b^{n+2} - a^{n+2}}} && \text{when } n \neq -2, \\
r' &= \sqrt{c^2 + \frac{\left(b^2 - c^2\right)\ln\left(r / a\right)}{\ln\left(b / a\right)}} && \text{when } n = -2.
\end{aligned}
\tag{3.8}
$$

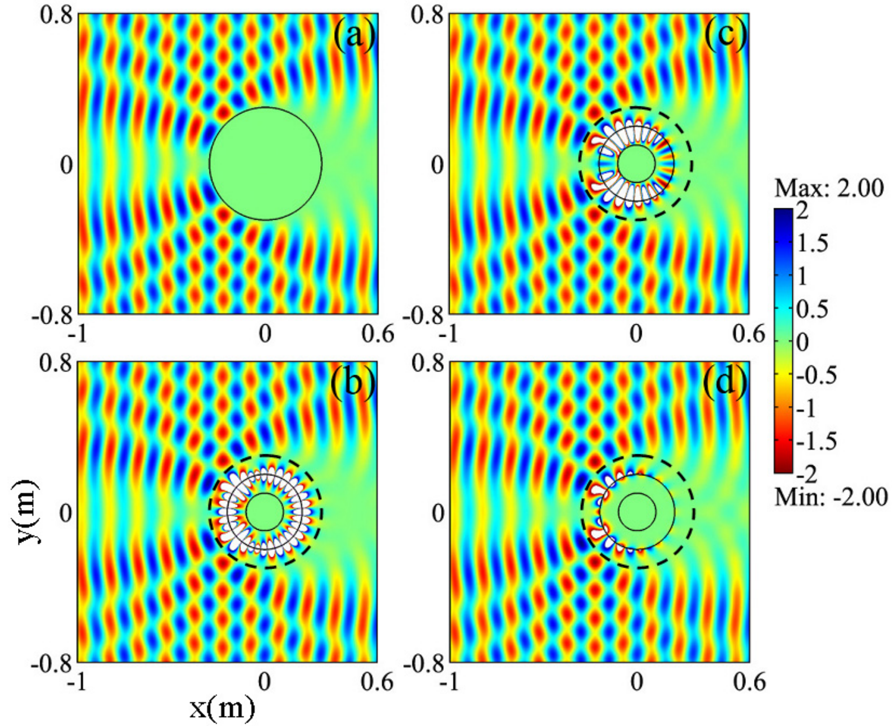

Fig. 3.1. Snapshots of the total electric fields for the reversely designed superscattering magnifier; (a) bare circular PEC with radiuse *c*, (b) $n = -2$, (c) $n = -10$, (d) $n = 10$. And also $a = 0.1$ m, $b = 2a$, and $c = 3a$.

The magnifiers designed via the proposed reverse method with the generating functions corresponding to different values of n, $g\left(r\right) = 1/r^2$ (i.e. $n = -2$), $g\left(r\right) = 1/r^{10}$ (i.e. $n = -10$), and $g\left(r\right) = r^{10}$ (i.e. $n = 10$), are shown in Figs. 3.1(b-d), respectively. It is seen that the electric fields outside the black dashed circular lines ($r > c$) for these three types are equivalent to that of the bare Perfect Electric Conductor (PEC). In other words, the scattering pattern of a small circular PEC ($r = a$) covered by the designed complementary media is the same as that of the bigger one ($r = c$).

Fig. 3.1(d) reveals that in comparison to the other two cases, the generating function with $n = 10$ gives the smallest scattering intensity inside the complementary medium and the area of white flecks is also minimal and confined just near the outer boundary ($r = b$). It can be explained that the implied spatial transformation corresponding to the case of the generating function $n = 10$ folds and compresses more virtual space into the area near the outer boundary in physical space, which can verified by plotting equation (3.8) for the different values of n (see Fig. 3.2).

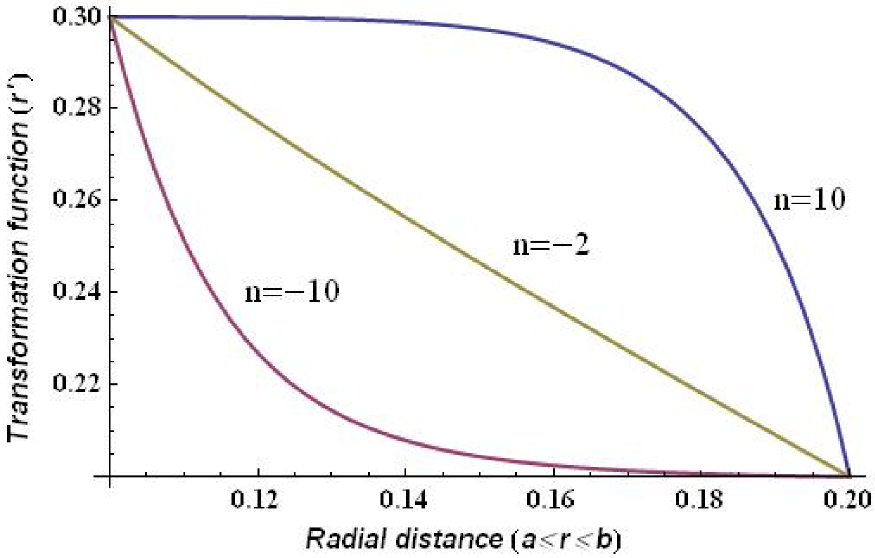

Fig. 3.2. Comparison between the transformation functions for three values of *n*. It is seen that the ($n = 10$) case is more uniform and hence compresses more virtual space near the out boundary compared to two other cases.

This reverse recipe can thus be a powerful tool to design isotropic and nonsingular magnifiers with retro-reflecting and imaging features by use of graded negative refractive index. From the condition $\alpha_\phi = 1/\alpha_r$, the isotropy imposes that $\alpha_r = \pm 1$ in equation (3.5). By taking the derivative of

$\pm r^2\alpha_z(r) = c^2 + 2\int_a^r r_1\alpha_z(r_1)dr_1$ with respect to r, one thus has $g(r) = T$ (T is a constant) or $r^2 g'(r) + 4rg(r) = 0$, respectively. In the case of $g(r) = T$ corresponding to $\alpha_r = +1$, the isotropy (under one polarization) implies $Td_0 = c^2 / a^2$. However, the aforementioned normalization condition $d_0 = \left(b^2 - c^2\right) \Big/ \left(2\int_a^b r_1 g(r_1) dr_1\right)$ leads to $Td_0 = \left(b^2 - c^2\right) / \left(b^2 - a^2\right)$, which is contradictory. Hence, $g(r) = T$ is not possible for isotropic designs. In the case of $r^2 g'(r) + 4rg(r) = 0$ corresponding to $\alpha_r = -1$, the generating function becomes $g(r) = 1/r^4$. After solving for the normalization, it is found that only when $c = b^2/a$, one can obtain isotropic complementary medium $\alpha_r = \alpha_\theta = -1$ and $\alpha_z(r) = -b^4/r^4$. Therefore, an isotropic negative index magnifier can be realized for one polarization, e.g. $\varepsilon = -1$ and $\mu = -b^4/r^4$ for TM incidence and also $\varepsilon = -b^4/r^4$ and $\mu = -1$ for TE incidence. It is obvious that these isotropic profiles are nonsingular.

To emulate how such an isotropic design behaves in practice, we took advantage of our developed method to carry out a ray tracing (photorealistic) process. Photorealistic ray tracing can also help foresee how a specific imperfection in media affects the device performance, though we only use it to visualize ideal performance in this chapter. Fig. 3.3(a) indicates that upper and lower rays intersect each other twice in the vicinity of the outer boundary ($r = b$) owing to the negative refractive index of the isotropic shell. Fig. 3.3(b) demonstrates the imaging properties in which only the images before and after paraxial rays intersections are shown. It reveals that the image inside the isotropic shell (A”B”C”D”) is flipped. But the image outside the shell (A’B’C’D’) is preserved, which is in contrast to the Eaton lens, flipping the image upside down and is a positive point for our design.

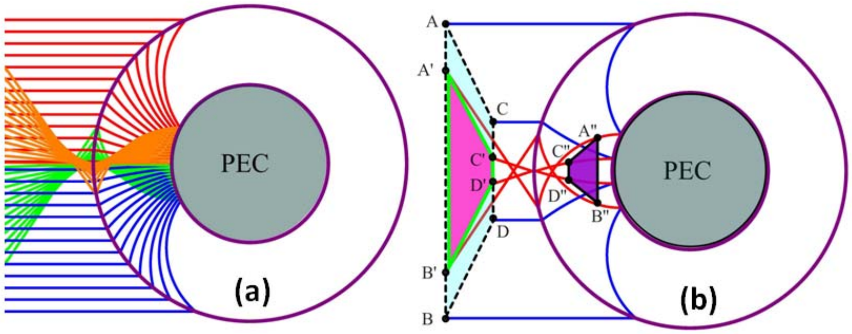

Fig. 3.3. Ray tracing of the isotropic negative index shell whose parameters are $\varepsilon = -b^4 / r^4$ and $\mu = -1$, $a = 0.2$ m, $b = 2a$ and $c = b^2 / a$. (a) ray trajectories of light before hitting the PEC (red and blue) , after being reflected by the PEC (orange and green); red and orange lines correspond to rays in the upper half-space; blue and green lines for the lower half-space. (b) the images inside and outside the isotropic shell.

In Fig. 3.4(a), a bare PEC rod of radius $r = b$ is placed inside a waveguide, so the wave is partially transmitted via the openings between the rod and the waveguide walls, as shown in Fig. 3.4(c). However, in Fig. 3.4(b), when a smaller PEC rod of radius $r = a$ coated by the designed isotropic shell ($a < r < b$) effectively behaves like a magnified PEC rod of radius $r = b^2 / a$. Therefore, even though the coated structure in Fig. 3.4(b) has its outmost radius physically identical to that in Fig. 3.4(a), it blocks whole the waveguide and the transmitted power through the waveguide drops down dramatically (the waveguide width is assumed to be $2b^2/a$). This is verified from the field distribution in Fig. 3.4(b) and the transmission spectra in Fig. 3.4(c).

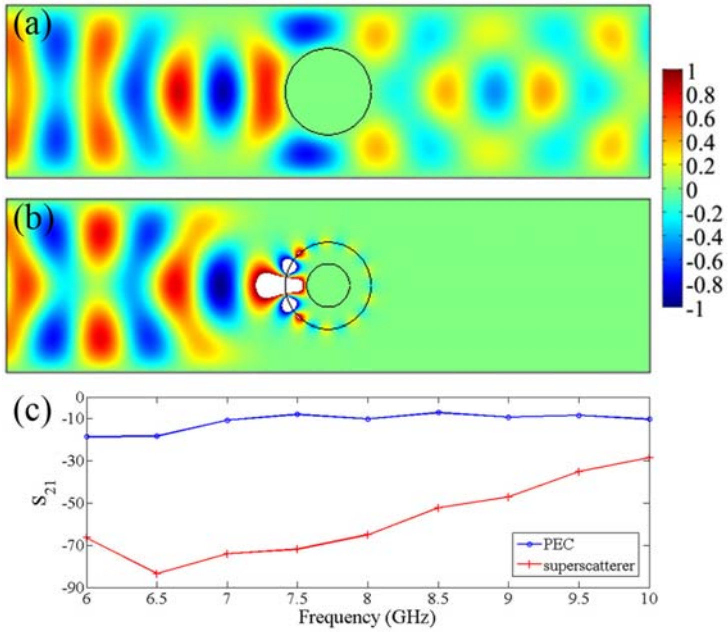

Fig. 3.4. The transmission of the electromagnetic waves through a waveguide partially blocked by a bare rod of radius $r=b$ and by a PEC rod of radius $r=a$ coated with the isotropic shell ($a<r<b$). The width of the waveguide is 0.08 m, the simulation frequency is 8 GHz, and the incident wave is TE polarized. (a) a snapshot of the magnetic field for a cylindrical bare PEC (r=b=0.02 m) in the waveguide, (b) a snapshot of the magnetic field for a cylindrical bare PEC (r=a=0.01 m) coated with an isotropic magnifying shell (outer radius b=0.02 m, refractive index $n=-b^2/r^2$), (c) transmission spectra for cases (a) and (b).

3.3 Three Dimensional Superscattere Design

The proposed reverse design method for the two dimensional superscatterer can be applied to the three dimensional case, as well. Suppose region Γ_a in Fig. 3.5(a) is occupied by a PEC and is required to scatter the incident light in the same way as a bigger bare PEC structure represented by Γ_c does. In order to achieve this goal, region Γ_a should be covered by another region Γ_b. This shrinkage of one domain into another one can be described in an orthogonal coordinate system via an unknown transformation function $x_i'=U(x_i)$ for $i=1,2,3$. According to the theory of transformation of optics, the constitutive parameters in region Γ_b can be expressed as [60],

$$\varepsilon_{\Gamma_b} = \mu_{\Gamma_b} = diag\left\{\xi_1, \xi_2, \xi_3\right\} = diag\left\{\lambda_1 / \lambda_2\lambda_3, \lambda_2 / \lambda_1\lambda_3, \lambda_3 / \lambda_1\lambda_2\right\}. \tag{3.9}$$

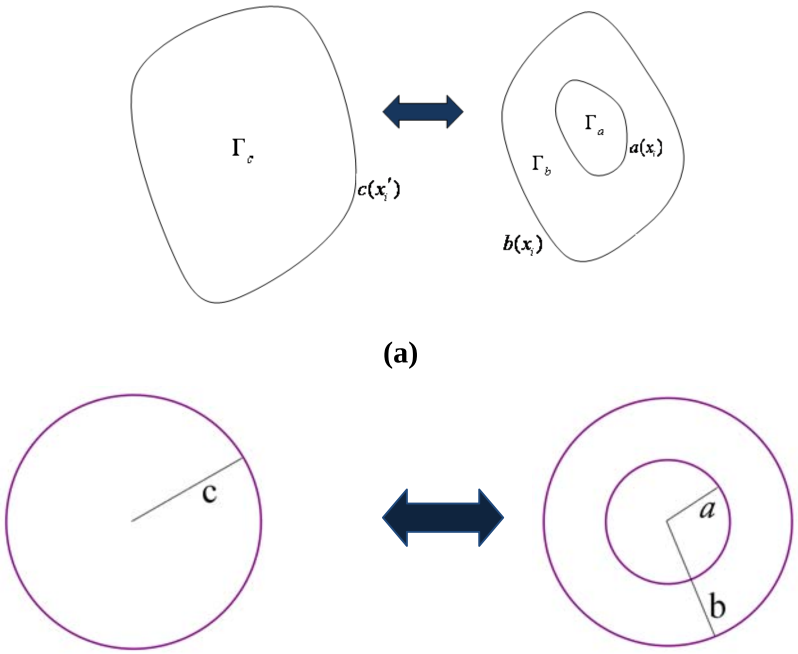

(a)

(b)

Fig. 3.5. (a) Shrinkage of Γ_c space into $\Gamma_a + \Gamma_b$. a , b and c are boundaries; (b) Transforming a circular region $r' \le c$ into an annular region $r \le b$.

If we let one of the ξ_i equal to an arbitrary but analytically integrable function $g\left(x_1, x_2, x_3\right)$ in the region Γ_b, two algebraic equations are obtained for the other two ξ_i. Solving these two equations with boundary conditions $c = U\left(a\right)$ and $b = U\left(b\right)$, the desired parameters can be found. As said before, the interesting point about this kind of design is that it leads to unlimited number of profiles which can do the job. It can also be interpreted through the above formulation, there is no theoretical limit on the size of regions Γ_a, Γ_b and Γ_c which can be arbitrarily small or big, though their profiles might be mathematically complicated.

After the general formulation, we take the design of spherical superscatterer into consideration. Similar to the 2D case as shown in Fig. 3.5(b), a spherical region ($r \le a$) covered by a metamaterial shell ($a \le r \le b$) in physical space $\Omega(r)$, can be transformed from a spherical region ($r' \le c$) in virtual space $\Omega'(r')$ via an unknown transformation function. The medium in the magnifying shell ($a \le r \le b$) has the following relative permittivity and permeability

$$\varepsilon = \mu = diag\left\{\xi_r, \xi_t, \xi_t\right\} = diag\left\{\lambda_r / \lambda_t^2, 1/\lambda_r, 1/\lambda_r\right\} , \tag{3.10}$$

where $\lambda_r = dr/dr'$ and $\lambda_t = r/r'$. Since our shrinkage in the spherical coordinate system is in the radial direction, the transformation function is dependent only on r, i.e. $r' = U(r)$. Now, let us choose $\xi_t(r) = A_0 g(r)$, where $g(r)$ can be any arbitrary well defined function and A_0 is a constant. So we have

$$\xi_t(r) = \frac{dr'}{dr} = A_0 g(r)\cdot \tag{3.11}$$

Then if we solve for r', we get

$$r' = U(r) = A_1 + A_0 \int_a^r g(\tau)\,d\tau. \tag{3.12}$$

Satisfying the boundary conditions $r'|_{r=a} = U(a) = c$ and $r'|_{r=b} = U(b) = b$, leads respectively to $A_1 = c$ and

$$A_0 = \frac{b-c}{\int_a^b g(\tau)\,d\tau}\cdot \tag{3.13}$$

From equation (3.10), we also know that

$$\xi_r(r)\xi_t(r)=\left(\frac{r'}{r}\right)^2. \tag{3.14}$$

Hence from equations (3.11) and (3.13), we obtain

$$\xi_r(r)=\left(\frac{r'}{r}\right)^2\frac{1}{A_0 g(r)}=\left(c+\frac{b-c}{\int_a^b g(\tau)d\tau}\int_a^r g(\tau)d\tau\right)^2\frac{\int_a^b g(\tau)d\tau}{(b-c)r^2 g(r)}. \tag{3.15}$$

Now, choosing $g(r)=r^n$ as an example, we find the corresponding transformation function, $\xi_t(r)$ and $\xi_r(r)$ of the proposed spherical magnifier,

$$r'=U(r)=\frac{c\left(b^{n+1}-r^{n+1}\right)+b\left(r^{n+1}-a^{n+1}\right)}{b^{n+1}-a^{n+1}}, \tag{3.16}$$

$$\xi_t(r)=-\frac{(n+1)(c-b)r^n}{b^{n+1}-a^{n+1}}, \tag{3.17}$$

$$\xi_r(r)=-\frac{\left(c\left(b^{n+1}-r^{n+1}\right)+b\left(r^{n+1}-a^{n+1}\right)\right)^2}{(n+1)(c-b)\left(b^{n+1}-a^{n+1}\right)r^{n+2}}. \tag{3.18}$$

Shown in Fig. 3.6(a) are the traces of rays impinging upon the PEC small sphere of radius $a=0.1$ m coated with the complementary medium $a\le r\le b=2a$, while the paths of the rays scattered by a single PEC sphere of radius $c=b^2/a$ are represented in Fig. 3.6(b). Comparing Fig. 3.6(a) with Fig. 3.6(b) reveals that the scattered rays from the coated small sphere follow the same traces as the rays scattered from the bigger PEC sphere. Therefore, it is interpreted that the scattering cross section of the small composite sphere is equal to that of the big PEC one. As mentioned earlier, there is no theoretical limit on a and c, which means that they can be as small or big as possible, though the coating medium profile might be mathematically complicated. Note that since our structure is spherically symmetric, the corresponding

Hamiltonian of the TE and TM modes do not have any terms in common and therefore the designed structure can work for these two polarizations.

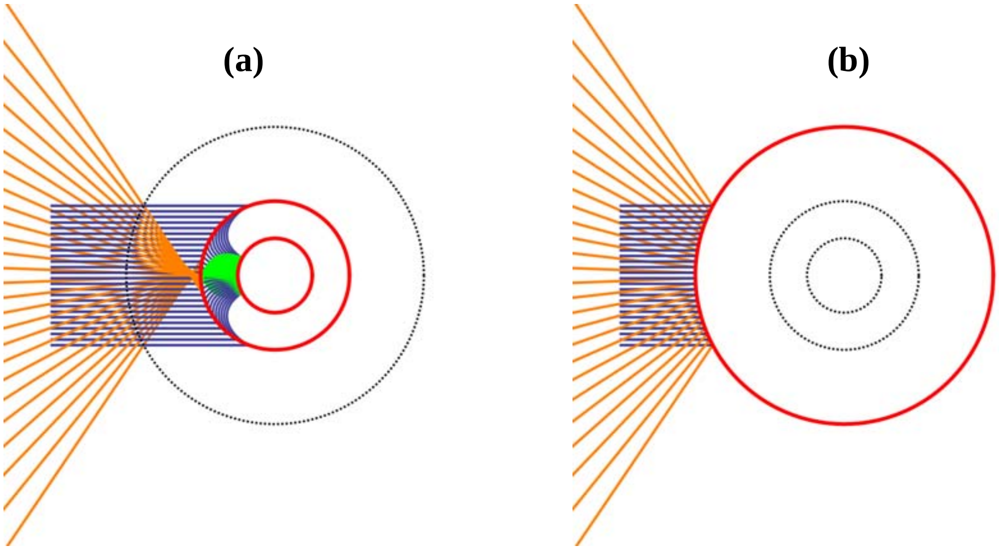

Fig. 3.6. (a) Ray traces for a PEC sphere of radius *a* enclosed in a complementary medium with thickness of *b*-*a* (solid red lines), (b) ray traces for a bare PEC sphere of radius *c* (the solid red line). The blue and orange lines denote incident and scattered rays, respectively.

A photorealistic demonstration of the designed spherical magnifier is presented in Fig. 3.7. As can be seen in this figure, a small spherical mirror of radius $a = 0.1\,\text{m}$ with an annular coating of the outer boundary radius $b = 2a$ is compared with a non-coated single spherical mirror of radius $b = 2a$ in a photorealistic manner. Both the spheres are actually placed in front of infinitesimally small virtual camera, which is circumscribed by a background scene of a garden pictured panoramically in Fig. 3.7(a). The distance between the camera and the center of the mirror in both Figs. 3.7(b) and (c) is assumed to be 1 m. As it is noticed from the comparison between Figs. 3.7(b) and (c), the non-coated mirror reflects a much wider and more compressed area of the reverse scene than the coated mirror, which magnifies the reverse scene and more details of this scene can be observed. In other words, the coated mirror acts like a bigger but non-coated mirror, demonstrating the magnification of the scattering. This illustration indeed verifies the fact that the scattering cross section of the coated mirror is much larger than that of the non-coated one.

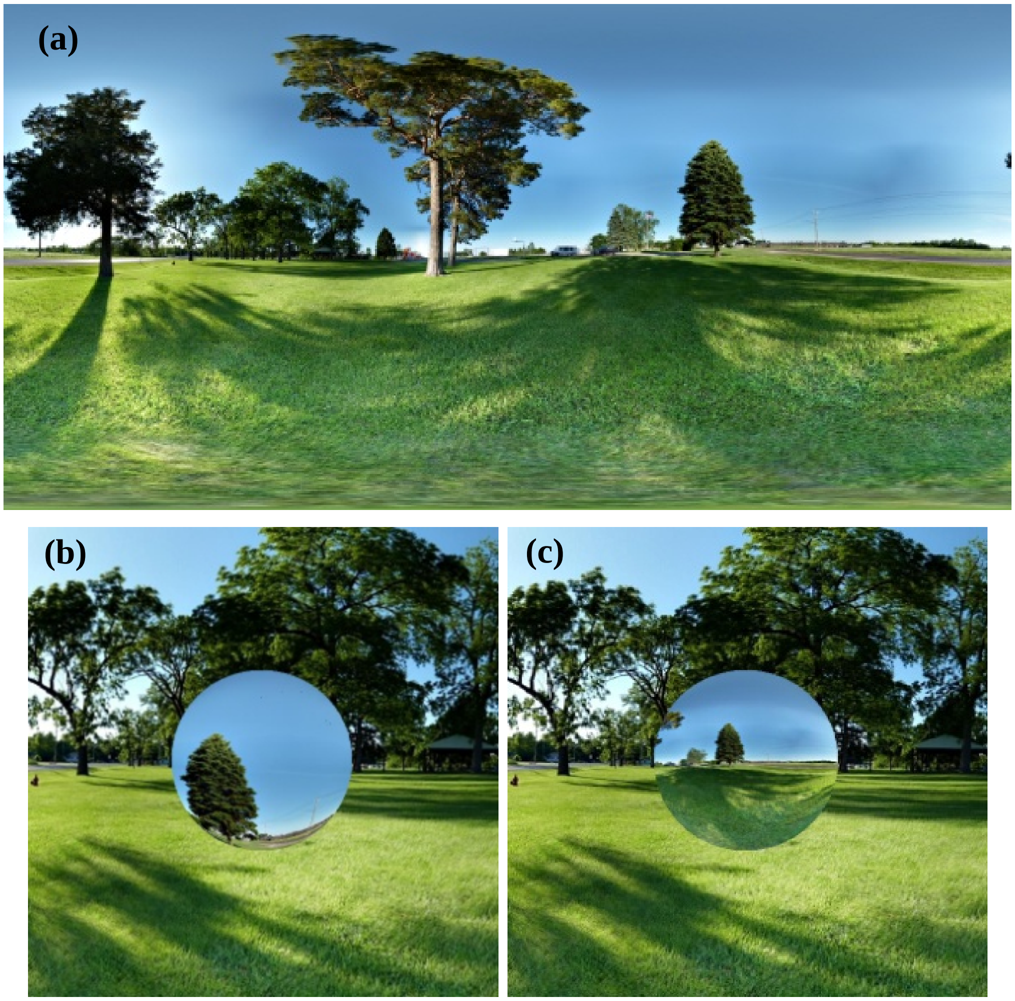

Fig. 3.7. (a) Panoramic depiction of the background scene, (b) a snapshot of the coated mirror, (c) a snapshot of the non-coated mirror. The physical sizes of (a) and (b) are the same. The camera is assumed to be 2 m away from the background scene so as to achieve a balance between close and far parallax error.

3.4 Conclusions

In this chapter, we developed a reverse methodology to realize metamaterial magnifiers in both the cylindrical and spherical geometries. They can be designed and visualized by use of negative index metamaterials without knowing the required spatial deformation a priori. The numerical results confirm the validity of the proposed concept, and also they show the significance of choosing a proper generating function so as to control the field distribution pattern in the complementary medium. The photorealistic rendering of an interesting magnifying superscatterer has distinguished features against a conventional Eaton lens in terms of ray trajectories and image properties. This reverse transformation further allows us to efficiently optimize and simplify magnifier's parameters by considering various generating functions rather than considering one specific set of parameters calculated from a given coordinate transformation each time. Nevertheless, besides the pros and cons of the developed reverse method of superscatterer design, the content of this chapter is a bright example of a standard ray tracing process and a sensible demonstration of photorealistic rendering in a practical situation. However, in the next chapter a more counterintuitive case of ray tracing applicability in graded complex device design will be studied, and it will be shown that a combination of inhomogeneity and anisotropy can lead to overlapping optical functionalities in a single device. What will come in the next chapter is an elaborate exploitation of the optical Hamiltonian and transformation optics in a graded-index anisotropic medium to solve a challenging problem.

CHAPTER 4

Biaxial Devices with Multiple Functions

4.1 Introduction

It is remarkable in modern optics that there is still no general method of designing a gradient index device when presented with a desired optical behavior and the correct form of the Hamiltonian, even in the isotropic case. However, much can be learned from the case of spherical symmetry, where general design methods do exist, both for isotropic and uniaxial cases [21, 61]. Spherically symmetric lenses are also of wide interest because of their unique ability to work equally well in all directions, and it stands to reason that there exist a number of spherically symmetric lenses that are "named" because of their great utility, viz. Maxwell's fisheye [62], the Eaton lens, the Luneburg lens [55], the invisible sphere [21, 61], the Pendry cloak [5], and the Miñano lens [63], to name just a few. Spherical symmetry is also important because ray Hamiltonians have the same form in all orthonormal coordinate systems [20, 33], so results in Hamiltonian optics in this system can often be generalized to other coordinate systems. In this work, we explore the design of gradient-permittivity biaxial dielectrics in this special system, which is much more complicated than it may first seem: although the permittivity tensor contains only three diagonal elements, as seen in Chapter 2, they are not separable in the Hamiltonians that determine the ray trajectories—light traveling through a biaxial device will generally be affected by all three gradient index tensors, resulting in long and complicated Hamiltonians. This occurs because light polarization can be continuously rotated in such a device. Though complex, biaxial optical instruments represent a potentially important way to achieve certain kinds of functionality in optics that would otherwise be impossible. In this work, for example, it will be shown that one can take any four independently-chosen spherically-symmetric lenses and combine their optical functions in an overlapping spherical region of space with a *single biaxial lens*, with each function assigned to a specific polarization and set of planes. We define "*optical function*" here to include the behavior of *any possible* lens or optical instrument that can be designed with an isotropic permittivity. (Note that this is extremely general, since it encompasses anything that can be defined by a spatially-dependent refractive index profile.) Due to the mixing of the tensor elements, it will also be shown that four is the maximum number of *independent* isotropic lens functions that can be combined. If more lens functions were desired in an overlapping region of space, symmetry would be broken.

A successful attempt to combine two optical functions into a single device with uniaxial symmetry was previously shown in [61] and such a device was realized experimentally in [64]. The work of [61] was also general: it combined arbitrary lens functions in overlapping physical space (where light entering an arbitrary point of a lens may interact with the entire body of the lens, for all points on the lens) and it is this generality that made the finding significant. In [61], through a regressive formulation on the basis of transformation optics, a new degree of freedom was induced into a dielectric uniaxial medium to make two polarizations do two different tasks simultaneously, while maintaining spherical symmetry. Lenses could be rotated arbitrarily without altering light trajectories at all. But unfortunately the integration over the physical extent of the device to determine the transformation function in [61] is not always convergent. Even in the converging cases, that method can provide only one transformation function for each pair of functionalities which means that method remains somewhat limited from an experimental point of view.

The design method to be introduced here relaxes that constraint somewhat, and can be readily applied to improve existing designs in metamaterials. For example, devices designed with transformation optics [5, 21, 65] require a nonunity magnetic permeability resulting in either loss or sacrifice of device functionality for one polarization [4, 31, 61, 66, 67], but this polarization can be "recovered" with the biaxial method to take on new optical functions. Biaxial dielectrics could potentially be fabricated by creating composite materials (asymmetric air inclusions in glass, for example) that have practically no loss or dispersion at optical wavelengths. The field of dielectric device design, with no need for metals or chirality, remains rich for exploration.

Another application of the biaxial method is to build upon interesting existing work in the area of "Janus" devices [68], where two-dimensional dielectric devices with two different optical functions in two different directions can be made. The authors of [68] employed transformation optics in two vertical directions independently and by invoking a quasi-conformal mapping technique [65], they achieved a nearly isotropic permittivity profile for their Janus device. However, the designed metadevice, like almost all transformation optics devices, was limited to only one polarization and furthermore is restricted to only a few permissible optical functions. Here, we extend this work to three dimensions and encompass both polarizations.

4.2 Controlling Biaxiality

In this section, we discuss the details of how to control biaxiality in order to engineer the behavior of a biaxial device so that it can acquire different functionalities for each polarization. Due to double refraction at the interface of a biaxial medium, any unpolarized incident ray (wave) splits into two polarized rays (waves) with reference to the alignment of the electric field; the in-plane and out-of-plane polarizations [20]. In Chapter 2, the Hamiltonian in a biaxial medium was factorized into two terms which are individually taking care of either of the incident polarizations along a plane of interest and therefore, by manipulating these two terms, we would be able to control the performance of each polarization. Unfortunately along an arbitrary plane, the factorized expressions become very complicated and it seems to be a hard task to engineer the incident polarizations. However, along principle planes (i.e. one of k_i vanishes) of the biaxial medium, the factorized terms turn out to be simpler. Even along these planes the factorized expressions share some terms and in order to control the performance of the polarizations along the principle planes, we cannot simply play with the permittivity elements ad hoc, as random guessing may not lead to interesting functions for all polarizations. To get around this problem, we make use of transformation optics to basically open some space in the physical domain (the principle planes) for correcting the paths of the rays with the out-of-plane polarizations, while the opened space cannot be seen by the in-plane polarizations. Although we believe this method can work in any orthogonal coordinate geometry, we will now use the spherical coordinate system as a specific example frame to depict the validity of this method.

4.2.1 General Idea

The main goal here is to design a dielectric graded-index sphere with a radially symmetric biaxial permittivity profile. This device is required to show different functions in its equatorial and polar planes. Due to two possible polarizations in each of these planes, the designed lens offers generally four functions in the planes of interest. This is the immediate interpretation, although the prospective biaxial profile of the sphere is radially symmetric and contains only three elements in its permittivity tensor.

In order to obtain the desired profile, it would not be advisable to simply play with permittivity elements in a random or blindly numerical manner. By simply changing the permittivity elements, at most we can design the functions of in-plane polarizations in the main two planes and most likely the behaviors of the out-of-plane polarizations would be out of our hands (essentially they would be sacrificed, just as they generally would be in devices designed with transformation optics but implemented in dielectrics). To find a way out of this problem, we use transformation optics to open some space in the physical domain for correcting the paths of the rays with out-of-plane polarizations, while the opened space cannot be seen by the in-plane polarized rays. Therefore, we can still use transformation optics, but correct the paths of the otherwise sacrificed rays with out-of-plane polarizations.

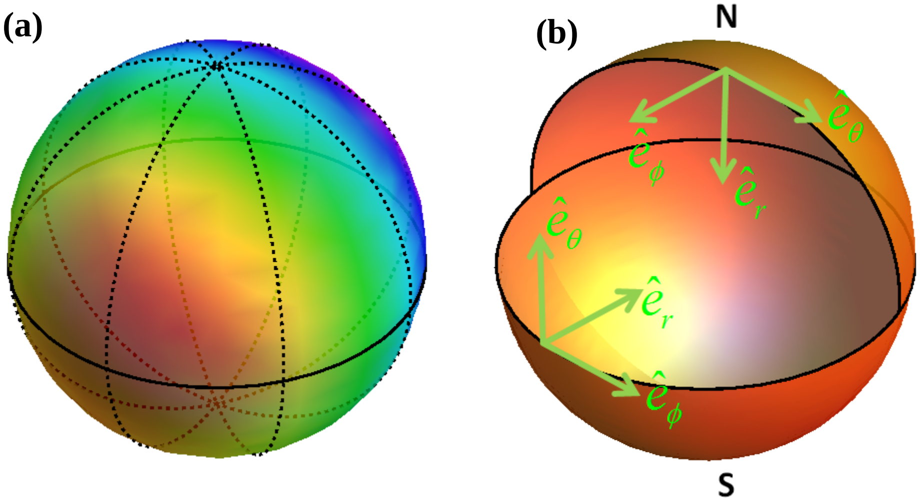

Fig. 4.1. (a) Illustration of equatorial and polar planes in a sphere (the solid circle is the equatorial plane and the dashed circles are polar planes); (b) alignments of basis vectors along equatorial and polar planes.

Before going further, we prefer to mention what we mean by equatorial and polar planes. If we assume north and south poles for a sphere in a coordinate system like $\{\hat{e}_r, \hat{e}_\theta, \hat{e}_\phi\}$, the large circular plane which divides the sphere into northern and southern hemispheres is called the equatorial plane. All the longitudinal great circles which are perpendicular to the equatorial circle and crossing both poles are called polar planes. These two types of planes are shown in Fig. 4.1(a). It should be noted that in any sphere, we have a unique equatorial plane and an infinite number of polar planes and our designed device is supposed to represent two specific functions along the equatorial plane and two other functions along all the polar planes. According to Fig. 4.1(b), the normal vector to the equatorial plane at the boundary of the sphere is in the direction of $\hat{e}_\theta$, while along each of the polar planes the normal vector is parallel to $\hat{e}_{\phi}$. If we break the incident fields into in-plane and out-of-plane polarizations, then despite its general complicated form, the Hamiltonian of a dielectric biaxial medium with the permittivity tensor $\varepsilon = diag\left\{\varepsilon_r = n_r^2, \varepsilon_\theta = n_\theta^2, \varepsilon_\phi = n_\phi^2\right\}$ in a spherical geometry along the equatorial and polar planes can be simplified as

$$\mathcal{H}_{equatorial} = \left(k_r^2 + k_\phi^2 - n_\theta^2\right)\left(k_\phi^2 n_\phi^2 + \left(k_r^2 - n_\phi^2\right)n_r^2\right), \tag{4.1}$$

$$\mathcal{H}_{polar} = \left(k_r^2 + k_\theta^2 - n_\phi^2\right)\left(k_\theta^2 n_\theta^2 + \left(k_r^2 - n_\theta^2\right)n_r^2\right), \tag{4.2}$$

where $\vec{k} = \hat{e}_r k_r + \hat{e}_\theta k_\theta + \hat{e}_\phi k_\phi$ is the wave vector in the spherical coordinate system. It should be noted that we assume the designed spherical lens is radially symmetric, i.e. $n_i = n_i\left(r\right)$ for $i = r, \theta, \phi$, and also has a radius equal to one. Nonetheless the radius of the lens can have any value and we are able to rescale all the diagrams and equations represented in this paper. As noted earlier, we cannot trivially assign functions to the permittivity components, for according to equations (4.1) and (4.2) they are playing a coupled role in formation of the Hamiltonians governing each ray. In order to achieve the proposed device through this method, we have to overcome several restrictions as will be explained in the subsequent sections.

4.2.2 Design for the In-plane Polarization

It is well-known that with the use of transformation optics, one can open space inside a medium to cloak an object [5, 21]. Here, we can open a hole with radius a at the center of our device to have some space to correct the ray trajectories for the out-of-plane polarizations. Now suppose for the in-plane polarizations, we would like the spherical device to offer function “A” for equatorial rays and function “B” for polar rays. And also suppose that these two functions can be individually implemented via isotropic and radially symmetric index profiles. Let us take the isotropic profiles of functions A and B as $n_e(r)$ and $n_p(r)$, respectively, where these two profiles are impedance matched with the vacuum at the boundary, i.e. $n_e(r=1)=n_p(r=1)=1$. Then we consider $n_e(r)$ and $n_p(r)$ as virtual indices and we apply transformation optics to them. If we employ transformation functions $r_{r\phi}=r_{r\phi}(R)$ and $r_{r\theta}=r_{r\theta}(R)$, where $0\le r_{r\phi}\le 1$ and $0\le r_{r\theta}\le 1$ refer to the virtual space along equatorial and polar planes and $a\le R\le 1$ denotes the physical space, then after performing some sort of normalization similar to that shown in [61], we obtain the following equations for the transformed permittivity components,

$$\varepsilon = diag\left\{ n_r^2 = n_e^2\left(\frac{r_{r\phi}}{R}\right)^2 = n_p^2\left(\frac{r_{r\theta}}{R}\right)^2,\ n_\theta^2 = n_p^2\left(\frac{dr_{r\theta}}{dR}\right)^2,\ n_\phi^2 = n_e^2\left(\frac{dr_{r\phi}}{dR}\right)^2 \right\}, \quad (4.3)$$

where n_e and n_p should be expressed in terms of R, i.e. $n_e = n_e\left(r_{r\phi}(R)\right)$ and $n_p = n_p\left(r_{r\theta}(R)\right)$. Additionally, according to the basic theory of transformation optics, we should have $r_{r\phi}(R)\big|_{R=1} = r_{r\theta}(R)\big|_{R=1} = 1$ and $\left(dr_{r\phi}/dR\right)\big|_{R=1} = \left(dr_{r\theta}/dR\right)\big|_{R=1} = 1$. We also let $\mu = \{1,1,1\}$ in the physical space.

It is important to note that in equation (4.3) we have used the transformation $r_{r\phi}(R)$ in the equatorial plane and $r_{r\theta}(R)$ in the polar plane of the virtual medium to find $n_\phi(R)$ and $n_\theta(R)$, respectively. However, through this trick we would normally obtain two expressions for $n_r(R)$, which is physically impossible. Thus we have to choose proper expressions for $r_{r\phi}(R)$ and $r_{r\theta}(R)$ so that the two expressions for $n_r(R)$ become equal to one another. Or simply from the first equality in equation (4.3), we should have

$$n_e r_{r\phi} = n_p r_{r\theta}. \tag{4.4}$$

If we take derivatives from both sides of equation (4.4), we obtain

$$n_e \frac{dr_{r\phi}}{dR} + \frac{dn_e}{dr_{r\phi}} \frac{dr_{r\phi}}{dR} = n_p \frac{dr_{r\theta}}{dR} + \frac{dn_p}{dr_{r\theta}} \frac{dr_{r\theta}}{dR}. \tag{4.5}$$

At the boundary of the lens $R = 1$, we have then

$$\frac{dn_e(r)}{dr}\Big|_{r=1} = \frac{dn_p(r)}{dr}\Big|_{r=1}, \tag{4.6}$$

where we have omitted the subscripts. Equation (4.6) actually inserts a restriction on the choice of n_e and n_p. Not any pair of well-known profiles like the Eaton lens, Maxwell fish-eye, and invisible sphere, etc. [21] may satisfy this condition. Here in order to overcome this obstacle, we break each of $n_e(r)$ and $n_p(r)$ profiles into inner and outer layers,

$$n_i(r) = \begin{cases} n_{i1}(r) & r_1 \le r \le 1 \\ n_{i2}(r) & 0 \le r \le r_1 \end{cases} \quad (i = e, p), \tag{4.7}$$

where we can assign any value between 0 and 1 to r_1. However, for ease in later calculations, we prefer r_1 to be bigger than a, i.e. $0 < a < r_1 < 1$. Then we have to design the respective profiles of these two layers so that they become continuous at $r = r_1$ and also all the incoming rays spiral into the inner layer as shown in Fig. 4.2.

In order to make all the rays spiral into the inner layer, we just need to assign a function, which is equal to one at $r=1$ and bigger than $1/r$ in the range $r_1 \le r \le 1$ [61]. However, the assigned function should be the same for n_e and n_p as we want to satisfy (4.6). As a consequence, an infinite number of functions can do the job for $n_{i1}(r)$. One among these functions is

$$n_{i1}(r) = \frac{3}{4r^{4/3}} + \frac{1}{4}. \tag{4.8}$$

This specific function is shown in Fig. 4.3. It is seen that this function is equal to one at $r=1$ and also bigger than $1/r$ in the range $0 \le r < 1$ without considering what the value of r_1 might be.

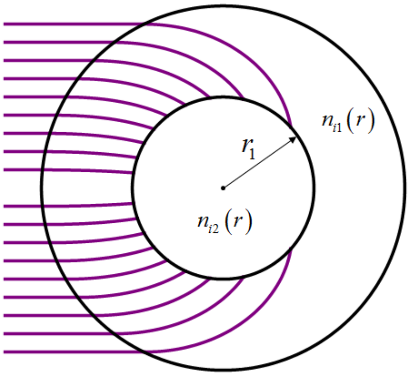

Fig. 4.2. The two layered profiles of $n_e(r)$ and $n_p(r)$. As can be seen, all the incoming rays should spiral into the inner layer.

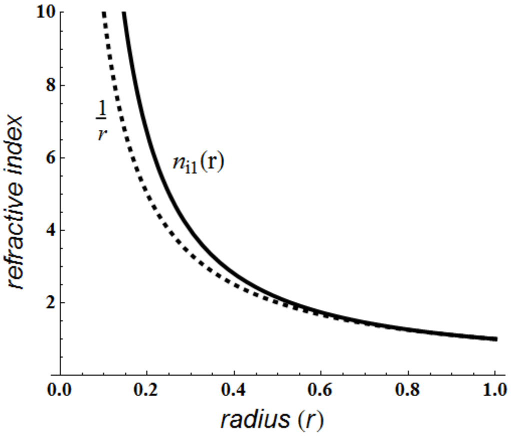

Fig. 4.3. Diagrams of $n_{i1}(r)$ and $1/r$.

In order to design the index profile within the inner layer, we follow the implicit integration explained in [21, 69]. We identify the impact parameter b of every spiraling ray at the boundary of the inner layer. According to the formation of ray trajectories corresponding to functions A or B, we would be able to determine the turning angle $\chi(b)$ toward the origin as a function of the impact parameter. Then we can calculate the profile index inside the inner region by solving the following integral equation for $n_{i2}(r)$,

$$\ln\left(\frac{n_{i2}}{n_{outer}}\right)=\frac{1}{\pi}\int_{r_1\rho}^{r_1}\frac{\chi(b)\,db}{r_1\sqrt{b^2/r_1^2-\rho^2}}, \tag{4.9}$$

where $\rho = rn_{i2}/Bn_{outer}$ and $n_{outer}=n_{i1}(r)\big|_{r=r_1}$.

Then with the use of transformation optics, we open a hole at the center of the device which is not seen by the in-plane polarized rays along both the equatorial and polar planes. But this opened hole is sensed by the out-of-plane polarized rays. So we can use this space effectively to engineer the trajectories of rays with the out-of-plane polarizations without disturbing the performance of the in-plane polarized rays. To do so, we should let all the out-of-plane polarized rays enter the central opened hole. As interpreted from equation (4.1) and (4.2), out-of-plane polarized rays in the equatorial plane (polar planes) act as if they were in an isotropic medium with a refractive index of n_θ (n_ϕ). In order to make the out-of-plane polarized rays spiral into the central space, similar to before we should have

$$n_\phi(R),n_\theta(R)>\frac{1}{R}\qquad for\, a<R<1. \tag{4.10}$$

As said earlier, we prefer to apply the transformation function over the inner layers of the virtual space (i.e. a to be smaller than r_1), so that the transformation functions will not affect the outer layers and hence the physical and virtual spaces overlap in the range $r_1 \le R \le 1$. Consequently, the inequality in equation (4.10) should be slightly modified as

$$n_\phi(R), n_\theta(R) > \frac{1}{R} \qquad \mathit{for}\, a < R < r_1 . \tag{4.11}$$

In addition, we also remember that in order to have a single expression for $n_r(R)$ at the end, equation (4.4) should be fulfilled. Therefore, enough care should be taken to choose appropriate transformation functions, $r_{r\phi}$ and $r_{r\theta}$, such that both equations (4.4) and (4.11) would be satisfied. The transformation functions should basically have the following properties,

$$\begin{cases} r_{r\phi}\big|_{R=a} = r_{r\theta}\big|_{R=a} = 0 \\ r_{r\phi}\big|_{R=r_1} = r_{r\theta}\big|_{R=r_1} = r_1 \\ \left(dr_{r\phi}/dR\right)\big|_{R=r_1} = \left(dr_{r\phi}/dR\right)\big|_{R=r_1} = 1 \end{cases} . \tag{4.12}$$

4.2.3 Design for the Out-of-plane Polarization

Referring to the Hamiltonian of the biaxial medium, the out-of-plane polarized rays in equatorial and polar planes behave as if they were in isotropic media with refractive indices n_θ and n_ϕ, respectively. In this part of the design we require both $n_\phi(R)$ and $n_\theta(R)$ to have values bigger than $1/R$ over all the range $a \le R < r_1$. Additionally, we know that in the range $r_1 \le R \le 1$ along both of the two planes $n_\phi(R)$ and $n_\theta(R)$ are equal to $n_{i1}(R)$, for the virtual and physical spaces are the same there. Hence, all the rays with the out-of-plane polarizations along these two planes spiral into the region

$R \le a$. Since this region is invisible to the in-plane polarized rays, we can use it to independently engineer the out-of-plane polarized ray trajectories. To do so, we resort to the integral equation (4.9) again. But for this time, we have in the equatorial plane $n_{outer} = n_\theta(R)\big|_{R=a}$ and in the polar planes $n_{outer} = n_\phi(R)\big|_{R=a}$. Then considering two other arbitrary functions like "C" and "D" for the out-of-plane rays along equatorial and polar planes, we can calculate the turning angles $\chi(b)$ and solve the related integral equations for $n_\theta(R)$ and $n_\phi(R)$ in the region $R \le a$.

4.2.4 A Specific Example

Now let us assume that function A (corresponding to n_e) to be a 90 degree deflector of rays and function B (corresponding to n_p) to be a 180 degree deflector of rays (equivalent to the performance of an Eaton lens). Let us note at this point that these lenses have singularities in their index profiles in the isotropic case, but these singularities are unrelated to the discussion that follows. (They are simply a feature of the lens index profile, and other lenses could also have been chosen instead. We choose them as convenient examples only since their optical functions are simple to understand.) For these two specific functions, we have calculated the refractive index distributions in the inner layers and the respective graphs for $n_{e2}(r)$ and $n_{p2}(r)$ are given in Fig. 4.4, where we have taken $r_1 = 0.85$.

As said before, both $n_e(r)$ and $n_p(r)$ have two parts which are continuous at the boundary of inner and outer layers. The inner parts are

$n_{e2}(r)$ and $n_{p2}(r)$, which are touching each other at $r = r_1$. The outer parts are set equal to $n_{i1}(r)$, which is bigger than $1/r$ to make the rays spiral from the outer layers into the inner layers. At $r = 1$, we have $n_e = n_p = 1$ and $dn_e/dr = dn_p/dr$, which shows that the restriction of (4.6) is satisfied. The ray trajectories for these refractive index distributions are depicted in Fig. 4.5.

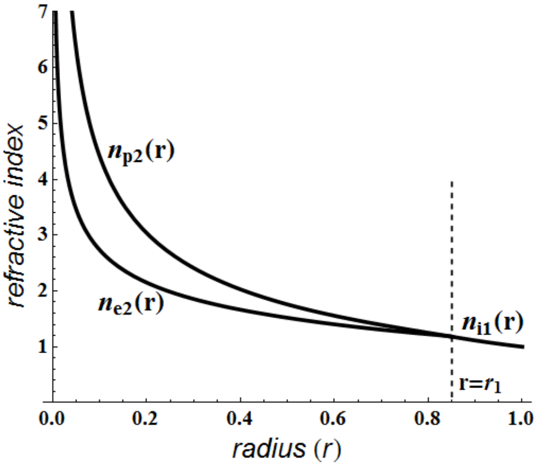

Fig. 4.4. Refractive index distribution for functions in the outer and inner regions of the lens along equatorial (Function A) and polar planes (Function B) in the virtual medium.

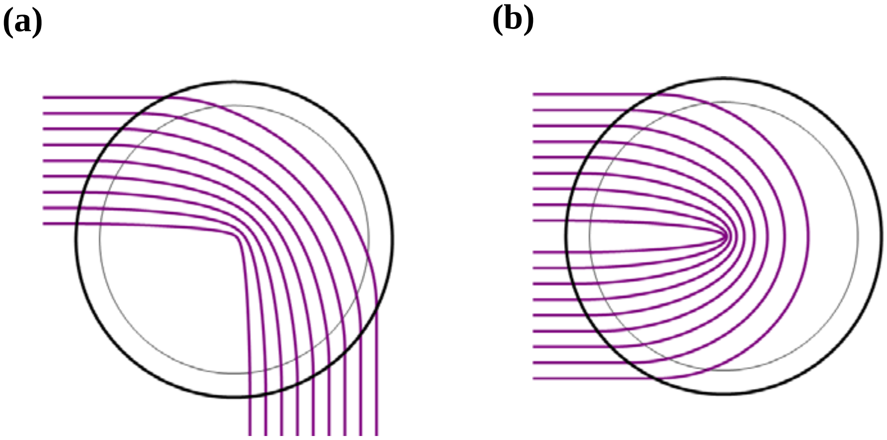

Fig. 4.5. Ray trajectories in virtual space; (a) 90 degree bending (function A) along the equatorial plane corresponding to $n_e(r)$, (b) 180 degree bending (function B) along polar planes corresponding to $n_p(r)$.

So far we have found two proper index profiles, which are satisfying equation (4.6), along equatorial and polar planes in the virtual space. Now we are prepared to apply convenient transformation functions on these two profiles to obtain the permittivity elements according to equation (4.3) in the physical space. Writing the transformation functions $r_{r\phi}\left(R\right)$ and $r_{r\theta}\left(R\right)$ in a linear or nonlinear series of some basic mathematical functions and finding the corresponding coefficients with simple but tedious numerical techniques, we would be able to approach the proper transformation functions which can do the job. The transformation functions, which we have found for the case $a = 0.34$, are shown in Fig. 4.6. It is seen that the obtained transformation functions are satisfying all the conditions described in equation (4.12). Without loss of generality, we added one more restriction on the transformation functions when we were calculating them and the reason will be clear soon. In fact we let first few derivatives of both transformation functions at $r = a$ be zero. In calculating the transformation functions we actually searched for mathematically well-defined (continuous and integrable) functions which fulfill equation (4.4) firstly. Secondly we looked at the resulting profiles for $n_{\phi}\left(R\right)$ and $n_{\theta}\left(R\right)$ to see how well they satisfy the inequality expressed in (4.11). The profile indices (or equivalently the permittivity tensor elements) $n_{r}\left(R\right)$, $n_{\theta}\left(R\right)$ and $n_{\phi}\left(R\right)$ according to the calculated transformation functions are depicted in Figs. 4.7(a) and (b). The performance of the designed profiles for the in-plane polarizations along equatorial and polar planes are also provided in Figs. 4.7(c) and (d), respectively.

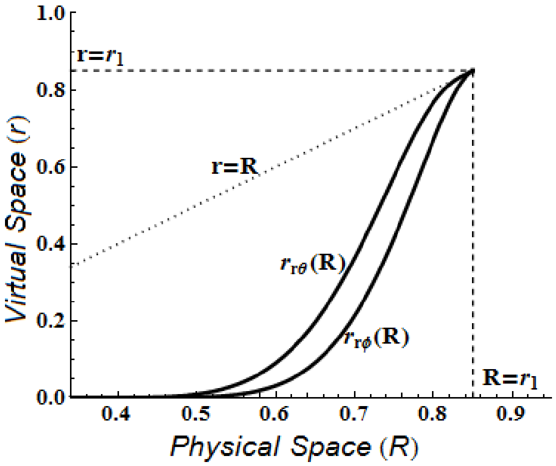

Fig. 4.6. The proper transformation functions which are obtained through a basic numerical manipulation for $a = 0.34$ and $r_1 = 0.85$. The dotted line $r = R$ shows that the transformation functions are eventually tangent to this line.

According to Fig. 4.7, the in-plane polarized rays in the polar planes bend 180 degrees around a central cloaked space and exit in a reverse direction with respect to the incoming rays. The trajectories of rays with an in-plane polarization in the equatorial plane are turning by 90 degrees around the same circumscribed space.

It is shown in Fig. 4.7(a) that with the help of the transformation functions depicted in Fig. 4.6, we can find a unique profile for $n_r(R)$. Through Fig. 4.7(b), it is seen that both $n_\phi(R)$ and $n_\theta(R)$ are zero at $R = a$, which is expected due to the vanishing first few derivatives of the transformation functions. Moreover, according to Fig. 4.7(b) these two profiles are not bigger than $1/R$ (highlighted with the dot-dashed line) in the range $a \le R < a'$, where $a' = 0.51$. Unfortunately this is against what is required in (4.11), although $n_\phi(R)$ and $n_\theta(R)$ are satisfying this requirement over $a' \le R < r_1$. Here is the place to explain why we chose the first few derivatives of the transformation functions to be zero. Due to the quasi-maximally flat nature of the transformation functions around $R = a$ (Fig. 4.6), the radial index $n_r(R)$ has very small values within $a \le R < a'$ range and it causes this region to work like some sort of null space and therefore, as is clear from Figs. 4.7(c) and (d), practically all the rays accumulate somewhere outside this region. So if we expand the size of the inner cloaked space from $R \le a$ to $R \le a'$ (as shown in Fig. 4.7(c) and Fig. 4.7(d) by flashes), we can have $n_\phi(R)$ and $n_\theta(R)$

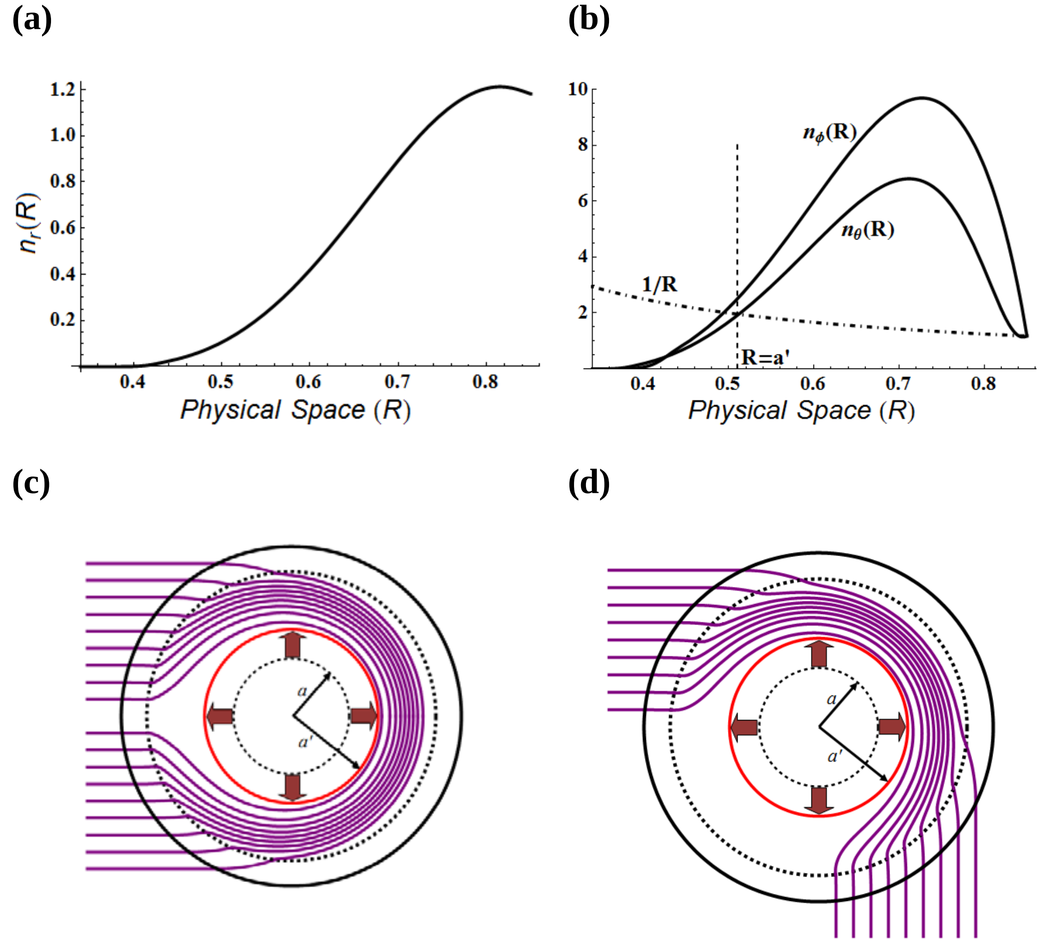

Fig. 4.7. (a,b) Profile indices in the range $a \le R \le r_1$ for the desired biaxial device, (c) The performance of the device for the in-plane polarization along a polar plane, (d) The performance of the device for the in-plane polarization along the equatorial plane.

fulfilling (4.11), as well as not deteriorating the performance of the device for in-plane polarizations. However, the invoked extension may lead to sacrificing rays with extremely low impact parameters, albeit these kinds of rays are usually discarded in graded-index optical devices anyway (and the percentage of affected rays can be designed to be made arbitrarily small).

Having completed the design for in-plane polarized rays, we are now prepared to design the profile indices in the region $0 < R \le a'$ to make our example device work for the out-of-plane polarizations. For this example, we have chosen function C to be a 360 degree deflector of incoming rays, which is similar to the performance of the invisible sphere explained in [21, 61]. We also can assign function D to be a 135 degree deflector of rays. Thanks to our extension of the cloaked area, both $n_{\phi}(R)$ and $n_{\theta}(R)$ have values bigger than $1/R$ all over the range $a' \le R < 1$. In order to find the profile indices in the region $0 < R \le a'$ for the considered functions (C and D), we should use the integral equation (4.9). It should be noted that in computing the profile indices, we should let $n_{outer} = n_{\theta}(R)\big|_{R=a'}$ in the equatorial plane and $n_{outer} = n_{\phi}(R)\big|_{R=a'}$ in the polar planes. The calculated profiles for $n_{\phi}(R)$ and $n_{\theta}(R)$ over the range $0 < R \le a'$ for these two functions are shown in Figs. 4.8(a) and (b), and also the corresponding ray trajectories are shown in Figs. 4.8(c) and (d). It is seen that all the incoming rays funnel into the innermost layer and get deflected by 360 and 135 degrees along equatorial and polar planes, respectively. After designing for the out-of-plane polarizations, in aggregate now we have four different functions along equatorial and polar planes (see Fig. 4.9) and in fact we have a three dimensional four-faced Janus device!

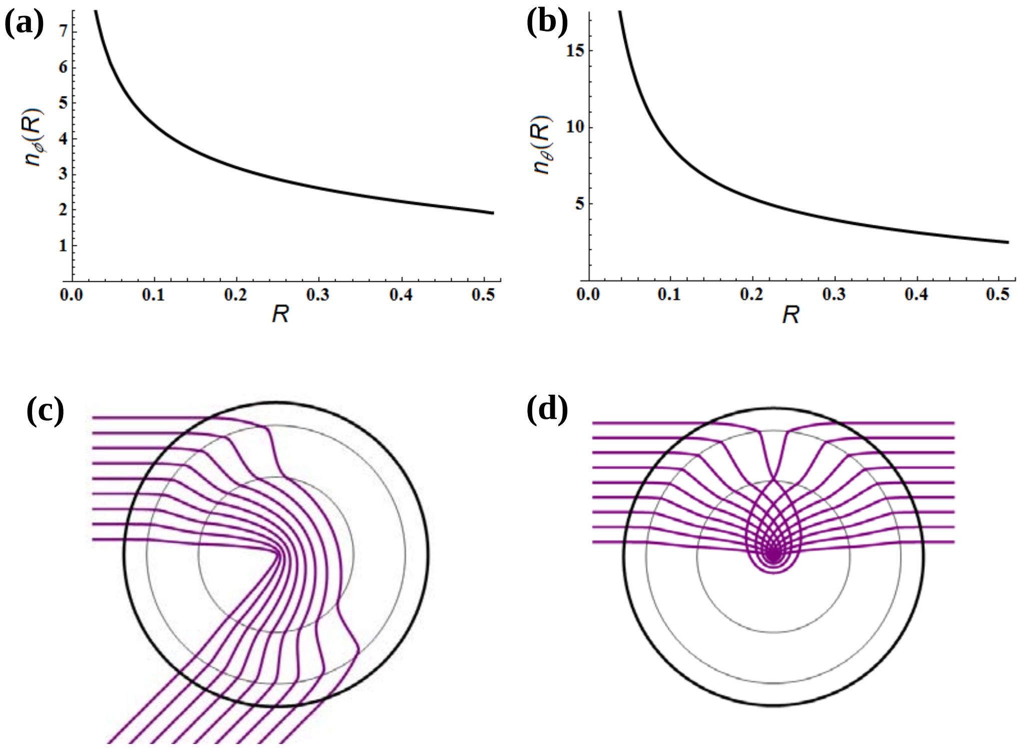

Fig. 4.8. (a,b) The obtained profile indices in the range of $0 < R \le a'$ for the desired biaxial device, (c) The performance of the device for out-of-plane polarized rays along a polar plane, (d) The performance of the device for out-of-plane polarized rays along the equatorial plane.

However, the presented four-faced Janus device is sensitive to polarization. If we would like to obtain a two-faced Janus device for unpolarized light, we just need to equate the in-plane and the out-of-plane polarization functionalities along each of the equatorial and polar planes. Shown in Fig. 4.10(c) is the performance of a Janus device along the equatorial plane, where the incoming rays split into two polarizations, travel along the plane, recombine again and go out with 360 degrees deflection. Through Fig. 4.10(d), it is also seen that along polar planes at $R = r_1$, an unpolarized ray splits into the in-plane and the out-of-plane polarized rays. After traveling along two different paths, these two rays recombine at $R = r_1$

again. It should be noted that as the profiles of the device are radially symmetric, the in-plane and the out-of-plane polarized rays are confined to the equatorial and polar planes and after traveling through the device they merge at $R = r_1$ [21]. The obtained profile indices for this Janus device are given in Fig. 4.10(a) and Fig. 4.10(b).

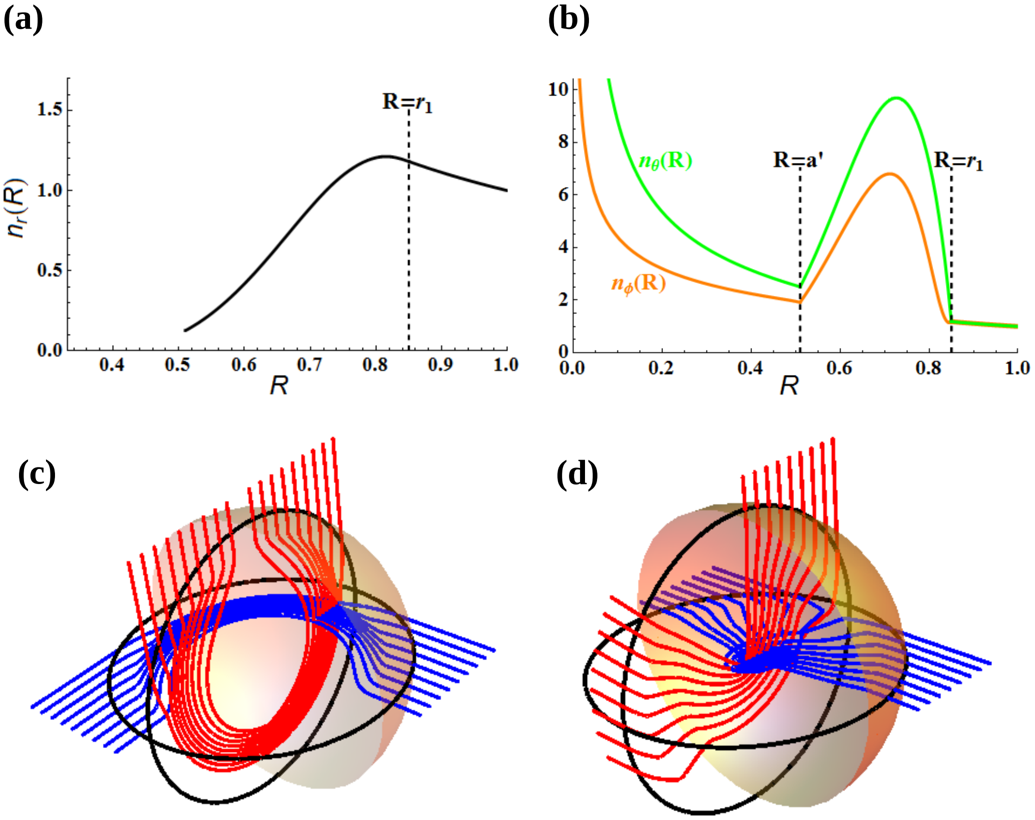

Fig. 4.9. (a,b) Index profiles for n_r , n_θ and n_ϕ. The middle and the inner layer radii are 0.85 and 0.51, respectively. The profile n_r within the inner layer is undefined, as it has no role in the shown functionalities. (c) The performance of the device for the in-plane polarization along polar (red rays) and equatorial (blue rays) planes. (d) The performance of the device for the out-of-plane polarization along polar (red rays) and equatorial (blue rays) planes.

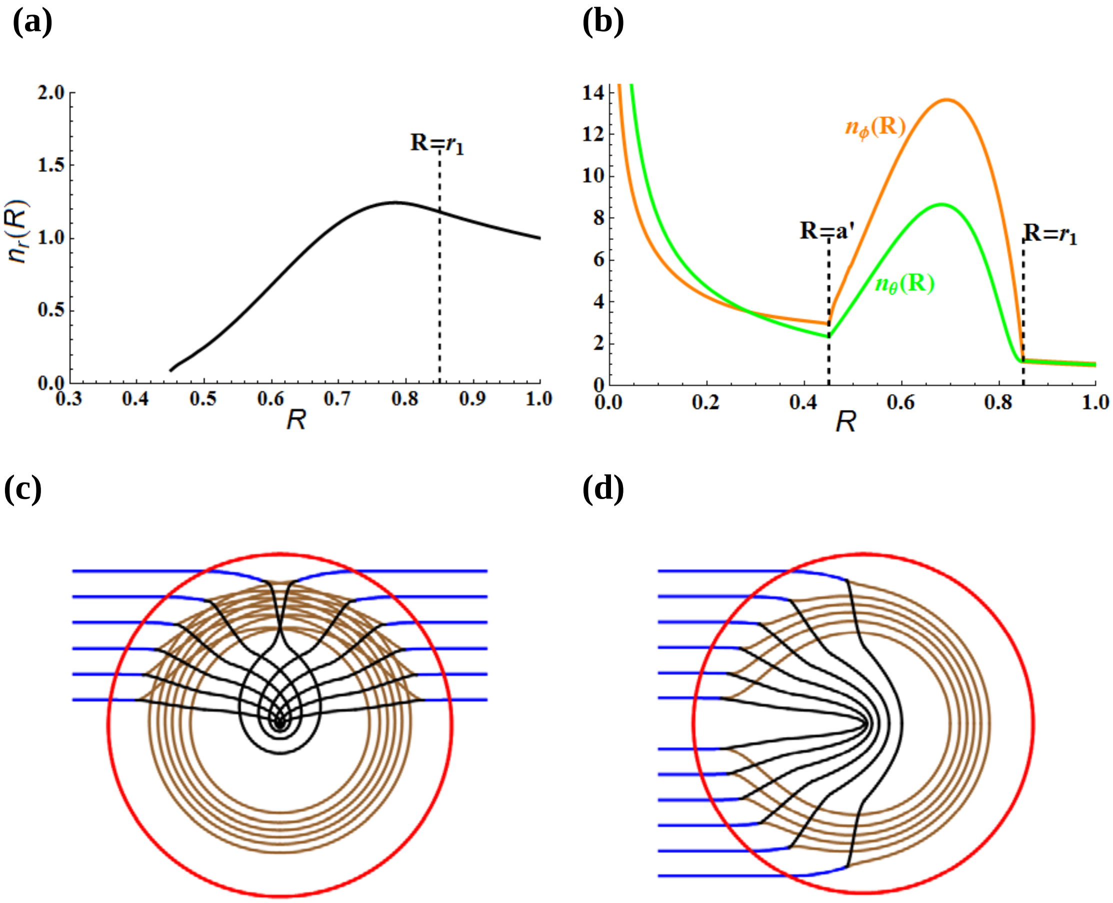

Fig. 4.10. (a,b) The profile indices n_r , n_θ and n_ϕ for the Janus device. In this design, the middle and the inner layer radii are 0.85 and 0.45, respectively. (c) The ray trajectories for in-plane (brown rays) and out-of plane polarizations (black rays) along the equatorial plane. (d) The ray trajectories for in-plane (brown rays) and out-of plane polarizations (black rays) along polar planes.

4.3 Conclusions

In conclusion, on the basis of the factorization of the biaxial Hamiltonian, shown in Chapter 2, and with the use of transformation optics, we proposed a method to design a radially symmetric biaxial dielectric device which offers four different functionalities along equatorial and polar planes. It turns out that for arbitrary functionalities, this is the best that can be done in a biaxial dielectric medium. (We state this without proof, but it can be seen readily – if any other plane were to have a different functionality, it would depend on those already designed because of orthogonality of the coordinate system.) Finally, based on the developed method, we designed a Janus device which represents two different functions for unpolarized light along equatorial and polar planes, respectively. As mentioned previously, the developed method of making use of biaxiality in dielectrics is a complex recipe which incorporates optical Hamiltonian and transformation optics beautifully to shape the formation of optical rays in anisotropic media and to create multi-function optical devices.

As said in Chapter 1, an optical ray is the direction of energy current density (or Poynting vector) in a medium and in the ray tracing machinery we actually calculate or control the direction through which optical energy flows. But one also may ask about the direction of the momentum flow in the medium. As is known from electrodynamics theory, an optical ray carries momentum and therefore a mechanical interaction will take place as the optical ray travels through a medium. As a matter of fact, one should be able to calculate such an interaction in the domain of geometrical optics and to trace the optical force distribution along a ray within a medium. It would be an astonishing complement to the described method in this chapter, if similar techniques can be developed to analyze and to engineer the mechanical interaction of light with optical devices. In Chapter 5, we will comprehensively investigate the optical force calculation from the geometrical optics perspective and briefly sketch the guidelines toward the ultimate goal of bringing optical force in complex media under control.

CHAPTER 5 Force Tracing

5.1 Introduction

Photon wave-particle duality, which states that photons, the quanta of light, exhibit both wave-like and particle-like characteristics, is responsible for almost all the subtleties attached to the behavior of light. Reflection, refraction and interference of light are all a consequence of wave-like behavior to some extent, while black-body radiation, the photoelectric effect and the Compton effect are related to the particle-like nature of photons. Distinguishing these two characteristics is crucial in gaining an intuitive understanding of the physics of light, but sometimes it can be baffling when these two views of the nature of light lead to contradictory conclusions in some circumstances. One such puzzling case is the long-lasting Abraham-Minkowski controversy which is related to the momentum of photons in matter and the distribution of optical force (or stress) and torque within a medium.

From the early days of electromagnetic wave theory, the pressure exerted by light onto a body was of great interest. In 1891, Maxwell, using his celebrated equations, was able to calculate the momentum density of light in free space and predicted that “[concentrated] rays falling on a thin metallic disc, delicately suspended in a vacuum, might perhaps produce an observable mechanical effect” [70]. At the same time, using the second law of thermodynamics, Bartoli reached a similar conclusion [71]. Not long after that, the idea proposed by Maxwell and Bartoli was experimentally validated by Lebedev [72] and later confirmed by experiments carried out by Nichols and Hull [73, 74]. In 1908 Minkowski derived the momentum density of light in dielectrics analytically, reaching a conclusion that a photon inside a medium of refractive index n carries a momentum equal to np, where p is the momentum of the photon in vacuum [75, 76]. Conversely, Abraham formulated electromagnetic momentum conservation in a different way which resulted in a conclusion of p/n for the momentum of the photon within a medium [77, 78]. This was the start of a controversy which lasted for a century; during this long period of time, there have been many efforts made by theoretical [79-91] and experimental [92-94] researchers to advocate either of the proposed formulations or to propose new expressions for the momentum of light in media. The literature concerning this controversy is vast, making it difficult to comprehensively review the various proposed solutions of the past, although we can refer the interested reader to several review papers which seem reasonably comprehensive [95-100]. Finally, it was Barnett who published a paper in 2010 [101] in which he showed how the Abraham-Minkowski puzzle can be settled. We will review his resolution very briefly in the next section, because it is crucial that this be clear before we proceed to calculate force distributions with a ray optics approach.

Leaving the controversy just mentioned aside for a moment, it must be mentioned that there exists a very rich field of research related to optical forces in different structures and devices. Optical tweezers [102], particle trapping by light [103, 104], tractor beams [105-109] and optical lift [110] are examples of very interesting applications of radiation pressure. In most analyses related to light pressure and optical torque, such as in analyses of these applications, researchers typically solve an electrodynamic problem from a full-wave perspective and then use this as a starting point from which they can control mechanical interactions between light and media. Solving a full-wave scattering problem for complex media can be enormously cumbersome and time intensive computation. But because we know that geometrical optics is a strong tool that can be used in many different situations (provided the problem under consideration meets the necessary criteria of the geometrical optics domain), we propose its use to solve the problems of optical force density in graded media. In subsequent sections, we will present a general method to calculate the distribution of the bulk and surface force density within a medium on the basis of ray-tracing techniques; we call this *force-tracing*. This technique is useful for several reasons. Firstly, working with rays is neater and more illustrative than full-wave descriptions. Secondly, in the geometrical optics limit, we need only to solve Hamilton's equations to calculate ray equations and consequently the force felt by each point of the medium under investigation. These equations are much easier to handle than a wave-based field description of the propagating and/or scattered fields which requires constructing the energy-momentum density tensor and integrating it over the domain of interest. Thirdly, similar to what was introduced in references [21, 111], in the geometrical optics domain various tomographic methods can be applied to reconstruct proper electromagnetic profiles to potentially engineer mechanical interactions. As a matter of fact, the force-tracing method could potentially yield a method of forcing an optical force distribution within a medium to be aligned with our interests; in other words, it may lead to a sort of "transformation optics" for forces. Such a design methodology is likely possible only in the ray optics limit, because the wave-optics process of constructing the energy-momentum density tensor and integrating it creates a problem much less amenable to inversion.

In the next sections, we first introduce the concept of bulk and surface optical force densities and briefly explain the Abraham-Minkowski controversy. Then we reach the main part of the work where a general formulation of force-tracing in isotropic and anisotropic media is presented followed by a few worked examples.

5.2 Momentum of Photon in Media and Optical Force

Let us consider Maxwell's equation,

$$\begin{aligned} \vec{\nabla}\cdot\vec{D} &= \rho, & \vec{\nabla}\cdot\vec{B} &= 0, \\ \vec{\nabla}\times\vec{E} &= -\frac{\partial\vec{B}}{\partial t}, & \vec{\nabla}\times\vec{H} &= \vec{j}+\frac{\partial\vec{D}}{\partial t}, \end{aligned} \tag{5.1}$$

where ρ and $\vec{j}$ are free charges and currents, respectively. If we consider the Lorentz force density exerted on free sources as $\vec{f}_s = \rho\vec{E} + \vec{j}\times\vec{B}$ and replace ρ and $\vec{j}$ by $\vec{\nabla}\cdot\vec{D}$ and $\vec{\nabla}\times\vec{H} - \partial\vec{D}/\partial t$ respectively, then after some vector algebraic simplification [22, 112-114], we obtain

$$\frac{\partial\vec{g}_M}{\partial t} + \vec{\nabla}\cdot\vec{T}_M + \vec{f} = 0, \tag{5.2}$$

where $\vec{g}_M = \vec{D}\times\vec{B}$ is the momentum density, $\vec{T}_M = (1/2)\left(\vec{D}\cdot\vec{E} + \vec{B}\cdot\vec{H}\right)\vec{1} - \left(\vec{D}\vec{E} + \vec{B}\vec{H}\right)$ is the stress tensor (momentum current density) and $\vec{1}$ is the unit dyadic. In equation (5.2), $\vec{f} = \vec{f}_b + \vec{f}_s$ is the Lorentz force density acting on both the free and bound sources and $\vec{f}_b$, which is the force density applied to the bound sources, can be written [112, 113]

$$\vec{f}_b = \left(-\vec{\nabla}\cdot\vec{P}\right)\vec{E} + \frac{\partial\vec{P}}{\partial t}\times\vec{B} - \left(\mu_0\vec{\nabla}\cdot\vec{M}\right)\vec{H} - \mu_0\frac{\partial\vec{M}}{\partial t}\times\vec{D}, \tag{5.3}$$

where $\vec{P}$ is the polarization vector, $\vec{M}$ is the magnetization vector, $\rho_e^{bound} = -\vec{\nabla}\cdot\vec{P}$ is the bound electric charge density, $\rho_m^{bound} = -\mu_0\vec{\nabla}\cdot\vec{M}$ is the bound magnetic charge density, $\vec{j}_e^{bound} = \partial\vec{P}/\partial t$ is the bound electric current density and $\vec{j}_m^{bound} = -\mu_0\,\partial\vec{M}/\partial t$ is the bound magnetic current density. Equation (5.2) is actually a demonstration of conservation of momentum in electrodynamics that was first derived by Minkowski. If in a dielectric with refractive index n we write the electromagnetic energy density u in terms of photons as $u = q\hbar\omega/V$, where q is the average number of photons with angular frequency ω in a volume V , and relate it to the electric field intensity, we can immediately obtain the momentum of a single photon in the dielectric medium as np where $p = \hbar\omega/c$ and c is the velocity of light in vacuum.

However, in general the stress tensor (or the energy-momentum tensor) in Minkowski's formulation is not symmetric and it seems to be in contradiction with the conservation of angular momentum. This concern made Abraham introduce a different stress tensor and hence a different momentum density in the momentum conservation equation,

$$\frac{\partial\vec{g}_A}{\partial t} + \vec{\nabla}\cdot\vec{T}_A + \vec{f}_1 + \vec{f} = 0, \tag{5.4}$$

where $\vec{g}_A = \vec{E}\times\vec{H}/c^2$ is the Abraham momentum density, $\vec{T}_A = (1/2)\left(\vec{D}\cdot\vec{E} + \vec{B}\cdot\vec{H}\right)\vec{1} - (1/2)\left(\vec{E}\vec{D} + \vec{D}\vec{E} + \vec{H}\vec{B} + \vec{B}\vec{H}\right)$ is the Abraham stress tensor and $\vec{f}_1$ is called the Abraham force density. In fact, $\vec{f}_1$ is the price to pay for having symmetry in the stress tensor in Abraham's formulation and is exactly what is required to make both formulations equivalent to each other; i.e. $\vec{f}_1 = \left(\partial\vec{g}_M/\partial t - \partial\vec{g}_A/\partial t\right) + \left(\vec{\nabla}\cdot\vec{\vec{T}}_M - \vec{\nabla}\cdot\vec{\vec{T}}_A\right)$. Like the previous case, if we express the energy density in terms of photons and use $\vec{g}_A$ for the momentum density, we find the momentum of photon in the dielectric medium as p/n.

Now we are left with a situation where two seemingly equivalent formulations give two different values for the momentum of a photon within a dielectric; this is the place where the Abraham-Minkowski dilemma appears. From a theoretical point of view, both formulations are accurate in some sense and are grounded in Maxwell's equations. From an experimental point of view, unfortunately the momentum of a photon in a medium cannot be measured directly and it must be interpreted through measurement of other entities. In experiments reported, the momenta measured were affected by the interpretation used, which again can make both interpretations seem correct [97, 115]. Barnett [101, 115] solved this dilemma by recalling the fact that two types of momenta can be attributed to photons; kinetic momentum as the product of the photon associated mass and its velocity (owing to particle nature of photons), and canonical momentum as Planck's constant divided by the photon de Broglie wavelength (owing to the wave nature of photons). The total momentum within a medium then is either the summation of the kinetic momentum of a photon and the kinetic momentum assigned to the matter or the summation of the canonical momentum of the photon and the canonical momentum assigned to the matter. According to Barnett, we have

$$\vec{p}^{\,medium}_{canonical} + \int dV\, \vec{g}_M = \vec{p}^{\,medium}_{kinetic} + \int dV\, \vec{g}_A\,, \tag{5.5}$$

where clearly Abraham's momentum is identified as the kinetic momentum of light and Minkowski's momentum is identified as the canonical momentum of light. In fact, all historical experiments seeming to favor either the Abraham or Minkowski momenta were missing a comprehensive inference of the photon-matter interaction within the medium under observation; this can be traced to equation (5.5).

Lastly, from a macroscopic point of view, any formulation, e.g. the formulation given by Abraham or Einstein-Laub, for conservation of momentum derived directly from Maxwell's equations is equivalent to the Minkowski's formulation provided it yields a correct force density (like $\vec{f}_1$ in Abraham's formulation) exerted within or on a medium. This general equivalence was proven in [97] and its references.

5.3 Force-tracing

As said earlier, the total Lorentz force felt by a medium is the summation of the force acting on free sources ($\vec{f}_s$) and the force acting on bound sources ($\vec{f}_b$). In the absence of free sources within a medium $\vec{f}_s$ vanishes and $\vec{f}_b$ is the force that affects the medium. In a linear non-dispersive medium we have the constitutive equations

$$\begin{cases} \vec{D} = \varepsilon_0 \vec{E} + \vec{P} = \varepsilon_0 \vec{E} + \varepsilon_0 \vec{\chi}_e \cdot \vec{E} \\ \vec{B} = \mu_0 \vec{H} + \mu_0 \vec{M} = \mu_0 \vec{H} + \mu_0 \vec{\chi}_m \cdot \vec{H} \end{cases}, \tag{5.6}$$

where $\vec{\chi}_e$ and $\vec{\chi}_m$ are the electric and magnetic susceptibility tensors, respectively. Using the above constitutive equations in (5.3), we have

$$\begin{aligned}\vec{f}_b &= \left(-\vec{\nabla}\cdot\vec{P}\right)\vec{E} + \frac{\partial\vec{P}}{\partial t}\times\vec{B} - \left(\mu_0\vec{\nabla}\cdot\vec{M}\right)\vec{H} - \mu_0\frac{\partial\vec{M}}{\partial t}\times\vec{D} \\ &= \underbrace{\left(-\vec{\nabla}\cdot\vec{P}\right)\vec{E} + \left(-\mu_0\vec{\nabla}\cdot\vec{M}\right)\vec{H}}_{A} + \frac{\partial\vec{P}}{\partial t}\times\left(\mu_0\vec{H} + \mu_0\vec{\chi}_m\cdot\vec{H}\right) \\ &- \mu_0\frac{\partial\vec{M}}{\partial t}\times\left(\varepsilon_0\vec{E} + \varepsilon_0\vec{\chi}_e\cdot\vec{E}\right) \\ &= A + \frac{\partial\vec{P}}{\partial t}\times\mu_0\vec{H} - \mu_0\frac{\partial\vec{M}}{\partial t}\times\varepsilon_0\vec{E} + \mu_0\varepsilon_0\frac{\partial}{\partial t}\left[\left(\vec{\chi}_e\cdot\vec{E}\right)\times\left(\vec{\chi}_m\cdot\vec{H}\right)\right].\end{aligned} \tag{5.7}$$

If we take the electromagnetic fields as time harmonic fields, then in a linear non-dispersive medium the time-average of the last term in (5.7) becomes zero. Hence the time-averaged bulk force density within the source-free medium would be

$$\left\langle\vec{f}\right\rangle = \frac{1}{2}\mathrm{Re}\left\{\left(-\vec{\nabla}\cdot\vec{P}\right)\vec{E}^* + \left(-\mu_0\vec{\nabla}\cdot\vec{M}\right)\vec{H}^* - i\omega\vec{P}\times\mu_0\vec{H}^* + i\omega\mu_0\vec{M}\times\varepsilon_0\vec{E}^*\right\} \tag{5.8}$$

where $*$ stands for the complex conjugate and "Re" stands for the real part. Equation (5.8) is the same equation introduced in [112-114]. However, in a lossless medium, we have

$$-i\omega\vec{P}\times\mu_0\vec{H}^* + i\omega\mu_0\vec{M}\times\varepsilon_0\vec{E} = -i\omega\varepsilon_0\mu_0\left[\left(\vec{\chi}_e\cdot\vec{E}\right)\times\vec{H}^* + \vec{E}^*\times\left(\vec{\chi}_m\cdot\vec{H}\right)\right]. \tag{5.9}$$

Under the geometrical optics assumption, the right hand side of equation (5.9) is pure imaginary and therefore the contribution of the last two terms in (5.8) is null. And also in source-free regions we can write

$$\vec{\nabla}\cdot\vec{D} = 0 \rightarrow \vec{\nabla}\cdot\vec{P} = -\varepsilon_0\vec{\nabla}\cdot\vec{E}, \tag{5.10}$$

$$\vec{\nabla}\cdot\vec{B} = 0 \rightarrow -\vec{\nabla}\cdot\left(\mu_0\vec{M}\right) = \mu_0\vec{\nabla}\cdot\vec{H}. \tag{5.11}$$

5.3.1 Isotropic Case

Let us consider *isotropic* media first. According to Chapter 2, in the domain of geometrical optics we are allowed to write the electromagnetic fields as,

$$\begin{cases} \vec{E}(\vec{r},t) = \vec{E}_0 \exp\left(ik_0\vec{k}\cdot\vec{r} - i\omega t\right) \\ \vec{H}(\vec{r},t) = \vec{H}_0 \exp\left(ik_0\vec{k}\cdot\vec{r} - i\omega t\right) \end{cases}, \tag{5.12}$$

where ω is the angular frequency, $\vec{k}$ is the wave vector and the magnitudes of both $\vec{E}_0$ and $\vec{H}_0$ are assumed to be approximately constant. In the isotropic media, we know that $\vec{E}_0$, $\vec{H}_0$ and $\vec{k}$ make a right triplet [22] and if we know enough about the directions of two of them, then we can calculate the direction of the third. In this sense, we can construct an arbitrary orthogonal coordinate system in which one of the basis vectors is along $\vec{k}$. If we call two other basis vectors $\hat{e}_z$ and $\hat{e}_t$, then we can decompose the electric field into its components, parallel (in-plane component) and perpendicular (out-of-plane component), to the plane defined by $\vec{k}$ and $\hat{e}_t$. For these two polarizations, we have

$$\begin{cases} In-plane:\ \vec{H}_0 = \hat{e}_z H_0 \,\&\, \vec{E}_0 = \dfrac{\hat{e}_z\times\vec{k}}{\left|\hat{e}_z\times\vec{k}\right|}E_0 \\ Out-of-plane:\ \vec{E}_0 = \hat{e}_z E_0 \,\&\, \vec{H}_0 = \dfrac{\vec{k}\times\hat{e}_z}{\left|\vec{k}\times\hat{e}_z\right|}H_0 \end{cases}. \tag{5.13}$$

Note that in inhomogeneous isotropic media, the direction of $\vec{E}_0$ ($\vec{H}_0$) for the in-plane (out-of-plane) polarization is position dependent. As a result, the divergence of $\vec{E}_0$ ($\vec{H}_0$) for the in-plane (out-of-plane) polarization is not zero,

$$\begin{cases} In-plane:\ \vec{\nabla}\cdot\vec{H}_0 = 0 \ \ \&\ \ \vec{\nabla}\cdot\vec{E}_0 \neq 0 \\ Out-of-plane:\ \vec{\nabla}\cdot\vec{E}_0 = 0 \ \ \&\ \ \vec{\nabla}\cdot\vec{H}_0 \neq 0 \end{cases}. \tag{5.14}$$

However, in homogeneous isotropic media, both $\vec{E}_0$ and $\vec{H}_0$ are vectors of constant amplitude and direction. So their divergences are zero and there exists a null bulk force density within such media. In homogeneous media the only thing which matters is the surface force originating from refraction of the fields at the media interfaces.

Then for the in-plane polarized wave we have,

$$\begin{aligned}\vec{\nabla}\cdot\vec{E}&=\vec{\nabla}\cdot\left(\vec{E}_0 e^{ik_0\vec{k}\cdot\vec{r}-i\omega t}\right)\\&=\vec{E}_0\cdot\vec{\nabla}\left(e^{ik_0\vec{k}\cdot\vec{r}-i\omega t}\right)+\vec{\nabla}\cdot\left(\frac{\hat{e}_z\times\vec{k}}{\left|\hat{e}_z\times\vec{k}\right|}\right)E_0 e^{ik_0\vec{k}\cdot\vec{r}-i\omega t}.\end{aligned}\tag{5.15}$$

Before going further we show that the first term in the right hand side of equation (5.15) does not have any contribution to the bulk force density. If we take $\vec{E}_0=\hat{e}_0E_0$ and $\vec{k}\cdot\vec{r}=k_xx+k_yy+k_zz$, we have

$$\vec{E}_0\cdot\vec{\nabla}\left(e^{ik_0\vec{k}\cdot\vec{r}-i\omega t}\right)=ik_0E_0\left[\left(\hat{e}_0\cdot\hat{e}_x\right)k_x+\left(\hat{e}_0\cdot\hat{e}_y\right)k_y+\left(\hat{e}_0\cdot\hat{e}_z\right)k_z\right]e^{ik_0\vec{k}\cdot\vec{r}-i\omega t}.\tag{5.16}$$

We have to multiply right hand side of (5.16) by $\vec{E}^*$ in order to figure out the contribution of the first term of (5.15) in the bulk force density. Thus we have,

$$\begin{aligned}&\vec{E}_0\cdot\vec{\nabla}\left(e^{ik_0\vec{k}\cdot\vec{r}-i\omega t}\right)\vec{E}^*\\&=ik_0E_0\left[\left(\hat{e}_0\cdot\hat{e}_x\right)k_x+\left(\hat{e}_0\cdot\hat{e}_y\right)k_y+\left(\hat{e}_0\cdot\hat{e}_z\right)k_z\right]e^{ik_0\vec{k}\cdot\vec{r}-i\omega t}\hat{e}_0E_0^*e^{-ik_0\vec{k}\cdot\vec{r}+i\omega t}\\&=\hat{e}_0ik_0\left|E_0\right|^2\left[\left(\hat{e}_0\cdot\hat{e}_x\right)k_x+\left(\hat{e}_0\cdot\hat{e}_y\right)k_y+\left(\hat{e}_0\cdot\hat{e}_z\right)k_z\right].\end{aligned}\tag{5.17}$$

As it is clear, $\vec{E}_0\cdot\vec{\nabla}\left(e^{ik_0\vec{k}\cdot\vec{r}-i\omega t}\right)\vec{E}^*$ is pure imaginary and after time-averaging, its contribution to the bulk force density vanishes.

Then the time-averaged force density for the in-plane polarization with the help of equation (5.8) can be expressed as

$$\left\langle\vec{f}\right\rangle=\frac{\varepsilon_0}{2}\left|E_0\right|^2\vec{\nabla}\cdot\left(\frac{\hat{e}_z\times\vec{k}}{\left|\hat{e}_z\times\vec{k}\right|}\right)\frac{\hat{e}_z\times\vec{k}}{\left|\hat{e}_z\times\vec{k}\right|}.\tag{5.18}$$

Similarly, for the out-of-plane polarization we can obtain the following expression for the force density,

$$\left\langle \vec{f} \right\rangle = \frac{\mu_0}{2}\left|H_0\right|^2 \vec{\nabla}\cdot\left(\frac{\hat{e}_z\times\vec{k}}{\left|\hat{e}_z\times\vec{k}\right|}\right)\frac{\hat{e}_z\times\vec{k}}{\left|\hat{e}_z\times\vec{k}\right|}. \tag{5.19}$$

It should be remembered that for the plane waves, we have $\varepsilon_0\left|E_0\right|^2 = \mu_0\left|H_0\right|^2$. Adding these two, we can express the density of the bulk optical force of unpolarized light in an isotropic medium as

$$\left\langle \vec{f} \right\rangle = \frac{\varepsilon_0}{2}\left|E_0\right|^2 \vec{\nabla}\cdot\left(\frac{\hat{e}_z\times\vec{k}}{\left|\hat{e}_z\times\vec{k}\right|}\right)\frac{\hat{e}_z\times\vec{k}}{\left|\hat{e}_z\times\vec{k}\right|}, \tag{5.20}$$

where $\left|E_0\right|$ is the magnitude of the electric field of the unpolarized light. After some mathematical simplification, we obtain the following expression for the bulk force density within an isotropic medium,

$$\left\langle \vec{f} \right\rangle = \frac{\varepsilon_0\left|E_0\right|^2}{2\left(k_x^2+k_y^2\right)^{3/2}}\left[k_xk_y\left(\frac{\partial k_x}{\partial x}-\frac{\partial k_y}{\partial y}\right)+k_y^2\frac{\partial k_x}{\partial y}-k_x^2\frac{\partial k_y}{\partial x}\right]\frac{\hat{e}_z\times\vec{k}}{\left|\hat{e}_z\times\vec{k}\right|}. \tag{5.21}$$

We know that the Hamiltonian in an isotropic medium is $\mathcal{H} = k_x^2 + k_y^2 - n\left(x,y\right)^2$ and the ray trajectories are calculated on the surface $\mathcal{H} = 0$. Regarding this surface, we can make some simplification as,

$$\frac{\partial k_x}{\partial y} = \frac{\frac{dk_x}{d\tau}}{\frac{dy}{d\tau}} = \frac{\frac{-\partial\mathcal{H}}{\partial x}}{\frac{\partial\mathcal{H}}{\partial k_y}} = \frac{2n\frac{\partial n}{\partial x}}{2k_y} = \frac{n}{k_y}\frac{\partial n}{\partial x}, \tag{5.22}$$

$$\frac{\partial k_y}{\partial x} = \frac{\frac{dk_y}{d\tau}}{\frac{dx}{d\tau}} = \frac{\frac{-\partial\mathcal{H}}{\partial y}}{\frac{\partial\mathcal{H}}{\partial k_x}} = \frac{2n\frac{\partial n}{\partial y}}{2k_x} = \frac{n}{k_x}\frac{\partial n}{\partial y}, \tag{5.23}$$

$$\frac{\partial k_x}{\partial x}=\frac{\dfrac{dk_x}{d\tau}}{\dfrac{dx}{d\tau}}=\frac{\dfrac{-\partial\mathcal{H}}{\partial x}}{\dfrac{\partial\mathcal{H}}{\partial k_x}}=\frac{2n\dfrac{\partial n}{\partial x}}{2k_x}=\frac{n}{k_x}\frac{\partial n}{\partial x}, \tag{5.24}$$

$$\frac{\partial k_y}{\partial y}=\frac{\dfrac{dk_y}{d\tau}}{\dfrac{dy}{d\tau}}=\frac{\dfrac{-\partial\mathcal{H}}{\partial y}}{\dfrac{\partial\mathcal{H}}{\partial k_y}}=\frac{2n\dfrac{\partial n}{\partial y}}{2k_y}=\frac{n}{k_y}\frac{\partial n}{\partial y}. \tag{5.25}$$

Using the above simplification, we can obtain the x-components of the normalized bulk force density as,

$$\begin{aligned}\left\langle \vec{f}_x\right\rangle_{normalized}&=\frac{\left\langle \vec{f}_x\right\rangle}{\dfrac{\varepsilon_0}{2}\left|E_0\right|^2}\\&=\frac{1}{\left(k_x^2+k_y^2\right)^{3/2}}\left[k_xk_y\left(\frac{n}{k_x}\frac{\partial n}{\partial x}-\frac{n}{k_y}\frac{\partial n}{\partial y}\right)+k_y^2\frac{n}{k_y}\frac{\partial n}{\partial x}-k_x^2\frac{n}{k_x}\frac{\partial n}{\partial y}\right]\frac{-k_y}{\left(k_x^2+k_y^2\right)^{1/2}}\\&=\frac{-k_y}{\left(k_x^2+k_y^2\right)^2}2n\left(k_y\frac{\partial n}{\partial x}-k_x\frac{\partial n}{\partial y}\right).\end{aligned} \tag{5.26}$$

On the Hamiltonian surface, we have $k_x^2+k_y^2=n\left(x,y\right)^2$. So inserting this into (5.26) we have,

$$\left\langle \vec{f}_x\right\rangle_{normalized}=\frac{-2k_y}{n\left(x,y\right)^3}\left(k_y\frac{\partial n}{\partial x}-k_x\frac{\partial n}{\partial y}\right) \tag{5.27}$$

Similarly, for the y-component we have,

$$\left\langle \vec{f}_y\right\rangle_{normalized}=\frac{2k_x}{n\left(x,y\right)^3}\left(k_y\frac{\partial n}{\partial x}-k_x\frac{\partial n}{\partial y}\right). \tag{5.28}$$

However we can go further in simplifying equations (5.27) and (5.28). Using the replacements

$$\begin{cases}dk_x/d\tau=-\partial\mathcal{H}/\partial x=2n\left(\partial n/\partial x\right)\rightarrow\partial n/\partial x=\left(1/2n\right)dk_x/d\tau\\dk_y/d\tau=-\partial\mathcal{H}/\partial y=2n\left(\partial n/\partial y\right)\rightarrow\partial n/\partial y=\left(1/2n\right)dk_y/d\tau\end{cases}, \tag{5.29}$$

in equations (5.27) and (5.28) we have,

$$\left\langle \vec{f}_x \right\rangle_{normalized} = \frac{1}{n^4} k_y \left(k_x \frac{dk_y}{d\tau} - k_y \frac{dk_x}{d\tau} \right), \tag{5.30}$$

$$\left\langle \vec{f}_y \right\rangle_{normalized} = \frac{-1}{n^4} k_x \left(k_x \frac{dk_y}{d\tau} - k_y \frac{dk_x}{d\tau} \right). \tag{5.31}$$

If we define $\vec{L}_k = \hat{e}_z \left[k_x \left(dk_y / d\tau \right) - k_y \left(dk_x / d\tau \right) \right]$, then we have

$$\left\langle \vec{f}_x \right\rangle_{normalized} = \frac{1}{n^4} \left(\vec{k} \times \vec{L} \right)_x , \tag{5.32}$$

$$\left\langle \vec{f}_y \right\rangle_{normalized} = \frac{1}{n^4} \left(\vec{k} \times \vec{L} \right)_y . \tag{5.33}$$

Or in another word,

$$\left\langle \vec{f} \right\rangle_{normalized} = \frac{1}{n^4} \left(\vec{k} \times \vec{L} \right). \tag{5.34}$$

Now let us consider the isotropic spherically symmetric medium in which the refractive index profile depends only on r, i.e. $n = n(r)$, while $r = \sqrt{x^2 + y^2}$. For this type of index profile, we have,

$$\frac{\partial n}{\partial x} = \frac{\partial r}{\partial x} \frac{dn}{dr} = \frac{x}{r} \frac{dn}{dr}, \tag{5.35}$$

$$\frac{\partial n}{\partial y} = \frac{\partial r}{\partial y} \frac{dn}{dr} = \frac{y}{r} \frac{dn}{dr}. \tag{5.36}$$

If in equations (5.27) and (5.28), we replace $\partial n / \partial x$ and $\partial n / \partial y$ by what we have from (5.35) and (5.36), we have

$$\left\langle \vec{f}_x \right\rangle_{normalized} = \frac{-2}{n^3} k_y \left(k_y x - k_x y \right) \frac{1}{r} \frac{dn}{dr}, \tag{5.37}$$

$$\left\langle \vec{f}_y \right\rangle_{normalized} = \frac{-2}{n^3} k_x \left(k_y x - k_x y \right) \frac{1}{r} \frac{dn}{dr}. \tag{5.38}$$

Let us define $q = k_y x - k_x y$. Then the derivative of q with respect to τ would be,

$$\frac{dq}{d\tau} = \frac{dk_y}{d\tau} x + k_y \frac{dx}{d\tau} - \frac{dk_x}{d\tau} y - k_x \frac{dy}{d\tau}. \tag{5.39}$$

But from the Hamiltonian of an isotropic medium and also from equations (5.29), (5.35) and (5.36) we have,

$$\frac{dx}{d\tau} = \frac{\partial \mathcal{H}}{\partial k_x} = 2k_x, \tag{5.40}$$

$$\frac{dy}{d\tau} = \frac{\partial \mathcal{H}}{\partial k_y} = 2k_y, \tag{5.41}$$

$$\frac{dk_x}{d\tau} = 2n \frac{\partial n}{\partial x} = 2n \frac{x}{r} \frac{dn}{dr}, \tag{5.42}$$

$$\frac{dk_y}{d\tau} = 2n \frac{\partial n}{\partial y} = 2n \frac{y}{r} \frac{dn}{dr}. \tag{5.43}$$

If we replace the above four expression in (5.39), we have,

$$\frac{dq}{d\tau} = 2n \frac{xy}{r} \frac{dn}{dr} + 2k_x k_y - 2n \frac{xy}{r} \frac{dn}{dr} - 2k_x k_y = 0. \tag{5.44}$$

It means that q is independent of the ray parameter τ or in another word $q = q(\tau) = q(\tau = 0)$. If we assume the ray is initially (at $\tau = 0$) incident into the medium at a point like (x_0, y_0) and in a direction parallel to the positive *x*-axis, i.e. $k_{y0} = 0$ and $k_{x0} = 1$, then for q we have,

$$q = q(\tau = 0) = k_{y0} x_0 - k_{x0} y_0 = 0 - y_0 = -y_0. \tag{5.45}$$

But y_0 is nothing but the impact parameter of the ray b [21]. So we have

$$k_y x - k_x y = -b. \tag{5.46}$$

Finally, the bulk force density components in the spherically symmetric medium would be,

$$\left\langle f_x \right\rangle_{normalized} = \frac{2b}{rn(r)^3} k_y \frac{dn}{dr}, \tag{5.47}$$

$$\left\langle f_y \right\rangle_{normalized} = \frac{-2b}{rn(r)^3} k_x \frac{dn}{dr}. \tag{5.48}$$

Or in a more compact form,

$$\left\langle \vec{f} \right\rangle_{normalized} = \frac{2b}{rn(r)^3} \frac{dn}{dr} \left(\vec{k} \times \hat{e}_z \right). \tag{5.49}$$

It should be recalled that in the geometrical optics, fields are locally plane waves and hence, as can be seen in equations (5.34) and (5.49), we are always able to decompose the force into two components along a plane of interest and the force does not have any component perpendicular to this plane. However, the orientation of the plane changes along a ray trajectory and thus so do the directions of the introduced basis vectors.

For the last word on the isotropic case, we refer back to equation (5.21). With the help of equations (5.22)-(5.25), we can write the magnitude of the normalized bulk force density as,

$$\left| \left\langle \vec{f} \right\rangle \right|_{normalized} = \frac{1}{\left(k_x^2 + k_y^2 \right)^{3/2}} \left[k_y \left(2n \frac{\partial n}{\partial x} \right) - k_x \left(2n \frac{\partial n}{\partial y} \right) \right]. \tag{5.50}$$

From (5.29) we can rewrite (5.50) as,

$$\left| \left\langle \vec{f} \right\rangle \right|_{normalized} = \frac{1}{\left(k_x^2 + k_y^2 \right)^{3/2}} \left[k_y \left(\frac{dk_x}{d\tau} \right) - k_x \left(\frac{dk_y}{d\tau} \right) \right]. \tag{5.51}$$

With knowledge of the Hamiltonian in the isotropic medium, we are allowed to make replacements like,

$$\frac{dk_x}{d\tau}=\frac{1}{2}\frac{d}{d\tau}\left(2k_x\right)=\frac{1}{2}\frac{d}{d\tau}\left(\frac{dx}{d\tau}\right)=\frac{1}{2}\frac{d^2x}{d\tau^2}, \tag{5.52}$$

$$\frac{dk_y}{d\tau}=\frac{1}{2}\frac{d}{d\tau}\left(2k_y\right)=\frac{1}{2}\frac{d}{d\tau}\left(\frac{dy}{d\tau}\right)=\frac{1}{2}\frac{d^2y}{d\tau^2}. \tag{5.53}$$

Utilizing the above replacements and also replacing k_x and k_y from equations (5.40) and (5.41), we can simplify equation (5.51) as,

$$\left|\left\langle \vec{f}\right\rangle\right|_{normalized}=2\frac{\left|\frac{dy}{d\tau}\frac{d^2x}{d\tau^2}-\frac{dx}{d\tau}\frac{d^2y}{d\tau^2}\right|}{\left[\left(\frac{dx}{d\tau}\right)^2+\left(\frac{dy}{d\tau}\right)^2\right]^{3/2}}. \tag{5.54}$$

Interestingly the fraction on the right hand side of equation (5.54) is an important geometrical quantity— the *curvature* (κ) of ray trajectories inside an isotropic medium. In other words,

$$\left|\left\langle \vec{f}\right\rangle\right|_{normalized}=2\kappa. \tag{5.55}$$

In consequence, the bulk force density is directly related to the curvature of the optical rays and therefore we can state a rule of thumb; *the greater the curvature of a light ray, the stronger the bulk force density inside an isotropic medium!*

5.3.2 Anisotropic Case

After settling down the force-tracing technique in isotropic media, now let us consider the *anisotropic* case. We know that in anisotropic media $\vec{D}$, $\vec{B}$ and $\vec{k}$ make a right triplet [22]. In this part, we assign the in-plane and the out-of-plane polarizations with respect to the displacement field $\vec{D}$. In an anisotropic medium we have,

$$\begin{gathered}\vec{D} = \varepsilon_0\vec{E} + \vec{P} = \varepsilon_0\vec{E} + \varepsilon_0\overleftrightarrow{\chi}_e \cdot \vec{E} = \varepsilon_0\left(\overleftrightarrow{I} + \overleftrightarrow{\chi}_e\right)\cdot \vec{E} = \varepsilon_0\overleftrightarrow{\varepsilon}_r \cdot \vec{E} \\ \rightarrow \vec{E} = \frac{1}{\varepsilon_0}\overleftrightarrow{\varepsilon}_r^{-1} \cdot \vec{D},\end{gathered} \tag{5.56}$$

$$\begin{gathered}\vec{B} = \mu_0\vec{H} + \mu_0\vec{M} = \mu_0\vec{H} + \mu_0\overleftrightarrow{\chi}_m \cdot \vec{H} = \mu_0\left(\overleftrightarrow{I} + \overleftrightarrow{\chi}_{m,}\right)\cdot \vec{H} = \mu_0\overleftrightarrow{\mu}_r \cdot \vec{H} \\ \rightarrow \vec{H} = \frac{1}{\mu_0}\overleftrightarrow{\mu}_r^{-1} \cdot \vec{B},\end{gathered} \tag{5.57}$$

where $\overleftrightarrow{\varepsilon}_r$ and $\overleftrightarrow{\mu}_r$ are the relative permittivity and permeability tensors, respectively. If we assume $\vec{D} = \vec{D}_0 e^{ik_0\vec{k}\cdot\vec{r}-i\omega t}$ and $\vec{B} = \vec{B}_0 e^{ik_0\vec{k}\cdot\vec{r}-i\omega t}$, then for the in-plane and the out-of-plane polarizations we can write

$$\begin{cases} In-plane: \ \vec{B}_0 = \hat{e}_z B_0 \,\&\, \vec{D}_0 = \dfrac{\hat{e}_z \times \vec{k}}{\left|\hat{e}_z \times \vec{k}\right|} D_0 \\ Out-of-plane: \ \vec{D}_0 = \hat{e}_z D_0 \,\&\, \vec{B}_0 = \dfrac{\vec{k} \times \hat{e}_z}{\left|\vec{k} \times \hat{e}_z\right|} B_0 \end{cases}. \tag{5.58}$$

According to equations (5.56)-(5.58), it is seen that the electric field $\vec{E} = \vec{E}_0 e^{ik_0\vec{k}\cdot\vec{r}-i\omega t}$ and the magnetic field $\vec{H} = \vec{H}_0 e^{ik_0\vec{k}\cdot\vec{r}-i\omega t}$ inside the anisotropic medium are oriented as,

$$\begin{cases} In-plane: \ \vec{H}_0 = \dfrac{\overleftrightarrow{\mu}_r^{-1}\cdot\hat{e}_z}{\left|\overleftrightarrow{\mu}_r^{-1}\cdot\hat{e}_z\right|} H_0 \,\&\, \vec{E}_0 = \dfrac{\overleftrightarrow{\varepsilon}_r^{-1}\cdot\left(\hat{e}_z \times \vec{k}\right)}{\left|\overleftrightarrow{\varepsilon}_r^{-1}\cdot\left(\hat{e}_z \times \vec{k}\right)\right|} E_0 \\ Out-of-plane: \ \vec{E}_0 = \dfrac{\overleftrightarrow{\varepsilon}_r^{-1}\cdot\hat{e}_z}{\left|\overleftrightarrow{\varepsilon}_r^{-1}\cdot\hat{e}_z\right|} E_0 \,\&\, \vec{H}_0 = \dfrac{\overleftrightarrow{\mu}_r^{-1}\cdot\left(\vec{k} \times \hat{e}_z\right)}{\left|\overleftrightarrow{\mu}_r^{-1}\cdot\left(\vec{k} \times \hat{e}_z\right)\right|} H_0 \end{cases}. \tag{5.59}$$

As a result, by inserting the electric and magnetic fields into equation (5.8), we obtain the following expression for the bulk force density of the in-plane polarization,

$$\begin{aligned}\left\langle \vec{f} \right\rangle = \frac{\varepsilon_0}{2}\left|E_0\right|^2 \vec{\nabla}\cdot\left(\frac{\vec{\vec{\varepsilon}}_r^{-1}\cdot\left(\hat{e}_z\times\vec{k}\right)}{\left|\vec{\vec{\varepsilon}}_r^{-1}\cdot\left(\hat{e}_z\times\vec{k}\right)\right|}\right)\frac{\vec{\vec{\varepsilon}}_r^{-1}\cdot\left(\hat{e}_z\times\vec{k}\right)}{\left|\vec{\vec{\varepsilon}}_r^{-1}\cdot\left(\hat{e}_z\times\vec{k}\right)\right|} \\ +\frac{\mu_0}{2}\left|H_0\right|^2 \vec{\nabla}\cdot\left(\frac{\vec{\vec{\mu}}_r^{-1}\cdot\hat{e}_z}{\left|\vec{\vec{\mu}}_r^{-1}\cdot\hat{e}_z\right|}\right)\frac{\vec{\vec{\mu}}_r^{-1}\cdot\hat{e}_z}{\left|\vec{\vec{\mu}}_r^{-1}\cdot\hat{e}_z\right|}.\end{aligned} \tag{5.60}$$

Similarly for the out-of-plane polarization we have,

$$\begin{aligned}\left\langle \vec{f} \right\rangle = \frac{\mu_0}{2}\left|H_0\right|^2 \vec{\nabla}\cdot\left(\frac{\vec{\vec{\mu}}_r^{-1}\cdot\left(\vec{k}\times\hat{e}_z\right)}{\left|\vec{\vec{\mu}}_r^{-1}\cdot\left(\vec{k}\times\hat{e}_z\right)\right|}\right)\frac{\vec{\vec{\mu}}_r^{-1}\cdot\left(\vec{k}\times\hat{e}_z\right)}{\left|\vec{\vec{\mu}}_r^{-1}\cdot\left(\vec{k}\times\hat{e}_z\right)\right|} \\ +\frac{\varepsilon_0}{2}\left|E_0\right|^2 \vec{\nabla}\cdot\left(\frac{\vec{\vec{\varepsilon}}_r^{-1}\cdot\hat{e}_z}{\left|\vec{\vec{\varepsilon}}_r^{-1}\cdot\hat{e}_z\right|}\right)\frac{\vec{\vec{\varepsilon}}_r^{-1}\cdot\hat{e}_z}{\left|\vec{\vec{\varepsilon}}_r^{-1}\cdot\hat{e}_z\right|}.\end{aligned} \tag{5.61}$$

5.3.3 Surface Force Density

In addition to the bulk force, there exists another force, *surface force*. This force is due to discontinuities at media interfaces which reflect or refract incident light. At the interface of a medium, the force density equation (5.8) can be written as [22, 112-114],

$$\left\langle \vec{f} \right\rangle = \frac{1}{2}\mathrm{Re}\left\{\rho_e \vec{E}_{av}^* + \rho_h \vec{H}_{av}^*\right\}, \tag{5.62}$$

where $\rho_e = \varepsilon_0 \hat{e}_n \cdot \left(\vec{E}_{out} - \vec{E}_{in}\right)$, $\rho_h = \mu_0 \hat{e}_n \cdot \left(\vec{H}_{out} - \vec{H}_{in}\right)$, $\vec{E}_{av} = \left(\vec{E}_{out} + \vec{E}_{in}\right)/2$, $\vec{H}_{av} = \left(\vec{H}_{out} + \vec{H}_{in}\right)/2$, $\hat{e}_n$ is the unit vector normal to the interface pointing out of the medium, and $\left(\vec{E}_{out}, \vec{H}_{out}\right)$ and $\left(\vec{E}_{in}, \vec{H}_{in}\right)$ are the outside and inside fields at the interface of the medium, respectively. If we assume $\vec{E}_{in} = \hat{e}_{e2} E_0 e^{ik_0\vec{k}_2\cdot\vec{r} - i\omega t}$, $\vec{H}_{in} = \hat{e}_{h2} H_0 e^{ik_0\vec{k}_2\cdot\vec{r} - i\omega t}$, $\vec{E}_{out} = \hat{e}_{e1} E_0 e^{ik_0\vec{k}_1\cdot\vec{r} - i\omega t}$ and $\vec{H}_{out} = \hat{e}_{h1} H_0 e^{ik_0\vec{k}_1\cdot\vec{r} - i\omega t}$, then we have,

$$\vec{E}_{av} = \frac{1}{2}\left(\hat{e}_{e2}E_0 e^{ik_0\vec{k}_2\cdot\vec{r}} + \hat{e}_{e1}E_0 e^{ik_0\vec{k}_1\cdot\vec{r}}\right), \tag{5.63}$$

$$\vec{H}_{av} = \frac{1}{2}\left(\hat{e}_{h2}H_0 e^{ik_0\vec{k}_2\cdot\vec{r}} + \hat{e}_{h1}H_0 e^{ik_0\vec{k}_1\cdot\vec{r}}\right), \tag{5.64}$$

$$\rho_e = \varepsilon_0 \hat{e}_n \cdot \left(\hat{e}_{e1}E_0 e^{ik_0\vec{k}_1\cdot\vec{r}} - \hat{e}_{e2}E_0 e^{ik_0\vec{k}_2\cdot\vec{r}}\right), \tag{5.65}$$

$$\rho_h = \mu_0 \hat{e}_n \cdot \left(\hat{e}_{h1}H_0 e^{ik_0\vec{k}_1\cdot\vec{r}} - \hat{e}_{h2}H_0 e^{ik_0\vec{k}_2\cdot\vec{r}}\right). \tag{5.66}$$

If we let $\hat{e}_n \cdot \hat{e}_{e1} = \cos\psi_e$, $\hat{e}_n \cdot \hat{e}_{e2} = \cos\psi'_e$, $\hat{e}_n \cdot \hat{e}_{h1} = \cos\psi_h$ and $\hat{e}_n \cdot \hat{e}_{h2} = \cos\psi'_h$, for $\rho_e \vec{E}^*_{av}$ we have,

$$\begin{aligned}\rho_e \vec{E}^*_{av} &= \frac{1}{2}\varepsilon_0 \left(\cos\psi_e E_0 e^{ik_0\vec{k}_1\cdot\vec{r}} - \cos\psi'_e E_0 e^{ik_0\vec{k}_2\cdot\vec{r}}\right) \\ &\quad \times \left(\hat{e}_{e2}E_0^* e^{-ik_0\vec{k}_2\cdot\vec{r}} + \hat{e}_{e1}E_0^* e^{-ik_0\vec{k}_1\cdot\vec{r}}\right) \\ &= \frac{1}{2}\varepsilon_0 \left|E_0\right|^2 \Big[\left(\cos\psi_e e^{ik_0\left(\vec{k}_1-\vec{k}_2\right)\cdot\vec{r}} - \cos\psi'_e\right)\hat{e}_{e2} \\ &\quad + \left(\cos\psi_e - \cos\psi'_e e^{ik_0\left(\vec{k}_2-\vec{k}_1\right)\cdot\vec{r}}\right)\hat{e}_{e1}\Big].\end{aligned} \tag{5.67}$$

Due to the phase matching [22], the exponential terms can be set equal to one. Thus equation (5.67) can be written like,

$$\rho_e \vec{E}^*_{av} = \frac{1}{2}\varepsilon_0 \left|E_0\right|^2 \left(\cos\psi_e - \cos\psi'_e\right)\left(\hat{e}_{e2} + \hat{e}_{e1}\right). \tag{5.68}$$

Similarly for $\rho_h \vec{H}^*_{av}$, we have,

$$\rho_h \vec{H}^*_{av} = \frac{1}{2}\mu_0 \left|H_0\right|^2 \left(\cos\psi_h - \cos\psi'_h\right)\left(\hat{e}_{h2} + \hat{e}_{h1}\right). \tag{5.69}$$

Finally, the surface force density would be

$$\begin{aligned}\left\langle \vec{f}_{surf} \right\rangle = \frac{1}{2}\varepsilon_0 \left|E_0\right|^2 \Big[&\left(\cos\psi_e - \cos\psi'_e\right)\left(\hat{e}_{e2} + \hat{e}_{e1}\right) \\ &+ \left(\cos\psi_h - \cos\psi'_h\right)\left(\hat{e}_{h2} + \hat{e}_{h1}\right)\Big].\end{aligned} \tag{5.70}$$

5.3.4 Results and Discussion

After setting up the theoretical foundation of the force tracing process, in this section we work several examples. As a first example we consider the bulk force distribution in an Eaton lens. The ray trajectories in the Eaton lens are parts of ellipses which share a focal point at the center, and if the ambient medium is vacuum, the incident rays do not feel any disturbance at the Eaton lens boundary (i.e. $n(r)=1$ at the boundary). Due to this transparency, there exists no surface force at the boundary. But by gradual change of the index, the trajectories of the rays bend gradually and therefore an optical force proportional to the curvature of the rays would be felt inside the lens.

In order to explain what really happens to a photon traveling inside an Eaton lens, we borrow the idea of Balazs [79] about photon-dielectric interaction. In the Balazs model, a photon of frequency ω is propagating towards a transparent dielectric box of rest mass M and refractive index n. The box is assumed to be located at rest on a frictionless surface. Before entering the box, the energy and the momentum of the photon is $\hbar\omega$ and $\hbar\omega/c$ (the associated mass of the photon is $\hbar\omega/c^2$) and therefore the total energy and momentum of the system is $E=\hbar\omega+Mc^2$ and $P=\hbar\omega/c$. (It should be noted that this P is different from what we used for the polarization vector in equation (5.8).) When the photon enters the box, its kinetic momentum would be $\hbar\omega/nc$ and hence the box picks up a momentum of $(\hbar\omega/c)(1-1/n)$ and starts to move with a velocity v which can be calculated through conservation of momentum. When the photon later exits the box, its momentum would be $\hbar\omega/c$ and hence the box stops moving. We can consider a similar story for a photon's journey within an Eaton lens. Consider two adjacent points on a ray trajectory like Q_i and Q_{i+1} in an Eaton lens, as shown in Fig. 5.1. At point Q_i the photon has the kinetic momentum $\hbar\omega / n_{Qi}c$, where n_{Qi} is the value of the Eaton index profile at Q_i. When the photon travels from this point to point Q_{i+1}, its kinetic momentum changes to $\hbar\omega / n_{Qi+1}c$. Because of this change, the Eaton lens picks up a kinetic momentum like $\left(\hbar\omega / n_{Qi}c\right) - \left(\hbar\omega / n_{Qi+1}c\right)$ and moves along a direction parallel to the difference of the two momentum vectors and at a speed determined by the conservation of energy and mass of the Eaton lens. Now let us consider $N+1$ points on the path of the photon which are uniformly distributed and located infinitesimally close to one another ($N \to \infty$). When the photon moves from point A to point Q_0, it imposes a momentum like $\Delta\vec{p}_0 = \vec{p}_A - \vec{p}_{Q0}$ on the lens. Then from its trip from point Q_0 to point Q_1, the photon offers the momentum $\Delta\vec{p}_1 = \vec{p}_{Q0} - \vec{p}_{Q1}$ to the lens. This momentum interchange between the photon and the lens takes place recursively along the rest of the path till the photon reaches point B and exits the lens. In aggregate, the momentum grabbed by the lens due to the propagation of the photon would be,

$$\vec{p}_{AB} = \vec{p}_A - \vec{p}_B = \sum_{i=0}^{N+1} \Delta\vec{p}_i \,. \tag{5.71}$$

where this momentum is proportional to the total force exerted on the lens. In the limiting case of $N \to \infty$, equation (5.71) can be written as,

$$\vec{p}_{AB} = \int_C d\vec{p} \propto \textit{optical force} \tag{5.72}$$

where C refers to the path of the photon.

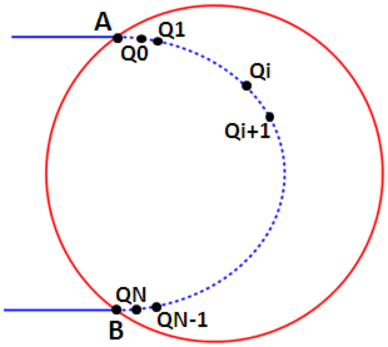

Fig. 5.1**.** The path of a photon within an Eaton lens. The photon enters the lens at point A and exits at point B.

In order to find the optical force distribution inside an Eaton lens, we need to use equation (5.49). To do so, we can calculate the optical force density along an arbitrary ray which can be parameterized with parameter τ. Shown in Figs. 5.2(a) and (b) are the bulk force density illustrated by black arrows along several ray trajectories and the bulk force distribution within the lens, respectively. One of the rays is shown in purple. The magnitude of the corresponding force density along this ray is depicted in Fig. 5.2(c). In addition, in order to show the validity of equation (5.55), the curvature ($2\times\kappa$) of the ray traced in purple is shown in Fig. 5.2(c) and as seen it is completely overlapping the normalized magnitude curve.

The trajectories of light rays in isotropic media can be determined by the Euler-Lagrange equation [21] (which can be broken into the set of the Hamilton equations) and based on this equation the ray tracing parameter τ is given by $d\tau = dl/n$, where dl is the infinitesimal increment of the geometrical path length and n is the refractive index. In order to find the total force along a ray's path we need to integrate the force density along the entire path and according to the previous mentioned note the total force would be $\left\langle \vec{F} \right\rangle_{normalized} = \int \left\langle \vec{f}(\tau) \right\rangle_{normalized} n\, d\tau$.

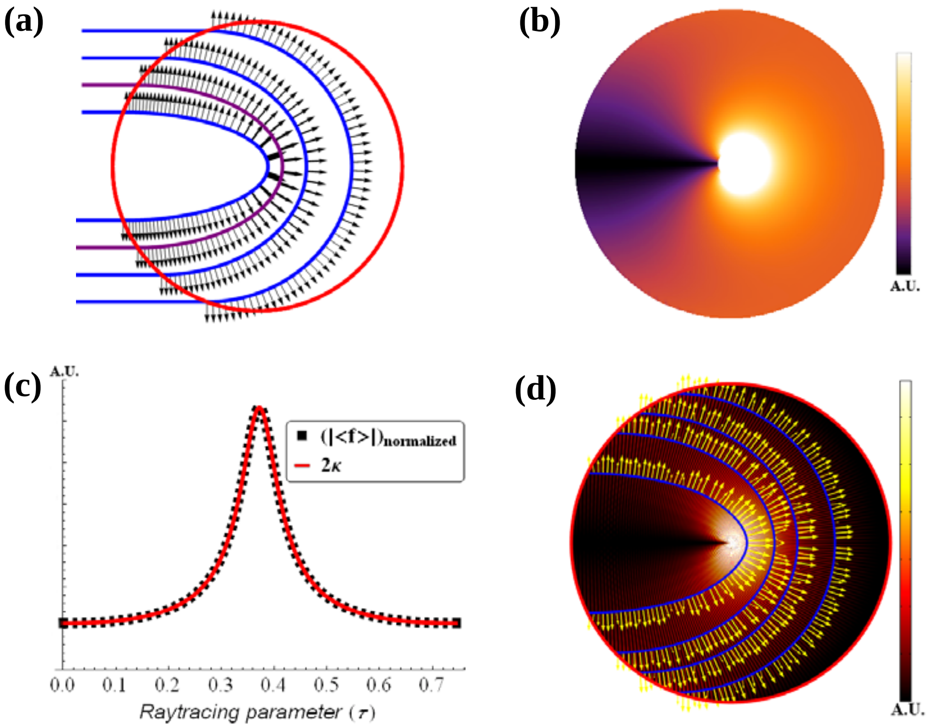

Fig. 5.2. (a) The normalized bulk force density arrows (distinguished by their thicknesses) traced along rays within an Eaton lens of unit radius. (b) The distribution of the normalized bulk force density (magnitude) inside the lens. (c) The magnitude of the normalized bulk force density versus the ray curvature (2κ) along the ray depicted in purple. (d) The force arrows (distinguished by their lengths) and the distribution of the normalized bulk force density (magnitude) inside the Eaton lens calculated through full-wave simulation (wavelength of the simulation is 0.05 units).

As seen in Figs. 5.2(a) and (b), the optical force increases at near the center of an Eaton lens where there is an index singularity. In other words, the optical force is proportional to the curvature of the rays and in the vicinity of a singularity the optical force in this region blows up. This is depicted at the centers of Figs. 5.2(a) and (b). This can also be vividly interpreted in Fig. 5.2(c), where the curve shows a sharp peak near the middle of the ray curve and obviously the peak gets sharper and sharper as the impact parameter of the ray decreases. The other interesting thing about the Eaton lens is the symmetry of the force distribution with respect to the horizontal axis (x axis). As seen in Fig. 5.2(b), the rays with tiny impact parameters initially cause very small forces and as they approach the singularity they face a sudden change in their trajectory and their mechanical interactions with the lens jumps up abruptly. However, this fluctuation in the force density becomes smoother as the impact parameter of the rays increases. In order to validate our analysis, we performed a full-wave simulation with a finite element technique using commercial software COMSOL to numerically calculate the force density inside an Eaton lens. The simulation result is given in Fig. 5.2(d). It is seen that the force-tracing analysis is in a good agreement with the full-wave simulation; nevertheless in the full-wave simulation, some force arrows along each ray have different heights. This is related to wave interference within the lens, and the locations of the regions of reduced force density are wavelength dependent (the wavelength simulated was slightly too large for an exact comparison to the geometric optics case—this was unfortunately necessary however, because full-wave simulations with shorter wavelengths would require additional/significant computational resources).

As another example, we consider the Luneburg lens in which incident parallel rays are focused at the back of the lens. The Luneburg lens is a spherically symmetric lens with the index profile $n(r)=\sqrt{2-r^2}$ where ray trajectories are (different) sections of ellipses [21]. Making use of equation (5.49), we can calculate the force distribution inside a Luneburg lens as depicted in Fig. 5.3. Like the previous case, in Figs. 5.3(a) and (b) the force density along individual ray trajectories and the bulk force distribution are depicted, respectively. In Fig. 5.3(a), one ray is chosen arbitrarily and traced in purple. The magnitude of the force density and the curvature ($2\times\kappa$) for the ray highlighted in purple are depicted in Figure 5.3(c), which again confirms the validity of equation (5.55). The lens feels maximum pressure at initial and final points along the ray's trajectory and minimum pressure exactly at the midpoint of the trajectory, for the curvature of the elliptic trajectory inside is the smallest there. It is seen that the rays with higher impact parameters impose higher force than those with lower impact parameters; the ray with zero impact parameter does not have any interaction with the lens. It can also be explained by the curvature of the trajectories. Shown in Fig. 5.3(d) is the full-wave calculation of force density inside the Luneburg lens in COMSOL, which is an indication of agreement between the proposed force-tracing method and the full-wave analysis.

As shown in Fig. 5.3(a), when many parallel rays enter a Luneburg lens, they propagate along trajectories to accumulate at a single point and exit at various angles corresponding to their impact parameters, and as a result the lens is pushed by the incoming rays. This is somehow vivid, for the projection of the outgoing rays' momenta along the horizontal axis is less than the corresponding momenta of the incoming rays and hence this reduction of their net momenta causes a pushing force. Conversely if many rays were to enter a Luneburg lens from a single point, they would exit in parallel and their momenta along one axis would increase during their trip within the lens and it would cause a pulling force on the lens along that axis [116-118]. These two facts are illustrated schematically in Figs. 5.4(a) and (b).

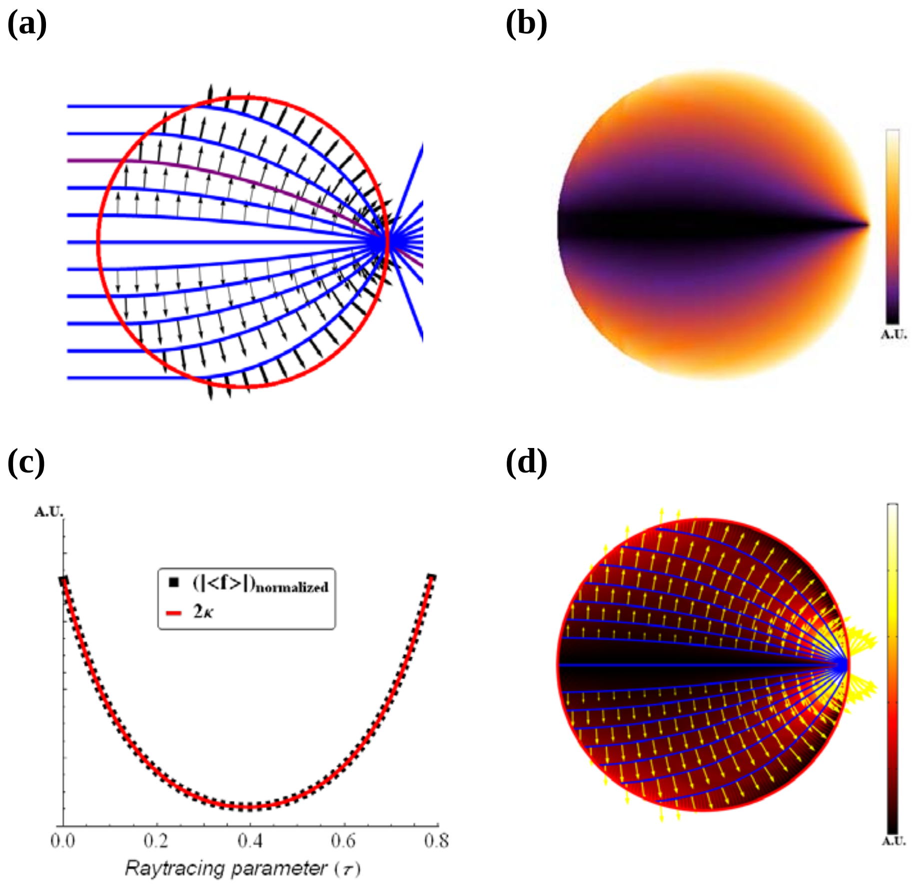

Fig. 5.3. (a) The normalized bulk force density arrows (distinguished by their thicknesses) traced along the rays within a Luneburg lens of radius 1. (b) The distribution of the normalized bulk force density (magnitude) inside the lens. (c) The magnitude of the normalized bulk force density versus the ray curvature (2κ) along the ray depicted in purple. (d) The force arrows (distinguished by their lengths) and the distribution of the normalized bulk force density (magnitude) inside the Luneburg lens calculated via full-wave simulation (wavelength of the simulation is 0.05 units).

In our final example, we examine the optical force within an invisible cloak [5, 37] designed through transformation optics; this is an anisotropic index profile. It is known that one can design an infinite number of cloaks to make an object invisible [119] but in this analysis we assume a simple case,

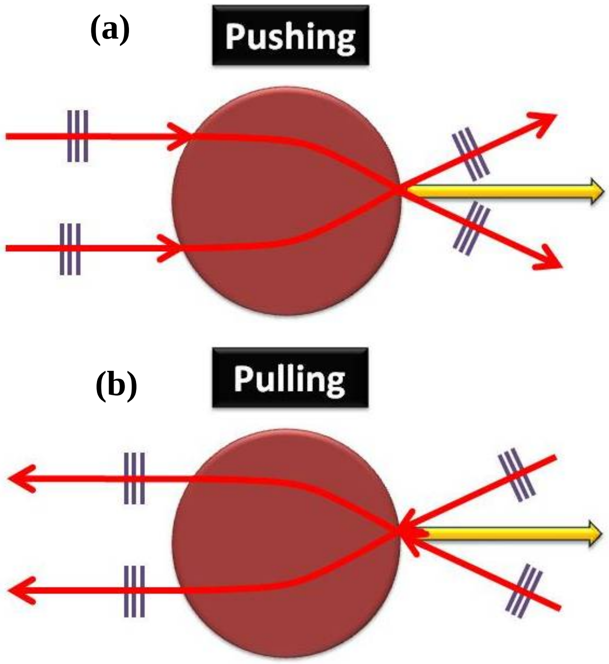

Fig. 5.4. (a) The pushing force case in the Luneburg lens. (b) The pulling force case in the Luneburg lens.

$$\vec{\varepsilon}_r = \vec{\mu}_r = diag\left\{\xi_r, \xi_\theta, \xi_\phi\right\} = diag\left\{\frac{R_2}{R_2 - R_1}\left(\frac{r - R_1}{r}\right)^2, \frac{R_2}{R_2 - R_1}, \frac{R_2}{R_2 - R_1}\right\} \tag{5.73}$$

where *diag* stands for a diagonal tensor, and R_2 and R_1 are the radii of the outer and inner boundaries of the cloak, respectively. It should be noted that since $\vec{\varepsilon}_r = \vec{\mu}_r$ in the cloak, no reflection takes place at the boundary of cloak and all the light goes through the device. But there exists refraction at the boundary of cloak which causes light rays to bend abruptly at that point. Hence contrary to the two previous examples in which we had only a bulk force, in the case of this cloak a surface force also appears. Utilizing equations (5.60), (5.61) and (5.70), we calculate the force distribution along the $\theta = \pi/2$ plane for a cloak with dimensions $R_2 = 1$ and $R_1 = 0.25$. Shown in Fig. 5.5 is the force distribution within the spherical cloak for in-plane polarized light.

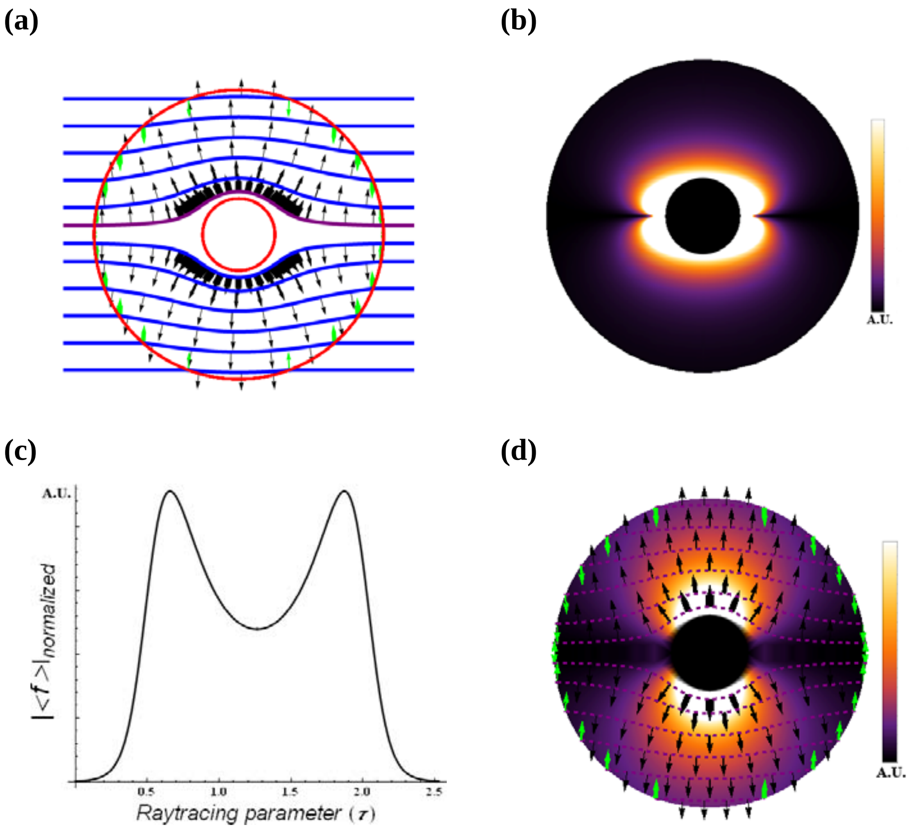

Fig. 5.5. (a) The normalized bulk (black) and surface (green) force density arrows (distinguished by their thicknesses) traced along the rays within a cloak of inner radius of 0.25 and outer radius of 1. (b) The distribution of the normalized bulk force density (magnitude) inside the lens. (c) The magnitude of the normalized force density along the ray depicted in purple. (d) The normalized bulk (black) and surface (green) force density arrows and the distribution of the normalized bulk force density (magnitude) inside the cloak calculated from analytical expressions.

As seen in Figure 5.5(a), near the focal points of the ray trajectory (where the curvature changes its sign) we have a maximum in the force distribution and due to the spherical symmetry, there are two of these maximum force density points along each ray trajectory. In addition, as we go further from the cloaked region the rays feel less force; this makes sense, because the outer rays are not as curved as the inner rays. It is interesting to see that the surface force (the green arrows) is directed inward while the bulk force is pointing outward and also the surface force is an order of magnitude less than the bulk force. The plot of the bulk force density is shown in Fig. 5.5(b). At points near the cloaked region, the force is much larger than it is near the outer lens boundary and this is related to the presence of a singularity at $r = R_1$. It should be noted that our calculation of the force density at points very close to the singularity may not be accurate enough—at such points we are out of the domain of geometrical optics. However, as can be seen from Fig. 5.5(a), all the force density arrows cancel each other out and the total force on the perfect cloak is zero as it should be. To ensure the validity of our force-tracing calculations, (as shown in Fig. 5.5(d)) we calculate the bulk and surface force densities from the analytical full-wave expressions given in [114]. It is seen that the agreement between our geometrical optics based analysis and the analytical analysis is quite acceptable. However, the force density distributions are clearly not the same. In the ray optics analysis that we have developed, the maximal bulk force density occurs when ray curvature is maximal and the maximal surface force density occurs where refraction is the greatest; in the full-wave analysis, these both occur along a vertical cutline through the cloak center. While the difference is not large between the two analyses, we find it to be an interesting limitation of geometrical optics, since all the conditions that would normally permit the use of geometrical optics have otherwise been met. Although we are unable to explain the specific reason for the differences in the two analyses in this example, we have found an even more remarkable example of this type of breakdown of geometrical optics which we will now describe.

As is evident in Fig. 5.5(a), the force field is mirror symmetric about a vertical cutline through the cloak. When a ray enters the cloak from the left side, in its first half trip, it causes a force with a negative horizontal component and in its second half trip, it exerts a force with a positive horizontal component and these two components cancel out each other. The surface force densities are at least ten times smaller than the bulk force densities. Now consider cutting the cloak in half so that only the left side remains. With the right half gone, one might conclude that a half cloak could be pulled by an incident plane wave! It would be remarkable, if it were the case. But due to the inability of geometrical optics to account for some phenomena like diffraction, some part of truth has been hidden in such an interpretation (not to mention that it would violate conservation of momentum). In order to make it clear why such a half-cloak tractor beam is impossible even though force-tracing says it is possible, we compare the ray analysis and full-wave analysis of a half cloak in Figs. 5.6(a) and (b). In the ray analysis, a half cloak produces a completely dark shadow, or in other words, a perfect hollow beam, and the outgoing rays do not have any interference with one another. However, in reality the light exiting a half cloak is diffracted, which makes the shadow formed behind the half-cloak incomplete. So the diffraction, not predicted by the ray analysis, is responsible for creating some pushing forces which aggregately overcome the negative horizontal components of the bulk force density. Therefore the net force on a half-cloak by an incident plane wave is pushing. As it is beyond the scope of this chapter, we are not to calculate this pushing force, though it would be noteworthy if someone carries out the full computation of such a pushing force.

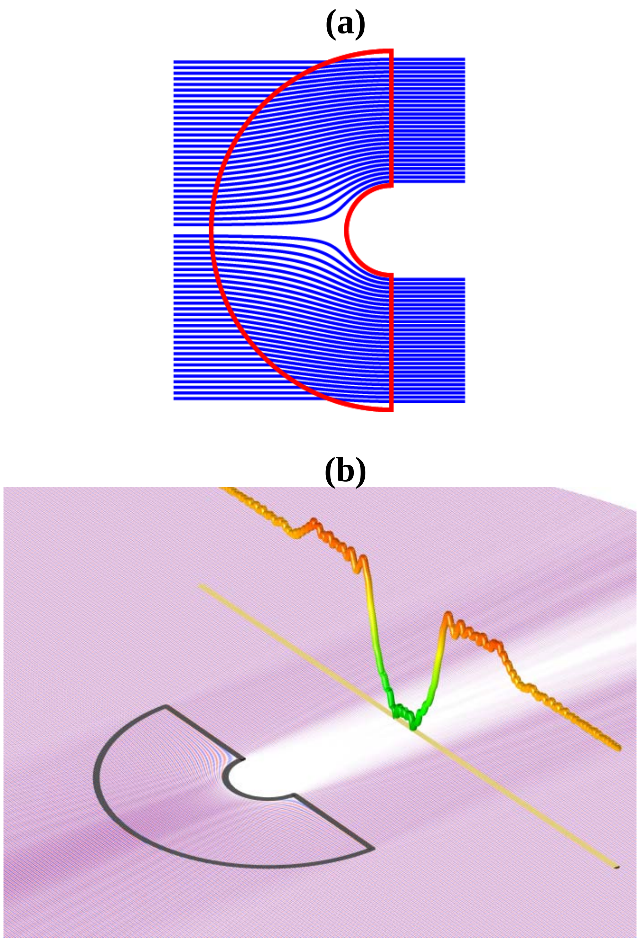

Fig. 5.6. (a) The ray trajectories of a half-cloak. (b) The full-wave simulation result for the magnitude of the electric field for a half-cloak; the magnitude of the electric field at a cutline located across the path of the outgoing wave is drawn to illustrate the diffraction pattern outside the half-cloak more clearly (wavelength of the simulation is 0.025).

5.4 Conclusions

In conclusion, we reviewed the conservation of light momentum in general and discussed the Abraham-Minkowski dilemma. With the aid of the geometrical optics toolset, we proposed a formulation for calculating the time-averaged bulk and surface Lorentz force densities within linear optical materials. Owing to the genuine simplicity of geometrical optics machinery, the formulation is much simpler than full-wave analysis and the standard process of integrating the stress tensor(s). In order to demonstrate the validity of our formulation, we considered two isotropic lenses (Eaton and Luneburg lens) and one anisotropic device (perfect spherical cloak) and calculated their bulk and surface force densities. It is hoped that this presentation of light-media interactions from a simple perspective can become a useful tool in calculating the optical forces within media under the constraints of geometrical optics; in many practical situations, it gives significantly identical solutions to much more cumbersome full-wave methods. As a future work, one may put an effort to propose a (probably semi-numerical) method to obtain isotropic or even anisotropic optical profiles with a desired force distribution. Moreover, complex theories like transformation optics and conformal mapping can be invoked in the prospective method(s) to shape the optical forces in anomalous ways useful for specific applications.

CHAPTER 6 Summary and Future Work

6.1 Summary

As alluded to in the introduction, the consideration of complex media, along with their accompanying fantastical properties, anomalies and subtleties, has made life much more exciting than it was in the recent past for the scientific community, and has brought the chance to the young as well as established researchers to reconsider the basics of electrodynamics and optics. With a temptation toward chasing after new ideas and challenges, fast and furious hunger for fame and publication, in addition to the excitement of revisiting old ideas and thoughts in new frames of reference, has caused a revolution in this field. As a result, being equipped with the luxury of complex media and the limitless power of creativity, designers have come up with many astounding optical devices and designs. However, in many of these works, fact and fiction can sometimes be difficult to tell apart, and that is exactly where the leading edge of technologies can be found. Borrowing the ideas from films and science fiction and translating them into the language of science and engineering, new technological objectives that require increasing structural complexity in their designs are pursued nowadays. Cloaking shells, optical lenses with unlimited resolutions, optical illusions, ultrathin foldable electronic devices and screens, extremely fast transistors and optical trapping and pulling are several examples of such objectives. In spite of immensely fast growth, everlasting debates and of course the involvement of practical issues, we found it interesting and instructive to explore the behavior of complex media from the geometrical optics point of view. Geometrical optics, with its language of rays, is an old and strong method in analyzing optical devices. Even though there exists some must-meet criteria for its use to be valid, geometrical optics brings ease in terms of mathematical calculation complexity and provides the central inspiration required for optical designs, especially in the domain of complex media.

We initiated this thesis with the definition of complexity in a medium and we addressed the necessary criteria according to which we can classify and model the complex media quantitatively. The foundation of transformation optics, complementary media and the space folding in complex media were also reviewed. We chose to follow a geometrical optics approach in our analyses and designs and to study light's interactions with complex media with the language of rays. Hence at the first step, by employing the elements of tensor calculus we wrote the governing optical Hamiltonian and therefore the ray equations in a coordinate-free scheme which can be applied in orthogonal or non-orthogonal and Euclidean or non-Euclidean spaces and geometries. This generalized method was applied for uniaxial and biaxial media as special cases and with a straightforward algebraic method the Hamiltonian in biaxial media was factorized. The validity of the generalized formulation was also examined via studying the transmuted Eaton lens.

Based on the theory of complementary media, we proposed a reverse method to design two-dimensional and three-dimensional superscatterers. As we then discussed in more detail, the proposed reverse method can bring about several benefits like controlling the isotropy of the designed lens and the light distribution in it. Additionally, photorealistic rendering of the superscattering mechanism was carried out and the corresponding ray formations as well as the image properties within the designed lenses were discussed.

Using the factorized expression for the Hamiltonian in biaxial media, we showed that how we can control the behavior of light in two orthogonal planes in a geometry. As an example, we designed a spherically symmetric lens which offers two functions in its equatorial plane and two functions in its polar planes according to the polarization of the applied light. Equalizing the two functions in each of the mentioned planes, we could design a Janus device for the unpolarized light.

And finally we considered the interesting case of force tracing. Due to a connection between the energy current density and momentum current density through conservation equations in electrodynamics, we came to this idea that not only the energy flow (ray path) but also the momentum flow (force density) can be traced in a medium. With the help of the eikonal equation and the Lorentz force, we derived general expressions for the bulk and surface force densities in isotropic and anisotropic media under the geometrical optics approximation. We specifically showed that in isotropic media, the optical force density is directly proportional to the curvature of the ray trajectory. We studied the optical force in three example graded-index devices and showed the validity of our analysis. We also highlighted a situation (i.e. half-cloak) in which the estimations based on force tracing may not be reliable and full-wave analysis is unavoidable.

6.2 Future Work

In the previous chapters, on the basis of Fermat's principle and the analogy of classical optics to Newtonian mechanics, we discussed the analysis and design of graded-index devices, i.e. devices with position dependent profile indices. But in all the designs and even in our generalized formulation, we neglected nonlinearities present in media. As a step forward, it would be worthwhile to study nonlinear electrodynamics under the geometrical optics limitations. Revisiting Fermat's principle in nonlinear media and relating it to the respective Lagrangian would possibly introduce new understandings in the physics of ray optics and may extend the domain of geometrical optics to new borders. Specifically, consideration of the complex features of the *k*-surface and the consequent multirefringence [120] in nonlinear media in addition to the unusual nature of reflection and refraction of light at the interfaces of nonlinear media due to the generation of harmonics [121], brings about a high chance to design interesting devices with unordinary optical properties, though the ray tracing analysis may be very tedious and demanding. As a matter of fact, contrary to its challenging physics and the pertaining complexities, the graded-index nonlinear metamaterial is a very rich area of exploration in physics and surely it is to lead to ground-breaking metadevices.

Another interesting case to consider in future work in the realm geometrical optics is investigating the ray optics of *bi-media*: *bi-anisotropic* and *bi-isotropic media*. We know that in a bi-anisotropic medium we have [22, 122],

$$\vec{D} = \varepsilon_0 \vec{\varepsilon} \cdot \vec{E} + \frac{1}{c} \vec{\xi} \cdot \vec{H} \tag{6.1}$$

$$\vec{B} = \frac{1}{c} \vec{\eta} \cdot \vec{E} + \mu_0 \vec{\mu} \cdot \vec{H} \tag{6.2}$$

where $\vec{\xi}$ and $\vec{\eta}$ are the tensors relating $\vec{H}$ and $\vec{E}$ to $\vec{D}$ and $\vec{B}$, respectively.

If under the geometrical optics approximation, we consider quasi-plane waves with slowly changing magnitudes like,

$$\vec{E} = \overrightarrow{\mathscr{E}} \exp\left(ik_0\vec{k}\cdot\vec{r} - i\omega t\right) \tag{6.3}$$

$$\vec{H} = \frac{1}{\eta_0}\overrightarrow{\mathscr{H}} \exp\left(ik_0\vec{k}\cdot\vec{r} - i\omega t\right) \tag{6.4}$$

then according to the source-free Maxwell equations we have,

$$\vec{k}\times\overrightarrow{\mathscr{E}} = \overleftrightarrow{\eta}\cdot\overrightarrow{\mathscr{E}} + \overleftrightarrow{\mu}\cdot\overrightarrow{\mathscr{H}} \tag{6.5}$$

$$\vec{k}\times\overrightarrow{\mathscr{H}} = -\overleftrightarrow{\varepsilon}\cdot\overrightarrow{\mathscr{E}} - \overleftrightarrow{\xi}\cdot\overrightarrow{\mathscr{H}} \tag{6.6}$$

Solving for $\overrightarrow{\mathscr{H}}$ in (6.5) and inserting it into (6.6) we have,

$$\vec{k}\times\left(\hat{\mu}^{-1}\,\vec{k}\times\overrightarrow{\mathscr{E}}\right) = \left(\overleftrightarrow{\xi}\cdot\overleftrightarrow{\mu}^{-1}\cdot\overleftrightarrow{\eta} - \overleftrightarrow{\varepsilon}\right)\cdot\overrightarrow{\mathscr{E}} - \overleftrightarrow{\xi}\cdot\overleftrightarrow{\mu}^{-1}\cdot\left(\vec{k}\times\overrightarrow{\mathscr{E}}\right) + \vec{k}\times\left(\overleftrightarrow{\mu}^{-1}\cdot\overleftrightarrow{\eta}\cdot\overrightarrow{\mathscr{E}}\right) \tag{6.7}$$

Or equivalently we can write equation (6.7) as,

$$M^{pk}\mathscr{E}_k = 0 \tag{6.8}$$

where for M^{pk} we have,

$$\begin{aligned} M^{pk} = {} & \left(\mu^{-1}\right)^{mi} e^{pn}{}_{m} e_{i}{}^{jk} k_n k_j + \varepsilon^{pk} - \xi^{pl}\left(\mu^{-1}\right)_{l}{}^{m} \eta_{m}{}^{k} \\ & + \xi^{pl}\left(\mu^{-1}\right)_{l}{}^{m} e^{nk}{}_{m} k_n - \left(\mu^{-1}\right)^{ml} \eta_{l}{}^{k} e^{pn}{}_{m} k_n \end{aligned} \tag{6.9}$$

To obtain a nontrivial solution for equation (6.8), we should have,

$$\mathcal{H} = \det\left(M^{pk}\right) = 0 \tag{6.10}$$

where $\mathcal{H}$ is the Hamiltonian of the bi-anisotropic medium. For a bi-isotropic medium, in which the constitutive parameters are scalar, equation (6.7) is simplified as,

$$\vec{k}\times\left(\vec{k}\times\overrightarrow{\mathscr{E}}\right) + \left(\xi-\eta\right)\vec{k}\times\overrightarrow{\mathscr{E}} + \left(\mu\varepsilon - \xi\eta\right)\overrightarrow{\mathscr{E}} = 0 \tag{6.11}$$

And consequently the matrix M would be,

$$M = \begin{bmatrix} -\left(k_2^2+k_3^2\right)+\beta & k_1k_2+\alpha k_3 & k_1k_3-\alpha k_2 \\ k_1k_2-\alpha k_3 & -\left(k_1^2+k_3^2\right)+\beta & k_2k_3+\alpha k_1 \\ k_1k_3+\alpha k_2 & k_2k_3-\alpha k_1 & -\left(k_1^2+k_2^2\right)+\beta \end{bmatrix} = K + X \qquad (6.12)$$

where K is the same matrix as what we defined in Chapter 2, $X = \begin{bmatrix} \beta & \alpha k_3 & -\alpha k_2 \\ -\alpha k_3 & \beta & \alpha k_1 \\ \alpha k_2 & -\alpha k_1 & \beta \end{bmatrix}$, $\alpha = \eta - \xi$ and $\beta = \mu\varepsilon - \xi\eta$.

Chiral materials are one well-known type of bi-media and they have been thoroughly investigated in the literature [51, 122-128]. In isotropic chiral media the constitutive equations are as follows [123, 124],

$$\vec{D} = \varepsilon\vec{E} + i\gamma\vec{B} \qquad (6.13)$$

$$\vec{H} = i\gamma\vec{E} + \left(1/\mu\right)\vec{B} \qquad (6.14)$$

If we assume time harmonic monochromatic waves within chiral media, then based on Maxwell's equation it is shown that [123, 124],

$$\vec{\nabla}\times\vec{\nabla}\times\vec{E} - 2\omega\mu\gamma\,\vec{\nabla}\times\vec{E} - k^2\vec{E} = 0 \qquad (6.15)$$

where $k = \omega\sqrt{\mu\varepsilon}$. Taking the electromagnetic waves in the chiral media as plane waves like $\vec{E}\left(\vec{r},t\right) = \vec{E}_0 e^{i\left(\vec{h}\cdot\vec{r}-\omega t\right)}$, from equation (6.15) we obtain,

$$\left(k^2 - h^2\right)^2 - 4\omega^2\mu^2\gamma^2h^2 = 0 \qquad (6.16)$$

Equation (6.16) is the characteristic equation in the chiral media and solving this equation for h, we have,

$$h = \pm\omega\mu\gamma \pm \sqrt{\omega^2\mu^2\gamma^2 + k^2} \qquad (6.17)$$

where the plus sign represents a right-handed circularly polarized wave and the minus sign is for a left-handed circularly polarized wave propagating within the chiral media. So any plane wave impinging onto a chiral medium interface breaks into right and left-handed circularly polarized waves with different phase velocities. In other words we observe a sort of birefringence in the chiral media, though the media are assumed isotropic. By taking this fact into account in addition to employing proper inhomogeneities, one may come up with interesting ideas to control the formation of the polarized rays and design useful devices.

On the basis of geometrical optics analysis in bi-anisotropic media, we also get prepared to study the behavior of rays and media in motion. It is known that a moving isotropic medium looks as if it were bi-anisotropic in a stationary laboratory reference frame and with the use of the special theory of relativity one can derive the constitutive relations for a moving isotropic medium as [22],

$$\vec{D} = \varepsilon \overleftrightarrow{A} \cdot \vec{E} + \vec{\Omega} \times \vec{H} \tag{6.18}$$

$$\vec{B} = \mu \overleftrightarrow{A} \cdot \vec{E} - \vec{\Omega} \times \vec{E} \tag{6.19}$$

where

$$\overleftrightarrow{A} = \frac{1-\beta^2}{1-n^2\beta^2}\left(\overleftrightarrow{1} - \frac{n^2-1}{1-\beta^2}\vec{\beta}\vec{\beta}\right), \tag{6.20}$$

$$\vec{\Omega} = \frac{n^2-1}{1-n^2\beta^2}\frac{\vec{\beta}}{c}, \tag{6.21}$$

where $\vec{\beta} = \vec{v}/c$, $\vec{v}$ is the velocity of the medium, c is the velocity of light in free space, and n is the refractive index, ε is the permittivity and μ is the permeability of the medium at rest. It should be noted that for inhomogeneous media the permittivity and permeability are dependent of position coordinates pertaining to the rest frame and these dependence should be transformed to the laboratory frame. Attaining the skill of ray tracing in bi-anisotropic media, one would then be able to analyze and to control the formation of optical ray trajectories in motion. As an example, the bi-anisotropic constitutive tensor of an Eaton lens in motion can be derived. Then with the use of that, the ray trajectories within the lens as well as geometrical deformation of the lens boundary at different velocities, from low to relativistic, can be compared and beautiful inspiring photorealistic animations can be rendered. Obviously, it goes without mentioning that the whole process in this example would be very challenging and demanding of lots of lengthy computations, though it is definitely worth it.

In addition to ray tracing, analysis of the optical force on moving objects can be a good prospective task to consider. Energy and momentum of light have been studied for almost a century. As we know through classical work on the optical force, impinging light induces electric and magnetic dipoles inside small particles and these dipoles are new sources of radiation. So, finding these radiated fields and using energy and momentum conservation laws, the optical force can be calculated. This process has been done in some literature like [129], but considering the optical force on particles in motion or on particles immersed in moving media seems to be interesting and bring more physics into the game. As is well known [130-133], one of the two postulates in the special theory of relativity states that the velocity of light in any inertial system in vacuum is fixed and equal to $1/\sqrt{\mu_0\varepsilon_0}$. So for all inertial systems in a vacuum, we have

$$\vec{D} = \varepsilon_0 \vec{E} \tag{6.22}$$

$$\vec{B} = \mu_0 \vec{H} \tag{6.23}$$

Now consider an isotropic, homogeneous and non-dispersive medium with permittivity ε , permeability μ and conductivity σ to be moving with velocity $\vec{v}$ relative to the inertial system I . Then the constitutive relations in the inertial frame I', in which the medium is assumed to be at rest, are

$$\vec{D}' = \varepsilon \vec{E}' \tag{6.24}$$

$$\vec{B}' = \mu \vec{H}' \tag{6.25}$$

$$\vec{J}_c' = \sigma \vec{E}' \tag{6.26}$$

Writing the fields in the rest frame ($\vec{D}', \vec{E}', \vec{B}', \vec{H}'$) with respect to the those in the moving frame ($\vec{D}, \vec{E}, \vec{B}, \vec{H}$) according to the Lorentz transformation, we have the new constitutive relations in the moving frame as [133],

$$\vec{D} + \frac{1}{c^2} \vec{v} \times \vec{H} = \varepsilon \left(\vec{E} + \vec{v} \times \vec{B} \right) \tag{6.27}$$

$$\vec{B} - \frac{1}{c^2} \vec{v} \times \vec{E} = \mu \left(\vec{H} - \vec{v} \times \vec{D} \right) \tag{6.28}$$

$$\vec{J}_c = \gamma \sigma \left[\vec{E} - \frac{1}{c^2} \vec{v} \left(\vec{v} \cdot \vec{E} \right) + \vec{v} \times \vec{B} \right] \tag{6.29}$$

where $\gamma = 1 \big/ \sqrt{1-\beta^2}$, $\beta = v / c$ and $v = |\vec{v}|$. Lorentz transformations can be used to find such relationships for more complex media such as inhomogeneous or dispersive media. On the other hand, we know that the induced electric and magnetic dipole moments due to the incidence of a plane wave, i.e. $\vec{E}_i = \vec{e}_i \exp\left(i\vec{k} \cdot \vec{r} - i\omega t \right)$ and $\vec{B}_i = \vec{b}_i \exp\left(i\vec{k} \cdot \vec{r} - i\omega t \right)$, can be written in terms of the corresponding polarizabilities as,

$$\vec{p} = \alpha_e \vec{e}_i \tag{6.30}$$

$$\vec{m} = \alpha_m \vec{b}_i \tag{6.31}$$

where α_e and α_m are electric and magnetic polarizabilities, respectively. We also know that the time-averaged optical force on a *small particle* at rest and immersed in a host medium is [129],

$$\left\langle \vec{F} \right\rangle = \frac{\vec{k}}{2} \mathrm{Im}\left\{ \vec{p} \cdot \vec{e}_i^{\,*} + \vec{m} \cdot \vec{b}_i^{\,*} \right\} - \frac{n}{c} \int_S \left\langle \vec{S}_r \right\rangle dS \tag{6.32}$$

where $\left\langle \vec{S}_r \right\rangle = (c/8\pi)\mathrm{Re}\left\{ \vec{E}_r \times \vec{H}_r \right\}$ is the time-averaged energy current density, $\vec{E}_r$ and $\vec{H}_r$ are the scattered electric and magnetic fields, n is the refractive index of the host medium, S is any closed surface circumscribing the particle and $*$ stands for the complex conjugate operation. So according to the previous discussion, by employing Lorentz transformation we can find the constitutive relations and fields in a moving frame with respect to a frame at rest. So, intuitively we should be able to take the motion of particles or the host medium into account and find the optical force, radiation pressure, extinction cross section and in general the energy-momentum tensor. On the top of that that, with the help of ray tracing technique in bi-media, we would be able to trace the optical force distribution within moving objects under geometrical optics limitations.

Bibliography

[1] V. G. Veselago, "Electrodynamics of Substances with Simultaneously Negative Values of Sigma and Mu μυ," *Sov. Phys. Usp.,* vol. 10, pp. 509-514, 1968.

[2] R. A. Shelby, D. R. Smith, and S. Schultz, "Experimental Verification of a Negative Index of Refraction," *Science,* vol. 292, pp. 77-79, 2001.

[3] V. N. Smolyaninova, I. I. Smolyaninov, A. V. Kildishev, and V. M. Shalaev, "Maxwell Fish-Eye and Eaton Lenses Emulated by Microdroplets," *Opt. Lett.,* vol. 35, pp. 3396-3398, 2010.

[4] U. Leonhardt, "Optical Conformal Mapping," *Science,* vol. 312, pp. 1777-1780, 2006.

[5] J. B. Pendry, D. Schurig, and D. R. Smith, "Controlling Electromagnetic Fields," *Science* vol. 312, pp. 1780-1782, 2006.

[6] J. B. Pendry, "Negative Refraction Makes a Perfect Lens," *Phys. Rev. Lett.,* vol. 85, pp. 3966-3969, 2000.

[7] U. Leonhardt, "Perfect Imaging without Negative Refraction," *New J. Phys.,* vol. 11, p. 093040, Sep 2009.

[8] Z. Duan, B. L. Wu, J. Lu, J. A. Kong, and M. Chen, "Reversed Cherenkov Radiation in a Waveguide Filled with Anisotropic Double-Negative Metamaterials," *J. Appl. Phys.,* vol. 104, p. 063303, 2008.

[9] N. Seddon and T. Bearpark, "Observation of the Inverse Doppler Effect," *Science,* vol. 302, pp. 1537-1540, 2003.

[10] G. Dolling, C. Enkrich, M. Wegener, C. M. Soukoulis, and S. Linden, "Simultaneous Negative Phase and Group Velocity of Light in a Metamaterial," *Science,* vol. 312, pp. 892-894, 2006.

[11] S. Qiao, G. Zheng, H. Zhang, and L. Ran, "Transition Behavior of k-Surface: From Hyperbola to Ellipse," *Prog. Electromagn. Res,* vol. 81, pp. 267-277, 2008.

[12] B. Luk'yanchuk, N. I. Zheludev, S. A. Maier, N. J. Halas, P. Nordlander, H. Giessen, *et al.*, "The Fano Resonance in Plasmonic Nanostructures and Metamaterials," *Nat. Mater.,* vol. 9, pp. 707-715, 2010.

[13] M. Fiebig, "Revival of the Magnetoelectric Effect," *J. Phys. D: Appl. Phys.,* vol. 38, pp. 123-152, 2005.

[14] C. L. Holloway, E. F. Kuester, J. Baker-Jarvis, and P. Kabos, "A Double Negative (DNG) Composite Medium Composed of Magnetodielectric Spherical Particles Embedded in a Matrix," *IEEE Trans. Antennas Propag.,* vol. 51, pp. 2596-2603, 2003.

[15] V. M. Kenkre, L. Skala, M. W. Weiser, and J. D. Katz, "Theory of Microwave Interactions in Ceramic Materials- The Phenomenon of Thermal Runaway," *J. Mater. Sci.,* vol. 26, pp. 2483-2489, 1991.

[16] P. C. Kim and D. G. Lee, "Composite Sandwich Constructions for Absorbing the Electromagnetic Waves," *Compos. Struct.,* vol. 87, pp. 161-167, 2009.

[17] R. H. Baughman, A. A. Zakhidov, and W. A. d. Heer, "Carbon Nanotubes - The Route Toward Applications," *Science,* vol. 297, pp. 787-792, 2002.

[18] A. K. Geim and K. S. Novoselov, "The Rise of Graphene," *Nat. Mater.,* vol. 6, pp. 183-191, 2007.

[19] A. Sihvola, "Metamaterials in Electromagnetics," *Metamaterials,* vol. 1, pp. 2-11, 2007.

[20] M. Born and E. Wolf, *Principles of Optics: Electromagnetic Theory of Propagation, Interference and Diffraction of Light.* Cambridge: Cambridge University Press, 1999.

[21] U. Leonhardt and T. G. Philbin, *Geometry and Light: The Science of Invisibility* NY: Dover, 2010.

[22] J. A. Kong, *Electromagnetic Wave Theory* NY: Wiley, 1986.

[23] R. Liu, C. Ji, J. J. Mock, J. Y. Chin, T. J. Cui, and D. R. Smith, "Broadband Ground-Plane Cloak," *Science,* vol. 323, pp. 366-369, 2009.

[24] Y. Lai, H. Y. Chen, Z. Q. Zhang, and C. T. Chan, "Complementary Media Invisibility Cloak that Cloaks Objects at a Distance Outside the Cloaking Shell," *Phys. Rev. Lett.,* vol. 102, p. 093901, 2009.

[25] T. Yang, H. Y. Chen, X. D. Luo, and H. R. Ma, "Superscatterer: Enhancement of Scattering with Complementary Media," *Opt. Express,* vol. 16, pp. 18545-18550, 2008.

[26] M. Rahm, S. A. Cummer, D. Schurig, J. B. Pendry, and D. R. Smith, "Optical Design of Reflectionless Complex Media by Finite Embedded Coordinate Transformations," *Phys. Rev. Lett.,* vol. 100, p. 063903, 2008.

[27] T. Han, C. W. Qiu, and X. H. Tang, "Adaptive Waveguide Bends with Homogeneous, Nonmagnetic, and Isotropic Materials," *Opt. Lett.,* vol. 36, pp. 181-183, 2011.

[28] A. V. Kildishev and V. M. Shalaev, "Engineering Space for Light via Transformation Optics," *Opt. Lett.,* vol. 33, pp. 43-45, 2008.

[29] S. Han, Y. Xiong, D. Genov, Z. W. Liu, G. Bartal, and X. Zhang, "Ray Optics at a Deep-Subwavelength Scale: A Transformation Optics Approach," *Nano Lett.,* vol. 8, pp. 4243-4247, 2008.

[30] B. Zhang and G. Barbastathis, "Dielectric Metamaterial Magnifier Creating a Virtual Color Image with Far-Field Subwavelength Information," *Opt. Express,* vol. 18, pp. 11216-11222, 2010.

[31] H. Hashemi, B. Zhang, J. D. Joannopoulos, and S. G. Johnson, "Delay-Bandwidth and Delay-Loss Limitations for Cloaking of Large Objects," *Phys. Rev. Lett.,* vol. 104, p. 253903, 2010.

[32] J. B. Pendry and S. A. Ramakrishna, "Focusing Light Using Negative Refraction," *J. Phys.: Condens. Matter,* vol. 15, pp. 6345-6364, 2003.

[33] A. Akbarzadeh and A. J. Danner, "Generalization of Ray Tracing in a Linear Inhomogeneous Anisotropic Medium: A Coordinate-Free Approach," *J. Opt. Soc. Am. A* vol. 27, pp. 2558-2562, 2010.

[34] C. W. Qiu, A. Akbarzadeh, T. Han, and A. J. Danner, "Photorealistic Rendering of a Graded Negative-Index Metamaterial Magnifier," *New J. Phys. ,* vol. 14, p. 033024, 2012.

[35] A. Akbarzadeh, T. Han, A. J. Danner, and C. W. Qiu, "Generalization of Superscatterer Design and Photorealistic Raytracing Thereof," presented at the Progress In Electromagnetic Research Symposium (PIERS), Kuala Lumpur, Malaysia, March 2012.

[36] A. Akbarzadeh, C. W. Qiu, and A. J. Danner, "Exploiting Design

Freedom in Biaxial Dielectrics to Enable Spatially Overlapping Optical Instruments," *Sci. Rep.,* vol. 3, p. 2055, 2013.

[37] A. Akbarzadeh, C. W. Qiu, and A. J. Danner, "Biaxial Anisotropy in Gradient Permittivity Dielectric Optical Instruments," presented at the Progress In Electromagnetic Research Symposium (PIERS), Kuala Lumpur, Malaysia, March 2012.

[38] A. J. Danner and A. Akbarzadeh, "Biaxial Anisotropy: A Survey of Interesting Optical Phenomena in Graded Media," presented at the International Conference on Metamaterials, Photonic Crystals and Plasmonics (META), Paris, France, April 2012.

[39] A. Akbarzadeh, C. W. Qiu, T. Tyc, and A. J. Danner, "Visualization of Pulse Propagation and Optical Force in Graded-Index Optical Devices," presented at the Progress In Electromagnetic Research Symposium (PIERS), Stockholm, Sweden, August 2013.

[40] U. Leonhardt and T. Tyc, "Broadband Invisibility by Non-Euclidean Cloaking," *Science,* vol. 323, pp. 110-112, 2009.

[41] M. Rahm, D. Schurig, D. A. Roberts, S. A. Cummer, D. R. Smith, and J. B. Pendry, "Design of Electromagnetic Cloaks and Concentrators Using Form-Invariant Coordinate Transformations of Maxwell's Equations," *Photon. Nanostruct.: Fundam. Applic.,* vol. 6, pp. 87-95, 2008.

[42] N. A. Mortensen, "Prospects for Poor-Man's Cloaking with Low-Contrast All-Dielectric Optical Elements," *J. Europ. Opt. Soc.,* vol. 4, p. 09008, 2009.

[43] J. E. Eaton, "On Spherically Symmetric Lenses," *IRE Trans. Antennas Propag.,* vol. 4, pp. 66-71, 1952.

[44] T. Tyc and U. Leonhardt, "Transmutation of Singularities in Optical Instruments," *New J. Phys.,* vol. 10, p. 115038, 2008.

[45] O. N. Stavroudis, "Ray-Tracing Formulas for Uniaxial Crystals," *J. Opt. Soc. Am.,* vol. 52, pp. 187–191, 1962.

[46] Q. T. Liang, "Simple Ray Tracing Formulas for Uniaxial Optical Crystals," *Appl. Opt.,* vol. 29, pp. 1008-1010, 1990.

[47] S. C. McClain, L. W. Hillman, and R. A. Chipman, "Polarization Ray Tracing in Anisotropic Optically Active Media. I. Algorithms," *J. Opt. Soc. Am. A,* vol. 10, pp. 2371-2382, 1993.

[48] S. C. McClain, L. W. Hillman, and R. A. Chipman, "Polarization Ray Tracing in Anisotropic Optically Active Media. II. Theory and Physics," *J. Opt. Soc. Am. A,* vol. 10, pp. 2383-2393, 1993.

[49] M. Sluijter, D. K. G. d. Boer, and J. J. M. Braat, "General Polarized Ray-Tracing Method for Inhomogeneous Uniaxially Anisotropic Media," *J. Opt. Soc. Am. A,* vol. 25, pp. 1260-1273, 2008.

[50] D. Schurig, J. B. Pendry, and D. R. Smith, "Calculation of Material Properties and Ray Tracing in Transformation Media," *Opt. Express,* vol. 14, pp. 9794-9804, 2006.

[51] C. W. Qiu, H. Y. Yao, L. W. Li, S. Zouhdi, and T. S. Yeo, "Backward Waves in Magnetoelectrically Chiral Media: Propagation, Impedance, and Negative Refraction," *Phys. Rev. B,* vol. 75, p. 155120, 2007.

[52] M. V. Berry and M. R. Jeffrey, "Conical Diffraction: Hamilton's Diabolical Point at the Heart of Crystal Optics," *Prog. Opt.* , vol. 50, pp. 13-50, 2007.

[53] M. Sluijter, D. K. G. d. Boer, and H. P. Urbach, "Ray-Optics Analysis of Inhomogeneous Biaxially Anisotropic Media," *J. Opt. Soc. Am. A* vol. 26, pp. 317-329, 2009.

[54] W. R. Hamilton, "Third Supplement to an Essay on the Theory of Systems of Rays," *Trans. Royal Irish Acad.* , vol. 17, pp. 1-144, 1837.

[55] R. K. Luneburg, *Mathematical Theory of Optics*. CA: Univ. of California Press, 1964.

[56] Z. C. Ruan and S. H. Fan, "Superscattering of Light from Subwavelength Nanostructures," *Phys. Rev. Lett.,* vol. 105, p. 013901, 2010.

[57] S. M. Nie and S. R. Emery, "Probing Single Molecules and Single Nanoparticles by Surface-Enhanced Raman Scattering," *Science,* vol. 275, pp. 1102-1106, 1997.

[58] C. J. Foot, *Atomic Physics*. NY: Oxford University Press, 2005.

[59] W. H. Wee and J. B. Pendry, "Shrinking Optical Devices," *New J. Phys.,* vol. 11, p. 073033, 2009.

[60] H. Y. Chen, "Transformation Optics in Orthogonal Coordinates," *J. Opt. A: Pure Appl. Opt.,* vol. 11, p. 075102, 2009.

[61] A. J. Danner, T. Tyc, and U. Leonhardt, "Controlling Birefringence in Dielectrics," *Nat. Photon.* , vol. 5, pp. 357-359, 2011.

[62] C. A. Swainson (alias J. C. Maxwell), "Problems," *Cambridge Dublin Math. J.,* vol. 8, pp. 188-189, 1854.

[63] J. C. Miñano, "Perfect Imaging in a Homogeneous Three-Dimensional Region," *Opt. Express,* vol. 14, pp. 9627-9635, 2006.

[64] V. N. Smolyaninova, H. K. Ermer, A. Piazza, D. Schaefer, and I. I. Smolyaninov, "Experimental Demonstration of Birefrigent Transformation Optics Devices," *Phys. Rev. B* vol. 87, p. 075406, 2013.

[65] J. Li and J. B. Pendry, "Hiding under the Carpet: A New Strategy for Cloaking," *Phys. Rev. Lett.,* vol. 101, p. 203901, 2008.

[66] V. M. Shalaev, "Optical Negative-Index Metamaterials," *Nat. Photon.* , vol. 1, pp. 41-48, 2007.

[67] A. Boltasseva and V. M. Shalaev, "Fabrication of Optical Negative-Index Metamaterials: Recent Advances and Outlook," *Metamaterials* vol. 2, pp. 1-17, 2008.

[68] T. Zentgraf, J. Valentine, N. Tapia, J. Li, and X. Zhang, "An Optical “Janus” Device for Integrated Photonics," *Adv. Mater.* , vol. 22, pp. 2561-2564, 2010.

[69] A. J. Danner, "Singularity Removal in Optical Instruments without Reflections or Induced Birefringence " *New J. Phys.* , vol. 12, p. 113008, 2010.

[70] J. C. Maxwell, *A Treatise on Electricity and Magnetism* Oxford: Clarendon, 1904.

[71] A. Bartoli, " Il Calorico Raggiante e il Secondo Principio di Termodynamica," *Nouvo Cimento* vol. 15, pp. 196-202, 1884.

[72] P. N. Lebedev, "Investigations on the Pressure Forces of Light," *Ann. Phys.* , vol. 6, pp. 433–458, 1901.

[73] E. F. Nichols and G. F. Hull, "The Pressure Due to Radiation," *Phys. Rev.,* vol. 17, pp. 26–50, 1903.

[74] E. F. Nichols and G. F. Hull, "The Pressure due to Radiation,"

Astrophys. J., vol. 57, pp. 315–351, 1903.

[75] H. Minkowski, "Die Grundgleichungen für die Elektromagnetischen Vorgänge in Bewegten Körpern," *Nachr. Ges. Wiss. Goettingen, Math. Phys. K1,* pp. 53-111, 1908.

[76] H. Minkowski, "The Basic Equations for Electromagnetic Processes in Moving Bodies," *Math. Ann.* , vol. 68, pp. 472–525, 1910.

[77] M. Abraham, "On the Electrodynamics of Moving Bodies," *Rend. Circ. Mat. Palermo* vol. 28, pp. 1–28, 1909.

[78] M. Abraham, "On Minkowski's Electrodynamics," *Rend. Circ. Mat. Palermo,* vol. 30, pp. 33–46, 1910.

[79] N. L. Balazs, "The Energy-Momentum Tensor of the Electromagnetic Field inside Matter," *Phys. Rev.* , vol. 91, pp. 408–411, 1953.

[80] P. Penfield and H. A. Haus, *Electrodynamics of Moving Media*. MA: MIT Press, 1967.

[81] S. R. d. Groot and L. G. Suttorp, *Foundations of Electrodynamics*. Amsterdam: North-Holland, 1972.

[82] J. P. Gordon, "Radiation Forces and Momenta in Dielectric Media," *Phys. Rev. A* vol. 8, pp. 14–21, 1973.

[83] Z. Mikura, "Variational Formulation of the Electrodynamics of Fluids and its Application to the Radiation Pressure Problem," *Phys. Rev. A* vol. 13, pp. 2265-2275, 1976.

[84] R. Peierls, "The Momentum of Light in a Refracting Medium," *Proc. R. Soc. London Ser. A* vol. 347, pp. 475–491, 1976.

[85] R. Peierls, "The Momentum of Light in a Refracting Medium. II. Generalization. Application to Oblique Reflexion," *Proc. R. Soc. London Ser. A* vol. 355, pp. 141–151, 1977.

[86] M. Kranyš, "About the Equivalence of Abraham's and Minkowski's Electrodynamics," *Can. J. Phys.* , vol. 57, pp. 1022-1026, 1979.

[87] M. Kranyš, "A Minkowski-Abraham-Eckart Unified Energy-Momentum Tensor," *Phys. Scr.* , vol. 20, pp. 685-686, 1979.

[88] M. Kranyš, "The Minkowski and Abraham Tensors, and the Non-Uniqueness of Non-Closed Systems Resolution of the Controversy," *Int. J. Eng. Sci.* , vol. 20, pp. 1193-1213, 1982.

[89] G. A. Maugin, "Further Comments on the Equivalence of Abraham's, Minkowski's, and Others' Electrodynamics," *Can. J. Phys.,* vol. 58, pp. 1163-1170, 1980.

[90] Y. N. Obukhov and F. W. Hehl, "Electromagnetic Energy–Momentum and Forces in Matter," *Phys. Lett. A* vol. 311, pp. 277-284, 2003.

[91] E. A. Hinds and S. M. Barnett, "Momentum Exchange between Light and a Single Atom: Abraham or Minkowski?," *Phys. Rev. Lett.* , vol. 102, p. 050403, 2009.

[92] R. V. Jones and J. C. S. Richards, "The Pressure of Radiation in a Refracting Medium," *Proc. R. Soc. London Ser. A* vol. 221, pp. 480-498, 1954.

[93] A. Ashkin and J. M. Dziedzic, "Radiation Pressure on a Free Liquid Surface," *Phys. Rev. Lett.,* vol. 30, pp. 139-142, 1973.

[94] G. B. Walker, D. G. Lahoz, and G. Walker, "Measurement of Abraham Force in a Barium-Titanate Specimen," *Can. J. Phys.* , vol. 53, pp. 2577-2586, 1975.

[95] I. Brevik, "Experiments in Phenomenological Electrodynamics and the

Electromagnetic Energy-Momentum Tensor," *Phys. Rep.,* vol. 52, pp. 133-201, 1979.

[96] U. Leonhardt, "Optics: Momentum in an Uncertain Light," *Nature (London)* vol. 444, pp. 823-824, 2006.

[97] R. N. C. Pfeifer, T. A. Nieminen, N. R. Heckenberg, and H. Rubinsztein-Dunlop, "Colloquium: Momentum of an Electromagnetic Wave in Dielectric Media," *Rev. Mod. Phys.* , vol. 79, pp. 1197-1216, 2007.

[98] C. Baxter and R. Loudon, "Radiation Pressure and the Photon Momentum in Dielectrics," *J. Mod. Opt.* , vol. 57, pp. 830-842, 2010.

[99] P. W. Milonni and R. W. Boyd, "Momentum of Light in a Dielectric Medium," *Adv. Opt. Photon.* , vol. 2, pp. 519-553, 2010.

[100] B. A. Kemp, "Resolution of the Abraham-Minkowski Debate: Implications for the Electromagnetic Wave Theory of Light in Matter," *J. Appl. Phys.* , vol. 109, p. 111101, 2011.

[101] S. M. Barnett, "Resolution of the Abraham–Minkowski Dilemma," *Phys. Rev. Lett.* , vol. 104, p. 070401, 2010.

[102] D. G. Grier, "A Revolution in Optical Manipulation," *Nature (London)* vol. 424, pp. 810-816, 2003.

[103] A. Ashkin, "Acceleration and Trapping of Particles by Radiation Pressure," *Phys. Rev. Lett.* , vol. 24, pp. 156-159, 1970.

[104] A. Ashkin, J. M. Dziedzic, J. E. Bjorkholm, and S. Chu, "Observation of a Single-Beam Gradient Force Optical Trap for Dielectric Particles," *Opt. Lett* vol. 11, pp. 288-290, 1986.

[105] J. Chen, J. Ng, Z. Lin, and C. T. Chan, "Optical Pulling Force," *Nature Photon.* , vol. 5, pp. 531-534, 2011.

[106] A. Novitsky, C. W. Qiu, and H. Wang, "A Single Gradientless Light Beam Drags Particles as Tractor Beams," *Phys. Rev. Lett.* , vol. 107, p. 203601, 2011.

[107] D. B. Ruffner and D. G. Grier, "Optical Conveyors: A Class of Active Tractor Beams," *Phys. Rev. Lett.* , vol. 109, p. 163903, 2012.

[108] O. Brzobohatý, V. Karásek, M. Šiler, L. Chvátal, T. Čižmár, and P. Zemánek, "Experimental Demonstration of Optical Transport, Sorting and Self-Arrangement Using a 'Tractor Beam'," *Nature Photon.* , vol. 7, pp. 123-127, 2013.

[109] V. Kajorndejnuku, W. Ding, S. Sukhov, C. W. Qiu, and A. Dogariu, "Linear Momentum Increase and Negative Optical Forces at Dielectric Interface," *Nature Photon.,* vol. 7, pp. 787-790, 2013.

[110] G. A. Swartzlander, T. J. Peterson, A. B. Artusio-Glimpse, and A. D. Raisanen, "Stable Optical Lift," *Nature Photon.* , vol. 5, pp. 48-51, 2011.

[111] A. Hendi, J. Henn, and U. Leonhardt, "Ambiguities in the Scattering Tomography for Central Potentials," *Phys. Rev. Lett.* , vol. 97, p. 073902, 2006.

[112] B. A. Kemp, T. M. Grzegorczyk, and J. A. Kong, "Ab Initio Study of the Radiation Pressure on Dielectric and Magnetic Media," *Opt. Express* vol. 13, pp. 9280-9291, 2005.

[113] B. A. Kemp, T. M. Grzegorczyk, and J. A. Kong, "Lorentz Force on Dielectric and Magnetic Particles," *J. Electromagn. Waves Appl.* , vol. 20, pp. 827-839, 2006.

[114] H. Chen, B. Zhang, Y. Luo, B. A. Kemp, J. Zhang, L. Ran, *et al.*, "Lorentz Force and Radiation Pressure on a Spherical Cloak," *Phys. Rev. A* vol. 80, p. 011808, 2009.

[115] S. M. Barnett and R. Loudon, "The Enigma of Optical Momentum in a Medium," *Phil. Trans. R. Soc. A* vol. 368, pp. 927-939, 2010.

[116] J. J. Sáenz, "Optical Forces: Laser Tractor Beams," *Nature Photon.* , vol. 5, pp. 514-515, 2011.

[117] S. Sukhov and A. Dogariu, "Negative Nonconservative Forces: Optical “Tractor Beams” for Arbitrary Objects," *Phys. Rev. Lett.* , vol. 107, p. 203602, 2011.

[118] A. Dogariu, S. Sukhov, and J. J. Sáenz, "Optically Induced 'Negative Forces'," *Nature Photon.* , vol. 7, pp. 24-27, 2013.

[119] A. Novitsky, C. W. Qiu, and S. Zouhdi, "Transformation-Based Spherical Cloaks Designed by an Implicit Transformation-Independent Method: Theory and Optimization," *New J. Phys.* , vol. 11, p. 113001, 2009.

[120] V. A. De Lorenci, R. Klippert, S. Y. Li, and J. P. Pereira, "Multirefringence Phenomena in Nonlinear Electrodynamics," *Phys. Rev. D,* vol. 88, p. 065015, 2013.

[121] N. Bloembergen and P. S. Pershan, "Light Waves at the Boundary of Nonlinear Media," *Phys. Rev.,* vol. 128, pp. 606–622, 1962.

[122] I. V. Lindell, A. H. Sihvola, S. A. Tretyakov, and A. J. Viitanen, *Electromagnetic Waves in Chiral and Bi-Isotropic Media* Boston: Artech House, 1994.

[123] S. Bassiri, C. H. Papas, and N. Engheta, "Electromagnetic Wave Propagation through a Dielectric-Chiral Interface and through a Chiral Slab," *J. Opt. Soc. Am. A,* vol. 5, pp. 1450-1459, 1988.

[124] F. Mariotte, P. Pelet, and N. Engheta, "A Review of Recent Study of Guided Waves in Chiral Media," *Prog. Electromagn. Res.* , vol. 9, pp. 311-350, 1994.

[125] J. B. Pendry, "A Chiral Route to Negative Refraction," *Science* vol. 306, pp. 1353-1355, 2004.

[126] S. Tretyakov, A. Sihvola, and L. Jylhä, "Backward-Wave Regime and Negative Refraction in Chiral Composites," *Photonics Nanostruct. Fundam. Appl.* , vol. 3, pp. 107-115, 2005.

[127] S. Zhang, Y. S. Park, J. Li, X. Lu, W. Zhang, and X. Zhang, "Negative Refractive Index in Chiral Metamaterials," *Phys. Rev. Lett.* , vol. 102, p. 023901, 2009.

[128] V. V. Shevchenko, "The Geometric-Optics Theory of a Plane Chiral-Metamaterial Lens," *J. Comm. Tech. Electron.,* vol. 54, pp. 662-666, 2009.

[129] M. Nieto-Vesperinas, J. J. Sáenz, R. Gomez-Medina, and L. Chantada, "Optical Forces on Small Magnetodielectric Particles," *Opt. Express,* vol. 18, pp. 11428-11443, 2010.

[130] J. D. Jackson, *Classical Electrodynamics*. NY: John Wiley, 1998.

[131] L. D. Landau, E. M. Lifshitz, and L. P. Pitaevskii, *Electrodynamics of Continuous Media*. Oxford: Pergamon Press, 1984.

[132] J. Schwinger, J. L. L. Deraad, K. A. Milton, and W.-y. Tsai, *Classical Electrodynamics*: Westview Press, 1998.

[133] T. Shiozawa, *Classical Relativistic Electrodynamics: Theory of Light*

Emmision and Application to Free Electron Lasers. New York: Springer-Verlag Berlin Heidelberg, 2004.